UNIVERSITY OF CORDOBA
FLUVIAL DYNAMICS AND HYDROLOGY RESEARCH GROUP
ANDALUSIAN INSTITUTE FOR EARTH SYSTEM RESEARCH

PhD Dissertation

# INFLUENCE OF MICROSCALE IN SNOW DISTRIBUTED MODELLING IN SEMIARID REGIONS

PhD Student: Rafael Pimentel Leiva
Supervisors: María José Polo Gómez
Javier Herrero Lantarón

Córdoba, December 2014

TITULO: *Influence of microscale in snow distributed modelling in semiarid regions*

AUTOR: *Rafael Pimentel Leiva*


Campus de Rabanales
Ctra. Nacional IV, Km. 396 A
14071 Córdoba

www.uco.es/publicaciones
publicaciones@uco.es

**TÍTULO DE LA TESIS:** Influence of microscale in the snow distributed modelling in semiarid regions

**DOCTORANDO/A:** Rafael Pimentel Leiva

## INFORME RAZONADO DEL/DE LOS DIRECTOR/ES DE LA TESIS

(se hará mención a la evolución y desarrollo de la tesis, así como a trabajos y publicaciones derivados de la misma).

María José Polo Gómez y Javier Herrero Lantarón, profesora del Departamento de Agronomía de la Universidad de Córdoba e Investigador Contratado del IISTA-UGR, como directores de la tesis doctoral del alumno del Programa de Doctorado "Dinámica de Flujos Biogeoquímicos y su Aplicación" Rafael Pimentel Leiva

INFORMAN,

Que el doctorando ha cubierto los objetivos propuestos en la tesis y ha estudiado los problemas que surgen al extender un modelo puntual de balance de energía en nieve ya existente a uno distribuido, y los ha solucionado. De manera que, como conclusión de la tesis, se ha obtenido un modelo físico distribuido calibrado para Sierra Nevada (España). Para ello ha utilizado combinadamente dos técnicas de teledetección, la primera basada en imagen visible terrestre, y la segunda en imagen hiperespectral desde satélite. Estas técnicas le han permitido obtener datos de la distribución de la nieve en planta con distintas resoluciones y dominio espacial, que han sido aprovechadas en el modelado distribuido de la nieve para definir ecuaciones y parámetros de entrada, calibrar y validar resultados, y poner en práctica técnicas de asimilación. Para ello, el doctorando ha tenido que desarrollar varias técnicas novedosas en el modelado distribuido de la nieve a escala de cuenca en Sierra Nevada, como la georreferenciación de fotografía terrestre mediante técnicas de "computer vision", detección de nieve en esas mismas imágenes mediante "machine learning", la asimilación de datos en el modelado físico utilizando filtros de Kalman, el tratamiento y corrección automática de imágenes Landsat, y el análisis de mezcla espectral en imágenes de Landsat. El trabajo se ha plasmado en dos programas de software libres programados por el propio doctorando en MatLab, una publicación en una revista indexada (Q1), y tres aportaciones a congresos indexados con revisión por pares, lo que avala la calidad del trabajo realizado.

Por todo ello, se autoriza la presentación de la tesis doctoral

Córdoba, 21 de noviembre de 2014

Firma del/de los director/es

Fdo.: María José Polo Gómez

Fdo.: Javier Herrero Lantarón

*A mis padres*

# Agradecimientos

Al proyecto CGL2011-25632, *Dinámica de la nieve en regiones mediterráneas y su modelado a diversas escalas. Implicación para la gestión de recursos hídricos* del Ministerio de Ciencia e Innovación; al proyecto, *Estudio del efecto del cambio global sobre la nieve y la hidrología de alta montaña en el Parque Nacional de Sierra Nevada,* de Fundación Biodiversidad, Ministerio de Agricultura, Alimentación y Medio Ambiente; y, al Grupo de Dinámica Ambiental de la Universidad de Granada, por su financiación para la realización de esta tesis.

Al Instituto de Estudios de Postgrado de la Universidad de Córdoba por su financiación para la realización de la estancia para la obtención de la mención internacional en el título de doctor.

A los responsables del Refugio Poqueira por su ayuda desinteresada.

A los gestores del Espacio Natural Protegido de Sierra Nevada por todas las facilidades para llevar a cabo las labores investigadoras dentro de sus límites.

A mis directores, María José y Javi, por darme esta oportunidad, por confiar en mí, por enseñarme a no conformarme con el primer resultado e intentar dar siempre esa vuelta de tuerca más, por contagiarme su afán por aprender y por su paciencia.

A Miguel Losada, por no hacer caso omiso a aquellos correos y contar conmigo en su equipo.

A Bob Su, por acogerme durante tres meses en su departamento, por sus consejos y su gran ayuda en mi investigación.

A mis compañeros del grupo de Dinámica Ambiental y Dinámica Fluvial e Hidrología, por su ayuda durante estos años y por hacer más fácil el día a día. En especial a Álex y Rafa, son muchos los años ya juntos.

A mis amigos del ITC, por hacer que mi estancia en Holanda fuese una gran experiencia.

A mis compañeros de máster.

Al resto de mis amigos.

A mis padres y a mi hermano, por todo su esfuerzo, ayuda y apoyo incondicional.

Gracias.

# Index

# List of Figures

# List of Tables

# List of symbols

| | |
|---|---|
| $\alpha$ | Albedo |
| $\varepsilon_\lambda$ | Residual error |
| $\lambda$ | Wavelength |
| $\phi_H$ | Stability-correction factor for non-adiabatic temperature gradient for sensible heat |
| $\phi_M$ | Stability-correction factor for non-adiabatic temperature gradient for mass |
| $\phi_V$ | Stability-correction factor for non-adiabatic temperature gradient for wind |
| $\sigma_{SB}$ | Stephan-Boltzman constant |
| **A** | Ensemble individual anomalies |
| **d** | Observation |
| $E$ | Flux of water mass exchange with the atmosphere |
| $e_a$ | Air pressure vapor |
| $e_{sn}$ | Saturatiom vapor pressure |
| G | Flux of sensible heat exchange with the ground |
| **G** | |
| $H$ | Flux of sensible heat exchange with the atmosphere |
| **H** | Operator mapping |
| $h$ | Snow depth |
| $\bar{h}$ | Mean snow depth |
| $h_e^*$ | Dimensionless snow depth when melt begins |
| $h_m^*$ | Dimensionless snow depth when maximum melt rate is achieve |
| $K$ | Net solar radiation flux |
| **K** | Kalman gain |
| $K_{u_E}$ | Bulk latent-heat transfer coefficient |
| $K_H$ | Bulk sensible-heat transfer coefficient with wind |
| $K_{H0}$ | Bulk sensible-heat transfer coefficient without wind |
| $L$ | Net termal radiation flux |
| $M$ | Flux of metling water |
| $m$ | Ensemble size |
| $P$ | Precipitation |
| $\mathbf{P}^{\mathrm{f}}$ | Forecast error covariance |
| **R** | Observation error covariance |
| $R_{s,\lambda}$ | Radiance measured at the sensor |
| **s** | Scaled innovation vector |
| **S** | Scaled ensemble observation anomalies |
| $SCF$ | Snow cover fraction |
| $SCF*$ | Dimensionless snow cover fraction |
| $SWE$ | Snow wáter equivalent |
| $SWE*$ | Dimensionless snow water equivalent |
| **T** | Transfor matrix for ETKF |
| $T_a$ | Air temperature |
| $T_{sn}$ | Snow temperature |
| $u$ | Internal energy per unit of mass |
| $U$ | Total internal energy |
| $u_E$ | Unitary energy flux associated with flux of flux water mass exchange with atmosphere |
| $u_M$ | Unitary energy flux associated with melting flux |
| $u_p$ | Unitary energy flux associated with precipitation |
| $u_W$ | Unitary energy flux associated with flux of water mass transport due to wind |
| $v_a$ | Wind speed |
| $W$ | Flux of water mass transport due to wind |
| **x** | Ensemble mean |
| $\mathbf{x}^{\mathrm{a}}$ | Analysis |
| $\mathbf{x}^{\mathrm{f}}$ | Forecast |
| $z_R$ | Reference altitude |
| $z_0$ | Snow roughness |

# Acronyms

| | |
|---|---|
| CV | Coefficient of variation |
| DC | Depletion curve |
| DEM | Digital Elevation Model |
| DI | Direct Insertion |
| EnKF | Ensemble Kalman Filter |
| ESRF | Ensemble Squared Root Filter |
| ETKF | Ensemble Transform Kalman Filter |
| GCMs | Genetal Circulation Models |
| MAE | Mean Absolute Error |
| ME | Mean Error |
| MODIS | Moderate-resolution Imaging Spectroradiometer |
| NDSI | Normalized Difference Snow Index |
| NWPMs | Numerical Weather Prediction Models |
| NOAA | National Oceanic and Atmospheric Administration |
| $R^2$ | Correlation coeficient |
| RIA | Agroclimatic Information Network of Andalusia |
| RCMs | Regional Climate Models |
| RMSE | Root Mean Squared Error |
| TP | Terrestrial photography |

# Summary

This work focuses on the importance of the microscale snow distribution in the modelling of the snow dynamics in semiarid regions. Snow over these areas has particular features that further complicate its measuring, monitoring and modelling (e.g. several snowmelt cycles throughout the year and a very heterogeneous distribution). Most extended GIS-based calculation of snowmelt/accumulation models must deal with non-negligible scales effects below the cell size, which may result in unsatisfactory predictions depending on the study scale. This study proposes the joint use of physically- based distributed snowmelt-accumulation modelling and remote sensing observation datasets to study the subgrid variability of snow distribution and its effects on the snow modelling at the watershed scale. The study has been carried out in Sierra Nevada Mountains, southern Spain, where the highest submit of the Iberian Peninsula can be found close to the seaside, which results in a sharp gradient of climate conditions associated to topography. The typical Alpine climate in the mountains is modulated by the subtropical conditions at the coast, with occurrence of snowfall usually from November to April in altitudes greater than 2000 m, and successive cycles of accumulation and snowmelt during the season.

Terrestrial photography data, an alternative and economical remote sensing information source whose scales can be adapted to the studied processes requirements, has been employed to study the snow dynamics at the subgrid scale (30 x 30 m). Snow cover area and snow depth datasets were obtained from terrestrial images in a pilot study area during 2009-2013. These dataset was employed to define the subgrid variability by means of depletion curves with two different approaches. As a first step, different snow depletion curves proposed by other authors were tested at the study area. The observations were included in a data assimilation scheme, an Ensemble Transform Kalman Filter, in the energy and mass balance equations of the snow model. The results identified the need for selecting a particular depletion curve parameterization depending on the succession of accumulation-melting cycles. Secondly, based on the former results, these datasets were directly employed to define parametric depletion curves at the pilot area. A flexible sigmoid function was found to satisfactorily reproduce the observed trends of the snowmelt effects on the snow cover area at the cell scale, but different values resulted for the sigmoid's parameters depending on the different snow states found: 1) cycles with a high accumulated snow depth which came from a metamorphosed snow; 2) cycles with great snow depth preceded by short accumulation phases; 3) cycles with low accumulation that occur in the cold season; and 4) cycles with low snow depth values which take place during spring. Moreover, an unique expression for the accumulation curve was also proposed. These results confirm the need of different parameterization to represent the physical variability in the accumulation-melting cycles in semiarid regions. Furthermore, this selective curve improves the model performance when compared to the results previously obtained with the data assimilation scheme.

Finally, the proposed parameterization was tested at the watershed scale, at the Guadalfeo River Basin, at the southern face of Sierra Nevada. Snow cover area distributed results from the model simulations were assessed with Landsat TM and ETM+ observations (30 x 30m spatial resolution), consisting of snow cover maps at the area from an endmembers spectral mixture analysis of the Landsat imagery. These maps had previously been validated from snow cover maps at higher spatial resolution (10m x 10m) obtained from terrestrial photography in a monitoring hillside in the area. The results showed a significant agreement between observed

and simulated data, which allows the obtaining of great spatial resolution snow map series with higher temporal resolution than the remote sensing images usually employed.

The results showed the importance of including the microscale effects on the snow modeling in semiarid regions, and also tested the capability of terrestrial photography to monitor snow variability, being a sound option to be included in standard instrumentation of weather stations in mountainous areas.

This work has been funded by the Spanish Ministry of Science and Innovation (Research Project CGL 2011-25632, “Snow dynamics in Mediterranean regions and its modelling at different scales. Implications for water management”), and the Spanish Ministry of Agriculture, Food and Environment (Biodiversity Foundation, Project “Study of the effect of global change on snow and high mountain hydrology in Sierra Nevada National Park”).

# Resumen

Este trabajo pone de manifiesto la importancia de la microescala en el modelado distribuido de la nieve en ambientes semiáridos. En estas áreas, la nieve posee características muy específicas que dificultan su medida, monitorización y modelado (p.e. diferentes ciclos de fusión a lo largo del año y una gran variabilidad espaciotemporal). Desde este último punto de vista, los modelos distribuidos de acumulación/fusión de nieve poseen limitaciones al representar procesos que ocurren a una escala inferior a la seleccionada como tamaño de celda en la discretización para la realización de sus cálculos. Este estudio propone el uso de modelado hidrológico, físico y distribuido, junto con técnicas de teledetección para el estudio de la variabilidad a escala de celda de la nieve y sus implicaciones a escala de cuenca. El área de estudio seleccionada ha sido Sierra Nevada, sur de España, cordillera paralela a la costa del mar Mediterráneo y donde se localizan las cumbres más altas de la Península Ibérica. Su proximidad al mar hace que el típico clima alpino de montaña se vea modificado por el clima subtropical de la costa, con nevadas desde noviembre a abril en cotas superiores a los 2000 m y ciclos sucesivos de acumulación y fusión de nieve durante este periodo.

La fotografía terrestre, técnica de teledetección novedosa y económica, que permite adaptar las observaciones a la escala de los procesos estudiados, ha sido empleada para el estudio de la dinámica de la nieve a escala de celda (30 x 30 m). Valores de superficie cubierta y espesor de nieve han sido obtenidos en una pequeña área experimental durante el período 2009-2013. Estas series de datos fueron empleadas para definir la variabilidad espacial dentro de la celda por medio de curvas de agotamiento utilizando dos enfoques. En primer lugar, diferentes curvas de agotamiento propuestas por otros autores fueron evaluadas en el área de estudio. Las observaciones fueron incluidas mediante un algoritmo de asimilación de datos, *Ensemble Transform Kalman Filter*, en el balance de masa y energía del modelo de nieve. Los resultados mostraron la necesidad de seleccionar diferentes curvas de agotamiento dependiendo de la sucesión de los ciclos de fusión-acumulación. En segundo lugar y en base a los resultados previos, estas series de datos fueron directamente empleadas para definir curvas de agotamiento paramétricas en el área experimental. Una curva sigmoide fue la utilizada para reproducir las tendencias de los diferentes ciclos de fusión, donde diferentes parámetros de ajuste fueron obtenidos para cada uno de estados encontrados: 1) ciclos con un gran espesor de nieve muy metamorfoseada; 2) ciclos son gran espesor de nieve precedidas de una fase de acumulación corta; 3) ciclos con poco espesor durante la estación de nieve; y 4) ciclos con poco espesor de nieve que tienen lugar en primavera. Una única parametrización fue propuesta para los ciclos de acumulación. Estos resultados confirmaron la necesidad de diferentes parametrizaciones para la representación de la variabilidad observada en los ciclos de acumulación-fusión en ambientes semiáridos. La elección de estas curvas mejora los resultados en el modelado si se comparan con los obtenidos utilizando el algoritmo de asimilación.

Finalmente, la parametrización propuesta fue evaluada a escala de cuenca, en la cuenca del río Guadalfeo, cara sur de Sierra Nevada. Los mapas distribuidos de superficie cubierta de nieve obtenidos en el modelado fueron comparados con mapas de nieve obtenidos mediante la aplicación de un modelo de mezclas espectrales aplicado sobre imágenes Landsat TM y ETM+ (30 x 30 m). Estos mapas fueron previamente validados con mapas de nieve a mayor resolución (10 x 10 m) obtenidos gracias a imágenes terrestres in una ladera monitorizada dentro de la cuenca. Los resultados muestran una gran concordancia entre mapas medidos y simulados, lo

cual permite obtener una amplia serie de mapas con mayor resolución temporal que la de las observaciones Landsat.

Los resultados manifiestan la importancia de incluir los efectos de la microescala en el modelado de la nieve en ambientes semiáridos, así como la capacidad que la fotografía terrestre posee para monitorizar la variabilidad de la capa de nieve, constituyendo una gran opción para ser incluida dentro de la instrumentación común que instalar en estaciones meteorológicas en zonas de montaña.

# CHAPTER 1: Introduction

*This chapter introduces the crucial role that snow plays in the hydrological cycle and how it increases in semiarid environments. In these regions, snow modelling requires a further assessment due to the highly heterogeneous spatial distribution of snow and its evolution. A brief revision of the different approaches for snow modelling found in the literature, emphasizing on their capability of capturing the particular characteristics of the snow in these areas, is first done; scale issues are specifically addressed. Furthermore, the chapter explores different techniques employed in obtaining snow evolution observations. A general description of the study area, Sierra Nevada Mountain Range (South Spain), is also included. The chapter finally presents the objectives of this work and the organization of the rest of the thesis.*

Snow dominates climate conditions and hydrology in many of the world's mountainous region. One-sixth of the total Earth's population depends on snowmelt for water resources (Barnett et al., 2005; Painter et al., 2009). In general, snowmelt dominant regions are located in latitudes greater than 45° (North and South) and, thus, largest efforts on studying snow dynamics and evolution have been developed over these areas. However, in some mountainous locations situated in warm regions at middle latitudes, snow dynamics further conditions the availability of water resources. This is the case of some semiarid Mediterranean climate regions, distributed all over the world (), such as Sierra Nevada Mountains (Southern Spain), Atlas Mountain Range (Northern Morocco), Mount Etna (Sicilia, Italy), the southern face of The Alps (Italy), Andes Mountain Range (Chile), Sierra Nevada Mountain (USA) and Colorado Plateau (USA).

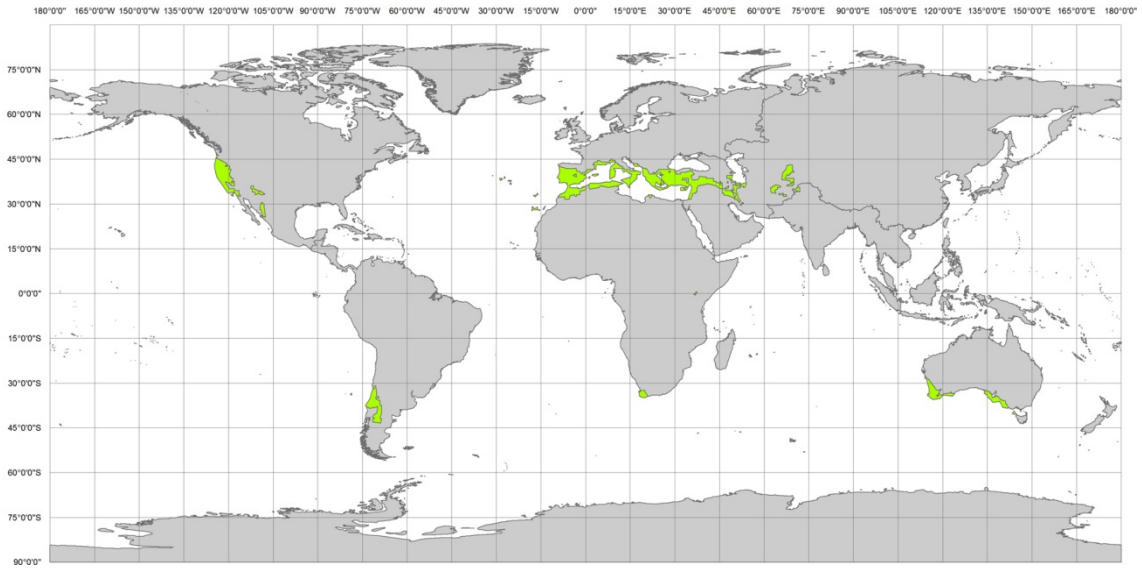


Figure 1.1 Mediterranean regions over the world.

Their different location over the globe implies that the typical mountainous climate is modified by Mediterranean surrounding weather conditions (i.e. high level of solar energy incoming throughout the year, variable character with lower precipitations and the recurrent presence of drought stages). In cold regions, the snow dynamics is usually characterized by the progressive accumulation of snowfall during the winter months. As a result, a deep and somehow uniform snowpack develops, which usually undergoes an unique melt cycle during spring. However, in semiarid areas, the snow behaviour is characterized by a highly strong spatiotemporal variability, and the occurrence of several accumulation-melting cycles throughout the year.

Figure 1.2 shows this heterogeneous spatial distribution found over Sierra Nevada Mountain, southern Spain, for selected areas over the 2009-2013 snow seasons. Different significant spatial scales appear in some areas associated with irregular snow distribution. On one hand, microscale patterns O (~m) conditioned by the interaction between the snow and the micro-topography (Figure 1.2 (limelight) and Figure 1.2 c) and, thus, associated to shallow snow depths can be found for light isolated snowfall events or at the beginning/end of an accumulation-melting cycle. On the other hand, snow patches at the hillside scale O (~100m), highly conditioned by the wind, usually develop associated with the terrain curvature (Figure 1.2 (background), Figure 1.2 b).


Figure 1.2 Different picture of the heterogeneous snow distribution over Sierra Nevada Mountain Range at different spatial resolution:.a) Panoramic view of the east part of south face of Sierra Nevada Mountain (2013 March 26); b) Caballo hillside during spring melt season, north face of Sierra Nevada Mountain (2009 June 6); c) Monitored area (30m x 30m) close to Refugio Poqueira (2011 Nov 30).

All these specific features increase the complexity in monitoring and modelling the snow behaviour and distribution over these regions. Currently, a combination of both modelling and remote sensing sources is mostly used for studying snow dynamics. However, the particular characteristics found over this semiarid environment require a specific study of the snow representation in both ways, especially for coarse spatial resolutions in remote sensing observations.

## 1.1. Snow modelling

During the last two decades, a significant amount of snow models has been developed. Their design, formulation and structure are closely related with the final purpose for which they are conceived. These uses go from their early inclusion in atmospheric models – i.e. general circulation model (GCMs) (Loth et al., 1993; Roeckner et al., 1996; Yang et al., 1997), regional climate models (RCMs) (Mabuchi et al., 1997; Shmakin, 1998) and numerical weather prediction model (NWPMs) (Kim and Ek, 1995; Smirnova et al., 1997) – to advanced snow

process studies (REFs) and other derived applications, such as avalanche forecasting (Lehning et al., 2002; Bartelt and Lehninhg, 2002), runoff forecasting (Tarboton and Luce, 1996; Lindstrom et al., 1997), climate monitoring (Grody and Basist, 1996) or downscaling GCM output (Xue et al., 1991). Models' resolution and formulation in sophisticated models (Jordan, 1991; Liston and Sturm, 1998) are usually not computationally efficient for being used in GCMs (Loth et al., 1993; Roeckner et al., 1996; Yang et al., 1997).

Within the snow models employed to study snow processes, the required complexity of the modelling depends on the approach to the physics of the processes represented. For example, the empirical approaches that correlate meteorological variables with snow fluxes (Kuchment et al. 1983; Kustas et al., 1994; Beninston et al., 2003) may not correctly represent the quick evolution of some processes over these changing environments. At the other extreme, the excessively complex formulation found in other approaches, i.e. Jordan (1991), has a computational cost which may be very high to reproduce large snow areas. Moreover, as mentioned above, most of snowmelt-accumulation models are conceived to study snow in cold regions and thus, they do not take into account some particular characteristics of the snow in warm and middle latitude region (Schulz et al. 2004; Sade et al. 2014).

Herrero et al. (2009) developed a point snow model for the study area, based on the physical approach from Anderson (1979), in which an empirical expression for the atmospheric emissivity was included to account for the local conditions. This mass and energy balance approached adequately the snow processes over this Mediterranean area, and included the net radiation transfer, the latent and the sensible heat transfer, and heat advection by rainfall. The model assumes a uniform horizontal snow cover surface distributed in one vertical layer defined by the snow column per unit area, which has the atmosphere as an upper boundary and the ground as a lower one.

The point calculations are usually extended over larger areas by means of simultaneous calculations throughout the cells represented in a Digital Elevation Model (DEM). This extension involves some scale effects to take into account the cell size and the significant processes at this subgrid scale; some corrections are then needed to properly represent the processes at the selected spatial resolution.

## 1.2. Scales issue in distributed snow modelling

Important scale issues appear when point calculations are extended to distributed values. The formulation proposed above (a single vertical layer with uniform density and temperature in the snowpack, and negligible horizontal fluxes) permits a simple extension to a distributed model by means of making calculation simultaneously in grid cells (Tarboton and Luce, 1996; Essery et al., 1999; Herrero et al., 2009). These hypothesis can be assumed for a maximum cell size, which depends on the local variability, over which non-negligible error are found in the distributed simulation of the snow-state variables. Even for such cell size, not all the relevant properties of snow can be considered homogeneous and this spatial variability must be somehow represented in the modelling (Blösch, 1999; Liston, 2004).

The basic solution is to split up the total spatial variability into two different sources: a small-scale variability within elements (subgrid variability) and a large-scale variability between elements (element-to-element variability) (Smagorinsky, 1974; Kirnbauer et al., 1994). The subgrid variability is usually defined by means of parameterization of the process at this scale

using lumped relationships between selected snow variables, and the element-to-element variability is explicitly represented by the model cell size. A lot of works have been developed to represent this element-to-element variability (Obled and Harder, 1979; Blöschl et al., 1991; Davis et al., 1995; Molotch and Bales, 2005; Clark et al., 2011). On the contrary, much less literature about subgrid variability is found (Roesch and Roeckner, 2006; Niu and Yang, 2007; Meromy et al., 2013).

The extended method to define the cell size recommends the search of a clearly discernible scale of variability capable to separate the large scale processes from the small scale ones. Based on the high heterogeneity shown by the snow distribution over these semiarid areas (Figure 1.2), these two different scales can be selected. On one hand, the microscale O (~m) snow distribution, very heterogeneous and totally conditioned by the interaction between snow and micro-topography, conditions the generation of turbulent flows (Dadic et al., 2010). On the other hand, hillside scale O (~100m) distribution is mainly controlled by the atmospheric agents, principally the wind, which acts as a crucial term in the energy balance and as one of the main transport agents. Nevertheless, in practice, the selection of the optimum grid cell size is often defined by practical considerations, such as data availability and the required resolution in the predictions (Blösch, 1999; Winstral et al., 2002).

Finally, different approaches for quantifying subgrid spatial variability of hydrologic processes can be found (Blöschl and Sivapalan, 1995). They include: a) the use of distribution functions rather than a single point to define snow depletion curve, which extends the point mass and energy balance calculation by using a relationship between one selected snow state variable and the snow cover fraction over a fixed area (Luce et al., 1999) (Anderson, 1973; Luce et al., 1999); b) the adoption of effective values for the model parameters, assuming that they are uniform within each element (e.g. Blöschl and Sivapalan, 1995; Wen and Gómez-Hernández, 1996); and c) the parameterization without explicitly resorting to the point equations (Blösch and Kirnbauer, 1991). This thesis aims to gain insight of the parameterization of this subgrid variability in Mediterranean snow regions.

## 1.3. Snow monitoring

The traditional snow observations consist of *in situ* measurements via periodic snow surveys at fixed locations, such as snow courses or snow pillows, or automated snow monitoring systems usually coupled to weather stations. These *in situ* measurements have the inconvenience of a limited accessibility to study sites during the snow season, the hard conditions under which the continuous measurements must be made, and the difficulty and costs to adequately cover large and heterogeneous areas (DeWalle and Rango, 2008).

A costly-effective alternative to these techniques is the use of remote sensing sources. These systems are generally based on the estimation of physical snow properties throughout the electromagnetic spectrum (e.g. electro-optical systems, thermal infrared system, passive microwave system, laser system and photography). Nowadays, they constitute the most powerful and relevant source of information for medium to large scale regional studies. Airborne sensors offer imagery with high spatial resolution, medium spatial coverage and rapid acquisition. Nevertheless, they still have a high cost per unit covered area, which limits their application over large zones. On the contrary, spaceborne sensors develop a continuous monitoring of the Earth surface and cover vast ground extensions. Different space agencies provide satellite remote sensing datasets, with derived products for specific applications in

many cases. For snow studies, the most extended satellite dataset are: Landsat TM, ETM+ and OLI with temporal resolution of 16 days and spatial resolution of 30 x 30m, MODIS, daily images with 250 x 250m spatial resolution, and NOAA, 1 x 1 km daily images. However, these fixed spatial and temporal resolutions may constitute a limitation for complex topographies or highly variable weather conditions; moreover, the recurrent presence of cloud cover during a significant fraction of the snow season poses a constraint for snow applications.

An economic alternative is the use of terrestrial photography. These conventional images are ground-taken from the Earth surface and their temporal and spatial resolution can be adapted to the processes under study. Terrestrial photography also eliminates the problems associated to cloud coverage; furthermore, its combination with satellite information may enhance the quality of the finally derived data. By testing smaller sites with a higher resolution, the results can be validated for the whole coverage area (Corripio, 2004). This technique has the limitation of not being able to cover vast extensions, as satellite images do. Nevertheless, its application to the study of snow processes at the subgrid, hillside or small basin scales allows adapting the observation to the required needs.

## 1.4. Study area

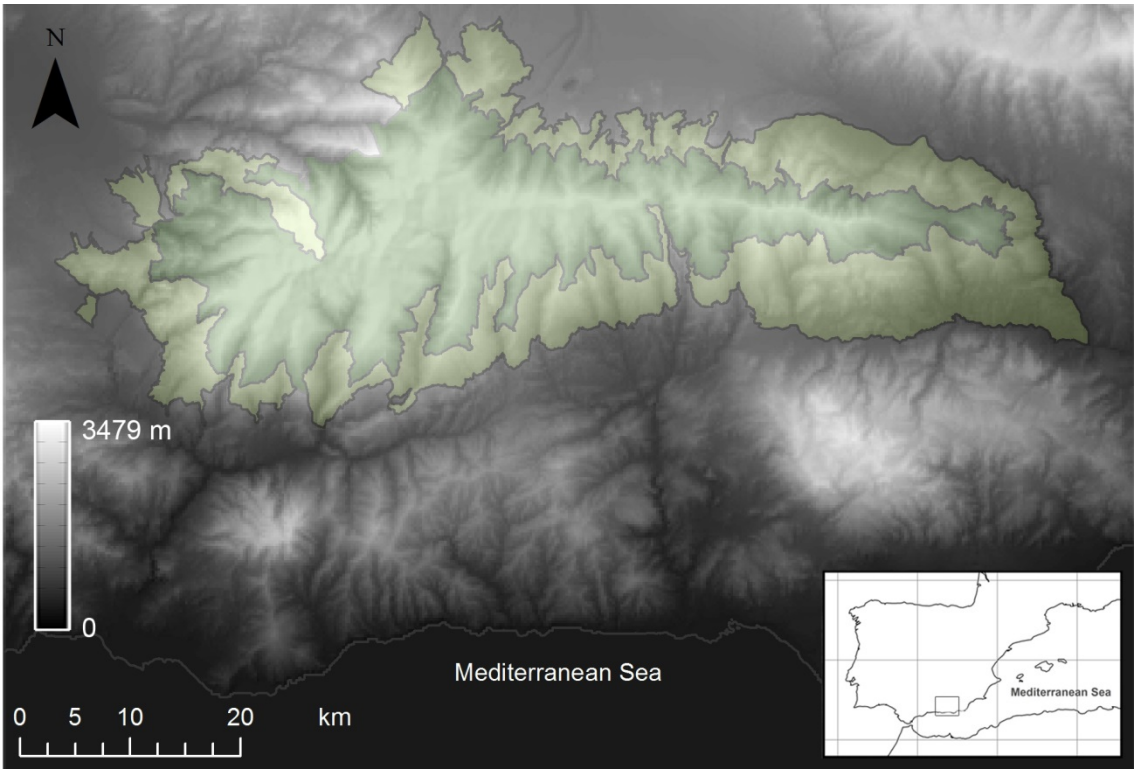


Figure 1.3 Location of Sierra Nevada Mountain Range in Spain, and limits of the protected areas: National Park (dark green) and Natural Park (light green).

Sierra Nevada Mountains, southern Spain, are a linear mountainous range parallel to the shoreline of the Mediterranean Sea, where the highest summits of the Iberian Peninsula can be found (Mulhacen peak, 3479 m) (Figure 1.3). It is the second highest range in Europe, only surpassed by the Alps. Consequently, snow usually appears throughout the year in the areas above 2000 m. Its proximity to the sea, only 40 km south, generates a very specific climate as the result of the interaction between sea and mountain conditions. The typical alpine climate is then modified by the Mediterranean surrounding features and, thus, snow is significantly

affected. Obviously, snow in the area is closer to alpine than boreal dynamics but strongly modified, however, by the low latitude, the low relative humidity and the proximity to the sea.

The region is affected by a strong altitudinal gradient with marked differences between the south (directly affected to the sea) and the north faces. Table 1.1 shows some statistical descriptors of temperature and precipitation on both an annual and daily basis over these areas.

Table 1.1 Main statistical description for meteorological variables in Sierra Nevada Mountain from 2009-2013

| | | **Annual mean** | **Annual standard deviation** | **Daily maximum** | **Daily minimum** |
|---|---|---|---|---|---|
| South Face | | | | | |
| High areas (over 2000 m.a.s.l) | Precipitation (mm) | 783.3 | 35.8 | 85.7 | 0.1 |
| | Temperature (ºC) | 7.8 | 6.9 | 30.5 | -20.2 |
| | Radiation (MJ $m^{-2}$ $day^{-1}$) | 11.1 | 1.1 | 1.45 | 35.9 |
| | Wind Speed ($ms^{-1}$) | 8.2 | 0.5 | 17.9 | 0.1 |
| Low areas (below 2000 m.a.s.l) | Precipitation (mm) | 503.7 | 160.1 | 79.0 | 0.1 |
| | Temperature (ºC) | 14.8 | 7.4 | 38.6 | -8.1 |
| | Radiation () | 9.5 | 1.5 | 0.7 | 35.4 |
| | Wind Speed ($ms^{-1}$) | 3.2 | 1.4 | 8.2 | 0.1 |
| North Face | | | | | |
| High areas (over 2000 m.a.s.l) | Precipitation (mm) | - | - | - | - |
| | Temperature (ºC) | 6.8 | 5.6 | 29.8 | -21.2 |
| | Radiation (MJ $m^{-2}$ $day^{-1}$) | 10.9 | 0.3 | 0.9 | 35.7 |
| | Wind Speed ($ms^{-1}$) | 5.1 | 2.2 | 19.3 | 0.1 |
| Low areas (below 2000 m.a.s.l) | Precipitation (mm) | 526.7 | 116.3 | 120.2 | 0.1 |
| | Temperature (ºC) | 9.7 | 4.5 | 38.7 | -9.0 |
| | Radiation (MJ $m^{-2}$ $day^{-1}$) | 9.4 | 1.2 | 0.56 | 35.2 |
| | Wind Speed ($ms^{-1}$) | 2.4 | 1.3 | 9.8 | 0.1 |

The typical high mountain covers, pastures and low shrubs, are predominantly found in the area. The main shrub is *Hormathophylla spinosa*, with a relevant presence also of *Genista versicolor* and *Festuca clemetei*. They constitute two compact and densely branched low bushes that grow closely together, forming an extremely compact, low, and continuous cover, which acts as an insulator between the soil and the snowpack (Anderson et al., 2011). Trees are not common in the area affected by snow. They are reduced to isolated patches of reforested pines (Figure 1.4).

Figure 1.4 Panoramic view of the south face of Sierra Nevada Mountains.

Moreover, its particular characteristics make Sierra Nevada a rich reservoir of endemic wildlife species. Considered the most important centre of biodiversity in the western Mediterranean region, over 2100 different vascular plant taxa have been recorded, accounting for nearly 30% of the vascular flora of the entire Iberian Peninsula (Heywood, 1995; Blanca, 1996; Anderson et al., 2011). The high regions of the range were declared a UNESCO Biosphere Reserve in 1986, a Natural Park in 1989, and a National Park in 1999 (Figure 1.3).

### 1.4.1. The Guadalfeo River Basin

The Guadalfeo River basin, with an extension of 1300 $km^2$, mainly belongs to the southern hillside of Sierra Nevada Mountain. The influence of the sea directly affects this watershed, in which subtropical and high mountainous climate coexist. The altitudinal gradients are higher than in the north face and, consequently, the snow dynamics exhibits a highly variable regime. Water from the snowpack, which acts as a reservoir of water, is the basic water resource during the dry season for an area with an economy mainly based on agriculture. Furthermore, its medium size and the presence of valleys North-South oriented contributing to the main river course, the Guadalfeo river, result in a fast snow signal in the fluvial regime. Changes in the snow dynamics highly condition the water resource availability and storage in the area, with two reservoirs within the watershed (Figure 1.5).

Figure 1.5 Overview of the Guadalfeo River Basin from the Rules reservoir in the Guadalfeo River

This watershed was selected in 2003 as pilot area for the development of the distributed and physically based hydrological model WiMMed (Watershed Integrated Model in Mediterranean Environments) in the so-called Guadalfeo Project funded by the Andalusian Regional Government (Polo et al., 2010; Egüen et al., 2010). Specifically, the snow module included in WiMMed (Herrero et al., 2009; Herrero et al., 2011) was intended to reproduce the highly variable snow cycles occurring at this area and estimate snowmelt contributions to surface and subsurface flows. The model works on a 30 x 30 m spatial resolution, according to the considerations proposed by Blösch (1999) and the available snow observations in the area, is based on the energy and water balance equations over the snow column, and applies a simple linear increase between two extreme thresholds as depletion curve to include the subgrid variability. The calibration and validation of the model during the 2004-2009 period can be resumed as: the importance of the evaporation term from the snowpack in the water balance on an annual basis, which reached up to a 40% of the total snowfall, and the need of a specific parameterization of the longwave radiation, crucial term in the energy balance at this area (Herrero et al., 2009); the good performance of the distributed extension over the area, with mismatches locally significant during the final phase of snowmelt cycles and/or short intermediate cycles during the cold season (Herrero et al., 2011); and the determining role of the

wind in snow distribution during certain periods (Herrero et al., 2011), which was not specifically accounted for in the balance equations. Later work further developed an empirical expression for the atmospheric emissivity from local direct longwave radiation measurements at the site (Herrero and Polo, 2012). The study of wind as a key agent in the redistribution of snow was not directly approached due to the uncertainty in the obtaining of accurate wind fields on such an abrupt and high region; indirect approaches to include not only wind but the global subgrid and hillslope variability were further explored instead (Pimentel et al., 2012, 2014a, 2014b; Pérez-Palazón et al., 2014), as the following chapters describe. Most of the work was carried out in the Guadalfeo river basin, based on the previous results and datasets previously developed.

### 1.4.2. Monitoring network and available data

During the last decade a snow monitoring network was specifically developed in the area (Figure 1.6) to surpass the lack of weather stations and systematic snow observations above 1500 m.a.s.l. in Sierra Nevada. This network complements the weather stations from both the Agroclimatic Information Network of the Andalusian Government and the Spanish Meterology Agency in the area, and it mostly relies on two data sources: automated meteorological measurements and terrestrial photography acquisition. Both datasets are crucial to model and understand the snow behaviour in this region. Table 1.2 and Table 1.3 resume the main characteristics of each type of monitoring system in the network.

Table 1.2 Components of the different weather stations in the snow monitoring network at the Guadalfeo River Basin.

| ID | Elevation | Installation | Raingauge | Temperature & Relative Humidity probe | Pyranometer | Pyrgeometer | Alpine Wind monitor | Barometer |
|---|---|---|---|---|---|---|---|---|
| 801 | 2470 | Nov 2005-opperational | OTT Pluvio2 | Campbell Scientific CS215 | Kipp & Zonen NR-Lite | - | Young 05103-45 | CS 100, Setra 278 |
| 802 | 2510 | Nov 2004 - opperational | Geonor T-200B | Vaisala HMP45C | Kipp & Zonen NR-Lite | Kipp & Zonen CGR3 | Young 05103-45 | Druck RPT410F |
| 803 | 1332 | Aug 2009-opperational | Young | Vaisala HMP45C | Hukseflux LP02 | Hukseflux IR02 | Young 05103-45 | CS 100, Setra 278 |
| 804 | 2141 | Oct 2012 – operational | OTT Pluvio 2 | Vaisala HMP45C | Hukseflux NR01 | | Young 05103-45 | CS 100, Setra 278 |

The network is mainly composed by 4 weather stations (Table 1.2 and Figure 1.6) that monitor precipitation, temperature, relative humidity, radiation, wind and pressure at high frequency (DECIR) with equipment operating at cold temperature ranges. Three of them (801, 802, 804) are located above 2000 m.a.s.l. One additional station (803) was located in the southern border of the watershed to capture the influence of the sea.

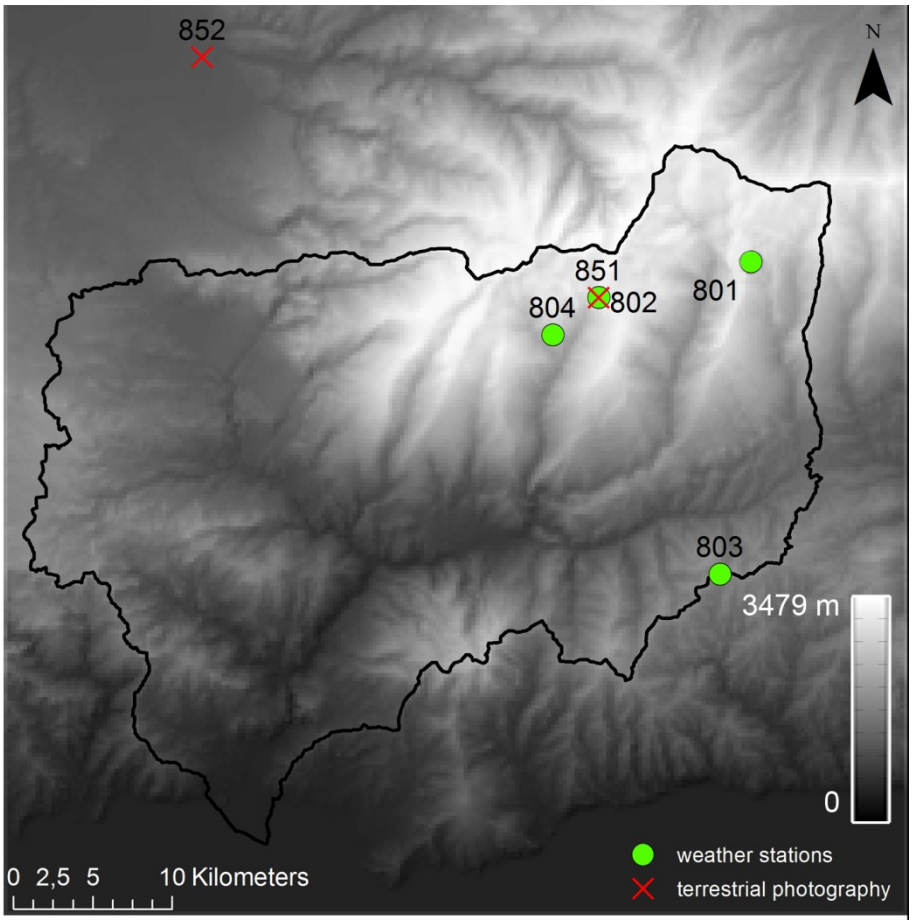


Figure 1.6 The Guadalfeo basin limits (black line). The Guadalfeo snow monitoring network: weather stations (green dots ) and terrestrial photography control points (red crosses).

Two terrestrial photography control points were also equipped in the watershed to capture the snow spatial distribution at the different scales mentioned in previous sections (Figure 1.6, Table 1.3 and Figure 1.7). Table 1.3 shows selected details of the technical characteristics of each camera. One of them were located within the highest region of the Guadalfeo basin (851), nearby weather stations in the network; their location also helped to further understand and validate the weather information collected. The other one was installed to cover part of the northern face of Sierra Nevada, where the distributed snow model had resulted in poorer approximations to the snow cover area identified from Landsat imagery, presumably due to its strong exposure to wind effects.

Table 1.3 Characteristics of the terrestrial photography systems in the snow monitoring network in Sierra Nevada.

| ID | Name | Camera | Installation | Temporal resolution | Spatial scale | Photo resolution (pixels) |
|---|---|---|---|---|---|---|
| 851 | Refugio Poqueira | CC640 Campbel Scientific | 2009/07/22-operational | 5 images per day (from 8 a.m. to 4 p.m.) | Detail (O~m) | 640 x 504 |
| 852 | Caballo hillside | Sony IPELA SNC-RZ50P | 2011/11/20-operational | 4 images per hour (4 different locations, from 7 a.m. to 7 p.m.) | Hillside (O~10m) | 640 x 480 |

Figure 1.7 Examples of the terrestrial photography network. From left to right Refugio Poqueira control area (microscale, 851) and Caballo hillside (hillside scale, 852).

Finally, different remote sensing datasets were available for this study area. In this work, Landsat TM and ETM+ imagery from 2000 to 2014 were selected for assessing the spatial distribution of snow during the study period; MODIS snow-products were discarded due to their coarse spatial resolution in terms of the microscale variability of snow in this area.

## 1.5. Objectives

From the previous work in the study area, the importance of further assessing the highly heterogeneous distribution of the snow cover has been pointed out. In this context, the main objective of this work is to explore the subgrid variability when modelling snow processes in semiarid regions, given the influence that microscale processes may have on the distribution of snow. To achieve this, terrestrial photography was used for both monitoring and further modelling the spatial distribution of snow at the study area. The study was carried out at different stages, starting with the study of the microscale influence on the physical model simulation of snow processes on a point and distributed calculation basis (terrestrial photography into the model), and finishing at the performance of the model at the basin scale once the microscale was included (terrestrial and Landsat images).

The following specific objetives were identified:

- To evaluate the use of terrestrial photography as direct observation of the microscale effects on the snow evolution. For this, terrestrial photography data from Refugio Poqueira control area (852) were used in a data assimilation scheme coupled to the snow model to reduce the uncertainties inherent to snow simulation.
- To generate a depletion curve formulation that included this subgrid variability during the accumulation-snowmelt cycles in these semiarid regions. For this, snow cover fraction and snow depth values obtained from the terrestrial images series at Refugio Poqueira control area (852) were used to parameterize depletion curves at the study area.
- To include this subgrid representation at the watershed scale and assess its improvement of the model capabilities at Sierra Nevada area. For this, terrestrial photography data at the hillslope scale from Caballo hillside 851 was used to validate the snow cover fraction distribution from a spectral mixture analysis of Landsat imagery.

These objectives also included the assessment of further needs for direct inclusion of wind effects in the modelling. Figure 1.8 shows an scheme of the work stages and the structure of this thesis work, in which terrestrial photography datasets at microscale resolution were employed to define subgrid variability: Chapter 2 is devoted to their use as indirect observations that are incorporated to the modelling by means of data assimilation techniques; Chapter 3 show their capability as direct measurement to define empirical depletion curves (DCs) that represent the

subgrid variability for different snow states during the snow season; Chapter 4 finally includes the previous results and conclusions in the distributed modelling of snow over the study area, and also uses terrestrial photography data at hillside scale as validation dataset of a spectral mixture analysis of Landsat imagery as basis for the evaluation of the model performance improvement at the watershed scale. The thesis finishes with a chapter of conclusions and further steps (Chapter 5). Some appendixes related to the treatment of terrestrial photography, Landsat images, and snow albedo have also been included.

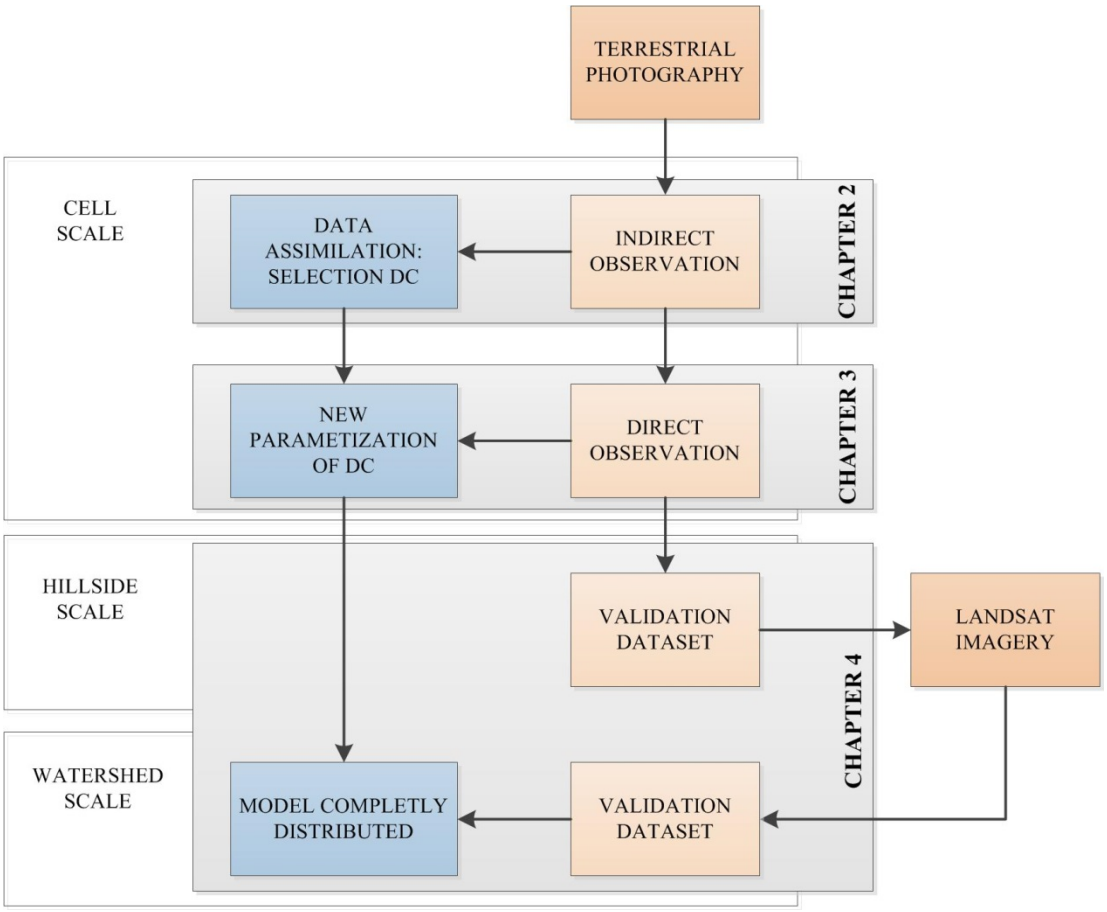


Figure 1.8 Flow chart of the different stages and significant scales addressed by the objectives of this research together with the thesis structure. Blue and red boxes correspond to snow modelling and snow observation issues in this work, respectively

# CHAPTER 2: Study snow dynamics at subgrid scale in semiarid environments combining terrestrial photography and data assimilation techniques

*Snow cover simulation is a complex task in mountain regions due to its highly irregular distribution. GIS-based calculations of snowmelt/accumulation models must deal with non-negligible scale effects below cell size, which may result in unsatisfactory predictions depending on the study scale. Terrestrial photography, whose scales can be adapted to the study problem, is a cost-effective technique, capable of reproducing snow dynamics at subgrid scale. A series of high frequency images were combined with a mass and energy model to reproduce snow evolution at cell scale (30 x 30 m) by means of the assimilation of the snow cover fraction observation dataset obtained from terrestrial photography in Sierra Nevada mountains, southern Spain. Ensemble Transform Kalman Filter technique is employed for that. The results show the convenience of adopting a selective depletion curve parameterization depending on the succession of accumulation-melting cycles in the snow season in these highly variable environments. A reduction in the error for snow depth to 50% (from 463.87 mm to 261.21 mm and from 238.22 mm to 128.50 mm) is achieved if the appropriate curve is selected.*

This chapter will be entirely published in *Journal of Hydrometeorology (in press):*
Pimentel, R., Herrero, J., Zeng, Y., Su, Z. and M. J., Polo, 2014: Study snow dynamics at subgrid scale in semiarid environment combining terrestrial photography data assimilation techniques. *J. Hydrometeorol.*

## 2.1. Introduction

Snow plays an important role in the hydrologic regime of mountainous catchments. In Mediterranean regions, significant variability in both meteorological variables and topographic features can be found (Diodato and Bellocchi 2007). This adds complexity to the task of monitoring and modeling the evolution of snow distribution, which determines the infiltration/runoff regime and the availability of water during the dry season.

Initially, a first approach to studying snowpack evolution is made by using simple empirical relationships between the snowmelt flux and selected meteorological variables (Kustas et al. 1994). However, in these areas, the marked annual, seasonal and even weekly variability of temperature, wind, and rainfall make this a difficult approach to apply in practice, and energy and mass balance equations are usually needed to capture these highly variable conditions (Anderson 1976). Many physically-based point models for the mass and energy balance in the snowpack have been developed over the last few decades (e.g. Jordan 1991; Marks and Dozier 1992; Tarboton and Luce 1996). However, the particular features of snow dynamics in Mediterranean regions (Sade et al. 2014; Schulz et al. 2004) make it difficult their application in some areas. For example, some models focus on the vertical gradients in the snow column and require complex information as input or calibration data (e.g. Jordan 1991), whereas in Mediterranean regions depths higher than 1 m may be seldom found in many sites. Other detailed approaches (e.g. Marks and Dozier 1992) capable of reproducing highly variable conditions require the availability of densely monitored areas to be calibrated, which is not frequent in mountainous areas, especially at high altitudes. On the other hand, models with a smaller number of state variables (e.g. Tarboton and Luce 1996) are very efficient to simulate runoff from snow areas with less demand of data sources, but they may not reproduce adequately the snow evolution under patchy conditions or during short and intense melting periods, due to a fixed time step in the calculation. Herrero et al. (2009) developed a point

energy balance snowmelt-accumulation model at a Mediterranean site following the formulation proposed by Tarboton and Luce (1996), which adopts a variable time step during the calculation procedure to better represent the variability of the different snow cycles within the season in these regions. The model also considers the important loss of water resources from snow evaporation under such conditions (Schulz et al. 2004; Sade et al. 2014), which accounted for as much as 42% of the total snowfall in extreme years, and the significance of the longwave radiation flux emitted from the snowpack in the energy balance. In addition, the use of a specific parameterization of this term in this area improved the model performance (Herrero and Polo 2012), and highlighted the differences in the driving processes for snow dynamics between Mediterranean and higher latitude regions.

These models can be applied over whole areas taking into account the significant issues of scale that arise when applying point models throughout a distributed area. The most common problems include: 1) the selection of an optimal grid cell size according to the physics of the studied processes; and 2) the question of how to represent the subgrid variability, also taking into account the snow dynamics. Following Blösch (1999), who affirms that an optimal cell size may not exist, the model element scale may in practice be dictated by practical considerations such as data availability to calibration and validation stages and the required resolution of the predictions. For the second question, a simple parameterization by means of depletion curves (DCs), which extends the point mass and energy balance calculation by using a relationship between one selected snow state variable and the snow cover fraction (SCF) over a fixed area (Luce et al., 1999), can be applied The availability of distributed snow measurements limits the application of both solutions, with different needs for the associated spatial resolution.

Remote sensing is the best and sometimes only available distributed data source for medium to large-scale studies. Different time and spatial scales of data can be found between satellites, with a decreasing spatial resolution for a given location as frequency increases, i.e. NOAA daily images with 1 x 1 km cell size, MODIS daily images with 500 x 500 m cell size or Landsat 16-days images with 30 x 30 m cell size. These satellite sources are widely used for examining the evolution of snow cover extent on a medium to large scale (Painter et al. 2009; Herrero et al. 2011; Wang et al. 2014; Malik et al., 2014). In semiarid environments, the extremely changing conditions favor the particular distributed patterns of the snow, which usually appear as medium to small sized patches. Thus, spatial resolution constitutes a limiting factor and Landsat has been the data source most recommended for studying snow evolution over these areas (Marks and Winstral, 2001; Pimentel et at., 2012), sometimes being combined with MODIS data to fill in the time lapse at a daily scale. Nevertheless, Landsat spatial resolution is not always capable of capturing the variability of snow distribution during spring or the short melting cycles in dry years, in which small snow patches may persist during many weeks in early summer (Rosenthal and Dozier 1996; Pimentel et al. 2012; Sade et al. 2014).

Moreover, the selection of the most representative DC to expand the physical snow models calculations over grid cells in distributed studies depends on the local conditions, including topography, vegetation and the dominant regimes of the weather variables, that is, it requires the availability of SCF local measurements. Terrestrial photography (TP) is a cost-effective technique, capable of reproducing snow dynamics at the cell scale when combined with the physical model approach and point measurements of other variables, such as snow depth. Different examples of parameterization of DCs have been proposed in the literature (Ferguson 1984; Buttle and Mc Donnell 1987; Luce et al., 2004), and local SCF data from TP provide a basis for the adoption of a given curve or local parameterizations. Additionally to a high and

easily flexible spatial resolution, TP frequency can be fixed at sub-daily scales and even change within the monitoring period to be adapted to the process significant scales without effort.

Nevertheless, the final simulation of the spatial evolution of the snowpack may not result in a satisfactory performance due to the high degree of heterogeneity of the snow and the usual lack of extended time series of snow depth/cover in situ to generate specific local DCs, and the need for not only simulating snow cover but also snow depth values. The complementary use of assimilation techniques can reduce uncertainty in the model forecast, considering that field dataset for additional snow variables is available. There are many examples of snow simulation using different assimilation techniques, from simple methods such as Direct Insertion (DI) (Liston et al. 1999; Malik et al. 2012) to more complex methods such as those derived from applications of Kalman filter (Kalman 1960). In this group, a wide range of methodologies are found: the original Kalman filter, mainly used as linear forecast model; the Ensemble Kalman Filter (EnKF) (Evensen 1994), which constitutes a stochastic formulation of the original filter and simplifies the problem of the non-linearity of the process; or the Ensemble Square Root Filter (ESRFs) (Pham et al. 2001; Tippett et al. 2003 and Ott et al. 2004), which does not perturb the observation and improves the computational time.

This work presents the potential of TP for capturing snow dynamics at the subgrid scale as an intermediate step between point and distributed snow modeling, when combined with physical modeling and point measurements. For this purpose, three different DC parameterizations proposed by Luce et al. (2004) were tested at a mountainous site in southern Spain by means of the assimilation of SCF values obtained from TP into a physical snow model previously validated at the study site (Herrero et al. 2009). The Ensemble Transform Kalman Filter (ETKF) technique, belonging to the ESFRF group, has been used in this study. A cell size of 30 x 30 m was selected in order to use the results in a further validation of the distributed model in the region through Landsat data.

The article is organized as follows: section 2.2 describes the characteristics of the study site and the available data; section 2.3 introduces the different steps in the calculation structure (snowmelt-accumulation model, DC, TP analysis, and ETKF technique); sections 2.4 and 2.5 present the results and their discussion, and, finally, the conclusions are drawn in section 2.6.

## 2.2. Study site and available data

This study has been carried out in the Sierra Nevada Mountains, southern Spain. This linear mountain range, with altitudes ranging from 1500 to 3500 m, runs parallel to the Mediterranean coast at a distance of 60 km. It is characterized by high altitudinal gradients and a modification of the mountain climate influenced by the surrounding Mediterranean conditions. It is usually covered with snow, at altitudes of over 2000 m, during winter and spring, and although the snowmelt season extends from April to June, the typically mild Mediterranean winters produce several accumulation-melting cycles before the final spring melting. Annual precipitation fluctuates widely and can range from 400 to 1500 mm, with a high spatial variability throughout the area due to topographic effects. The average temperature ranges from -5 °C to 5°C during the snow season, although minimum values of -20 °C can be found at certain times in winter.

A control area of about 900 $m^2$ was selected near the monitoring weather station used in this study, Refugio Poqueira (Figure 2.1), at 2500 m.a.s.l. This area is composed of fragmented phyllites and schists, and a characteristic vegetation canopy, consisting of *Genista versicolor* and *Festuca clementei*, two compact and densely branched low shrubs that grow closely

together, forming extremely compact, low, continuous cover, which acts as an insulator between the soil and the snowpack and is the main vegetation cover from 2000 to 2900 m over this area (Anderson et al., 2011).

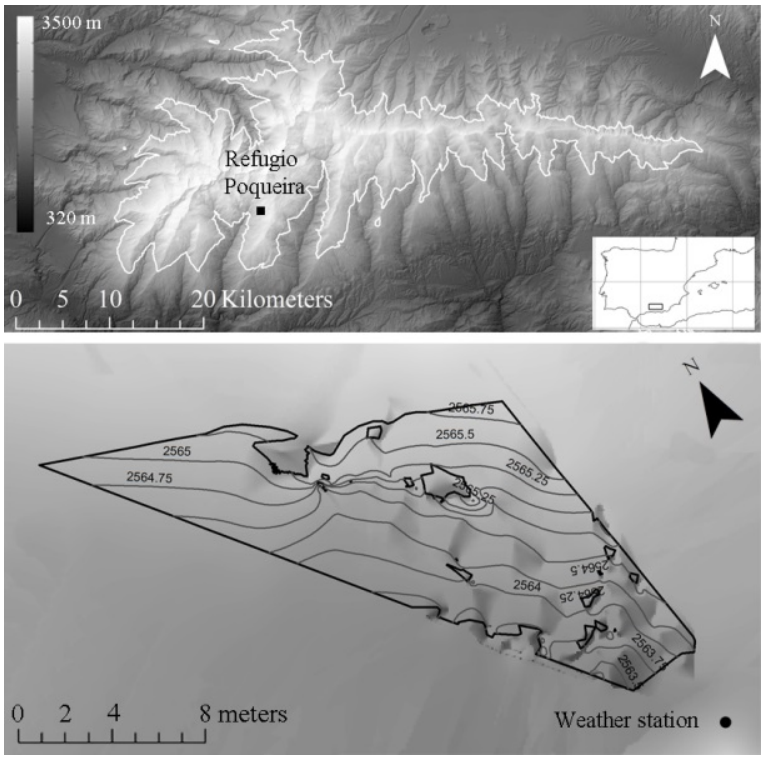


Figure 2.1 Location of the study site at Sierra Nevada Mountains, Southern Spain (top), and DEM of the control area close to the Refugio Poqueira Weather Station (below) The black dot indicates the location of the weather station and the black solid line the area covered by the images obtained from TP

### 2.2.1. Weather Data

Table 2.1 Statistics descriptors of selected meteorological variables at the Refugio Poqueira weather station during the study period (2009-2011)

| | **Mean** | **Max** | **Min** |
|---|---|---|---|
| Annual precipitation (mm $yr^{-1}$) | 750 | 1250 | 467 |
| Snowfall annual fraction (% of annual precipitation) | 60 | 70 | 40 |
| Instant temperature (ºC) | 6.4 | 24.6 | -14.4 |
| Instant winter temperature (ºC) | 1.3 | 8.5 | -14.4 |
| Solar radiation (J $m^{-2}day^{-1}$) | 19.8·106 | 35.8·106 | 0.5·106 |
| Wind speed ($ms^{-1}$) | 3.82 | 13.24 | 0.11 |

The automated weather station located at Refugio Poqueira (Figure 2.1) consists of a rain gauge with Alter shields to facilitate snow collection, a pyranometer, a pyrgeometer, a temperature and humidity probe, a wind monitor, and a manometer. 5-minute datasets have been consistently recorded since 2004 up to the present; some statistical descriptors of the weather data at this site are included in Table 1. Table 2 shows the model and main characteristics of the instrumental components of the Refugio Poqueira station.

Table 2.2 Specifications of the sensors at the Refugio Poqueira weather station

| Instrument | Range | Operating Temp (ºC) |
|---|---|---|
| Campbell CR10X Datalogger | | -25 to 50 |
| Geonor T-200B Rain gauge | 0-600 mm | -25 to 70 |
| Vaisala HMP45C. Temperature | -40 to 60 ºC | -40 to 60 |
| Vaisala HMP45C. Humidity | 0.8-100% | -40 to 60 |
| Pyranometer Kipp & Zonen SP-Lite | 0.4 – 1.1 µm | -30 to 70 |
| Druck RPT410F Barometer | 600-1100 hPa | -40 to 60 |
| Young 05103-45 Wind Monitor | 0-60 m/s | -50 to 50 |
| Pyrgeometer | 4.5 – 44 µm | -40 to 80 |

### 2.2.2. Terrestrial photography

Since the summer of 2009, an automatic CC640 Campbell Scientific camera has provided five images per day, every two hours between 8.00am and 4.00pm, of the control area, with a resolution of 640 x 504 pixels and a focal length of 85 mm. This camera is able to capture both the fast snow melting cycles and the spatial heterogeneity exhibited by the snow cover at the study site in relation to its micro-topography. Additionally, two snow measuring rods were installed in the photographed area at representative points where the snow is more persistent during most of the accumulation-melting cycles throughout the year. Thus, the TP images allow us to monitor a representative snowpack depth at the study site with high frequency recording.

### 2.2.3. Digital elevation model

A 0.05x0.05 m Digital Elevation Model (DEM) of the control area was derived from the spatial interpolation of topographic data survey. The topographic survey was designed from a previous analysis of the TP, from which the most important elements of the micro-topography that condition the snow distribution over the control area were selected.

## 2.3. Methods

Two consecutive hydrologic years, 2009-2011, were simulated at the study site by using the snow point model by Herrero et al. (2009), with three different DCs. The model was used with its original calibration, obtained with data from 2004 to 2007. Two different performances of the model were tested. First, the three DCs were evaluated by comparing TP-observed values of SCF and snow depth with their simulated results, without any assimilation procedure (open loop simulation). Second, the TP-SCF dataset (observation) was assimilated by means of ETKF for the same DC-formulations and the simulated snow depth values were validated against the TP-snow depth dataset. This section describes the different items in the calculation process: the snow model structure, the three selected DCs, how the snow variables were obtained, and the ETKF assimilation technique.

### 2.3.1. Snow modeling: Point model

The snowmelt-accumulation model for Mediterranean sites developed by Herrero et al. (2009) is a physical model based on a point mass and energy balance. The model assumes a horizontally uniform snow cover distributed in one vertical layer. This snow column per unit area defines a control volume, with the atmosphere and the ground as external boundaries; the

lateral mass and energy fluxes between adjacent snow columns are null since the horizontal gradients are neglected when compared to the vertical ones. The balance equations can then be expressed according to:

$$\frac{d\,SWE}{dt} = P - E + W - M \tag{2.1}$$

$$\frac{d(SWE \cdot u)}{dt} = \frac{dU}{dt} = K + L + H + G + P \cdot u_P - E \cdot u_E + W \cdot u_W - M \cdot u_M \tag{2.2}$$

where *SWE* (snow water equivalent) is the water mass in the snow column, and *u* is the internal energy per unit of mass (*U* for total internal energy). In the mass balance, *P* defines the precipitation rate, *E* is the flux of water mass exchange with the atmosphere (positive for evaporation from the snowpack/negative for condensation from the atmosphere), *W* represents flux of water mass transport due to wind, and *M* is the melting water flux. In addition, for the energy fluxes in Eq. (2.2), *K* is the net solar or short wave radiation flux, *L* the net thermal or long-wave radiation flux, *H* the flux of sensible heat exchange with the atmosphere, *G* the flux of sensible heat exchange with the ground, and $u_P$, $u_E$, $u_W$, and $u_M$ are the unitary energy values associated with each one of the mass fluxes involved in Eq.(2.1) $W \cdot u_W$ and $M \cdot u_M$ are advective terms and $E \cdot u_E$ and *H* are diffusive transport terms, whose formulation requires some characterization of the turbulent atmospheric conditions (Anderson 1976; Jordan et al. 1999). *SWE* values are transformed into snow depth values by means of a local empirical relationship for the experimental measurements.

Some simplifying assumptions were proposed when applying Eqs. (2.1) and (2.2) at the study site. The wind transport term, *W*, was disregarded due to the quick snow metamorphosis, which compacts the snow and reduces its mobility. *G* was also disregarded since, besides being considered a secondary term *per se* in the energy balance (Kuusisto 1986), its value is considerably reduced at this site by the insulating properties of the local vegetation canopy. *P* is direct input from the dataset measured by the weather station. In addition, the terms, *K*, *L*, $E \cdot u_E$ and *H* can be explained as:

$$K = K\downarrow + K\uparrow = K\downarrow (1 - \alpha) \tag{2.3}$$

$$L = L\downarrow + L\uparrow = L\downarrow - \sigma_{SB} \cdot T_{sn}^4 \tag{2.4}$$

$$U_E = \left( \frac{K_{U_E}}{\phi_M \cdot \phi_V} \cdot v_a \right) \cdot \left( e_{sn} - e_a \right) \tag{2.5}$$

$$H = \left( \frac{K_H}{\phi_M \cdot \phi_H} \cdot v_a + K_{H0} \right) \cdot \left( T_a - T_{sn} \right) \tag{2.6}$$

where $K\downarrow$ and $K\uparrow$ are downwelling and upwelling short radiation fluxes, $K\downarrow$ is measured directly by the weather station; $\alpha$ is the snow albedo, which in this study is considered to be constant with a value of 0.8; $L\downarrow$ and $L\uparrow$ are downwelling and upwelling long radiation fluxes, where $L\downarrow$ is also measured directly by the weather station; $U_E = E \cdot u_E$; $K_{UE}$ is the bulk latent-heat transfer coefficient, which depends on average roughness of the snow $z_0$; $K_H$ is the bulk sensible-heat transfer coefficient with wind and $K_{H0}$ the same without wind; $v_a$, $e_a$, and $T_a$ are,

respectively, the wind speed, the air vapor pressure, and the air temperature at a reference altitude $z_R$ (typically 2 meters); $e_{sn}$ is the saturation vapor pressure for the snow temperature, $T_{sn}$; and $\phi_M$, $\phi_V$ and $\phi_H$ are the stability-correction factors for non-adiabatic temperature gradients for mass, wind and sensible heat, respectively (Dingman, 2002). In this work, the conclusions from Herrero et al. (2009) for snow dynamics at the study site were adopted, with values of $6\ Wm^{-2}K^{-1}$ for $K_{H0}$, 2.5 mm for $z_0$ and the terms $\phi_M$, $\phi_V$ and $\phi_H$ were disregarded.

### 2.3.2. Depletion curve

DCs are used to expand the point snow calculations over the cell size area selected as a previous step in the distributed modeling of the snowpack, taking into account the spatial variability at the subgrid scale. These empirical functions relate the SCF (the fraction of cell area covered by the snow) to other snow variables. During an accumulation-melting cycle, the selected DC includes the decrease in snow cover within the cell area and, therefore, affects the quantification of energy fluxes in the energy balance. These fluxes are reduced proportionally to the fraction of the area covered by the snow. Thus, it is important to select a suitable DC when applying the model.

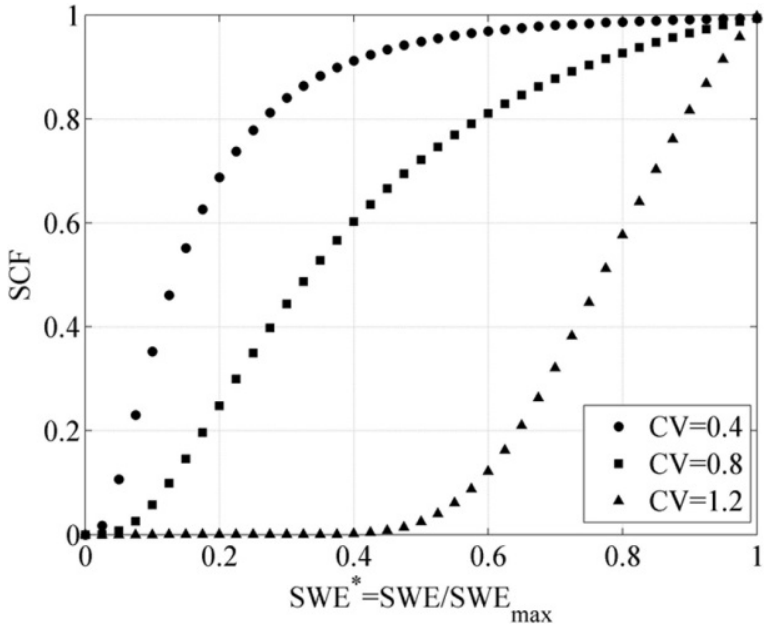


Figure 2.2 Different dimensionless DCs parameterized as lognormal distribution for different coefficients of variation (CV).

Different methodologies have been employed to define these curves. For example, Cline et al. (1998) used remote sensing data to generate DCs under the assumption that the SCF decrease over time was spatially coherent - in other words, the snow did not change its location; Luce and Tarboton (2004) employed a probability density function of *SWE* for the peak accumulation date over a basin; or Kolberg et al. (2006), who applied a Bayesian approach to update these curves using remote sensing data. However, most of the DCs proposed relate SCF and *SWE*, with rare exceptions.

Following this, the DC shapes proposed by Luce and Tarboton (2004) from different distribution functions were tested at the study site to select the formulation that most closely resembled most of the in-season melting cycles that characterize snow dynamics in Mediterranean climates. A lognormal distribution was finally chosen. Three parameterizations

described by their coefficient of variation (CV) were adopted for a lognormal distribution between the dimensionless variables of snow water equivalent, *SWE** ($SWE^* = SWE/SWE_{max}$, where $SWE_{max}$ is the *SWE* maximum in each melt cycle), and SCF, in the control area (Figure 2.2).

The CV represents the main trend in the evolution of areal accumulation-melting. Lower values were associated with a higher sensitivity of SCF to changes in *SWE** in the first stage of the accumulation and in the last stage of melting processes, whereas high CV values correspond to low sensitivity of SCF during the initial stages of snow accumulation but with quick changes in SCF during the initial stages of melting. At the spatial scale of the present study (30 x 30 m), the snow properties, together with the microtopography and ground vegetation at a given site, among others, are the underlying factors for a given DC shape representing local conditions.

### 2.3.3. Terrestrial photography analysis

To quantify the evolution of snow at the subgrid scale, TP observations were obtained at the study site during two consecutive hydrologic years (2009-2011). Every TP image underwent a two-step analysis: georeferencing, to provide the image with spatial coordinates, followed by a snow detection process using a non-supervised clustering algorithm, which provided both the SCF and snow depth for each image. Both steps are described below.

#### Georeference

The georeference of each image was made on the basis of the local DEM, whose quality together with the image quality (level of distortion induced by the lens during the acquisition process) determined the final accuracy of the results.

First, the images were lined up to correct possible displacements during the acquisition process. Secondly, the corrected images were georeferenced to a DEM following standard procedures for viewing with computer graphics (Fiume et al. 1989; Foley et al. 1990), which relate the two-dimensional pixels in the images to the three-dimensional points in the DEM. This mapping function translates the coordinate system of the DEM to the camera position and applies a transformation according to the focal length and view direction. The result is a virtual photograph of the DEM, that is, a representation of it as it would be seen from the point of view of the camera. The two-dimensional representation of the DEM is then scaled according to the resolution of the photograph (Corripio 2004; Rivera et al. 2008). In this way, the two representations can be superimposed; establishing the necessary correspondence between a pixel in the photograph and its projection coordinates in the DEM. The final result is a map in which all the pixels in the TP have been located over the terrain.

#### Snow detection

To distinguish the snow-covered and non-covered pixels in each image, a clustering algorithm was applied. These unsupervised methods are generally used to group together data according to some certain notion of similarity. In this case, all the white points in the scene are linked to the presence of snow, so that two clusters can be easily defined: snow-cover and non-covered pixels. A K-mean clustering (MacQueen 1967) was selected; this algorithm classifies the data into a given number of clusters, selecting a random center within each cluster and minimizing the distance between the data and these centers. This algorithm proved to be efficient enough to differentiate these two kinds of pixels, since it was capable of detecting most of the snow area

with no previous calibration or the use of fixed thresholds in the images, with a resulting low level of misclassifications, which were in turn related to the presence of strong shadows in the images (Pimentel et al. 2012). From this pixel classification, the SCF can be easily calculated.

This algorithm was also used to measure the snow depth from the rods installed in the control area. The rods were painted in a distinct color, red, which made them easy to differentiate from the remaining objects in the scene. From the clustered results, a linear equation was capable of estimating the depth of the snow from the identified pixels with rods.

### 2.3.4. Ensemble Transform Kalman Filter (ETKF)

As stated before, the data assimilation method employed in this work is the ETKF. This filter was introduced by Bishop et al. (2001) as a form of square root filter that allows a deterministic update of the ensemble anomalies (Tippett et al. 2003), and it is usually chosen for its natural characteristics and its computational efficiency (Sakov and Oke 2008). It is based on the equations of the Kalman filter and the Monte Carlo perturbation of the EnKF.

The Kalman filter analysis equations represent the state variable update from the assimilation process and they can be described as:

$$\mathbf{x}^a = \mathbf{x}^f + \mathbf{K}(\mathbf{d} - \mathbf{H}\mathbf{x}^f) \tag{2.7}$$

where $\mathbf{x}^a$ is the analysis and $\mathbf{x}^f$ the forecast; $\mathbf{d}$ is the vector observation; $\mathbf{H}$ is the operator mapping the state vector space to the observation space; and $\mathbf{K}$ is referred to as the Kalman gain, given by:

$$\mathbf{K} = \mathbf{P}^f \mathbf{H}^T (\mathbf{H}\mathbf{P}^f \mathbf{H}^T + \mathbf{R})^{-1} \tag{2.8}$$

with $\mathbf{P}^f$ and $\mathbf{R}$ the forecast and observation error covariance matrixes, respectively; the superscripts $f$ and $a$ denote forecast and analysis, respectively, and the superscript $\mathbf{T}$ denotes a matrix transpose.

These are the basic equations also used by EnKF, but this one employs a Monte-Carlo approximation to solve the problem of the non-linearity of the model used. The covariance matrix $\mathbf{P}$, in this case, is stored and manipulated implicitly via an ensemble variable $\mathbf{X}$ of the model states, $\mathbf{X} = [\mathbf{X}_1, ..., \mathbf{X}_m]$, with $m$ being the ensemble size, by means of using the relationship:

$$\mathbf{P} = \frac{1}{m-1}\sum_{i=1}^{m}(\mathbf{X}_i - \mathbf{x})(\mathbf{X}_i - \mathbf{x})^T = \frac{1}{m-1}\mathbf{A}\mathbf{A}^T \tag{2.9}$$

where $\mathbf{x}$ is the ensemble mean:

$$\mathbf{x} = \frac{1}{m}\sum_{i=1}^{m}\mathbf{X}_i \tag{2.10}$$

and $\mathbf{A} = [\mathbf{A}_1, ..., \mathbf{A}_m]$ is the ensemble of the individual anomalies or perturbations,

$$\mathbf{A}_i = \mathbf{X}_i - \mathbf{x} \tag{2.11}$$

Based on these equations, Sakov et al. (2009) defined the ETKF by rewriting the general analysis equation given by Eq.(2.7) in a generic form

$$\mathbf{x}^a - \mathbf{x}^f = \mathbf{A}^f \mathbf{G}\mathbf{s} \tag{2.12}$$

where $\mathbf{s}$ is the scaled innovation vector defined as

$$\mathbf{s} = \mathbf{R}^{-1/2}\left(\mathbf{d} - \mathbf{H}\mathbf{x}^f\right)\Big/\sqrt{m-1} \tag{2.13}$$

and **G** stands for

$$\mathbf{G} = \mathbf{S}^T\left(\mathbf{I} + \mathbf{S}\mathbf{S}^T\right)^{-1} \tag{2.14}$$

with $\mathbf{S}$ being the term that represents the scaled ensemble observation anomalies:

$$\mathbf{S} = \mathbf{R}^{-1/2}\mathbf{H}\mathbf{A}^f \Big/ \sqrt{m-1} \tag{2.15}$$

In this annotation, the anomalies of the ensemble update are calculated as

$$\mathbf{A}^a - \mathbf{A}^f = \mathbf{A}^f \mathbf{T} \tag{2.16}$$

with $\mathbf{T}$ being the transform matrix for ETKF proposed by Bishop et al. (2001)

$$\mathbf{T} = \left(\mathbf{I} + \mathbf{S}^T\mathbf{S}\right)^{-1/2} - \mathbf{I} \tag{2.17}$$

In this work, the platform EnKF-Matlab (version 0.28) developed by Sakov (http://enkf.nersc.no/Code/EnKF-Matlab/) was used to implement the aforementioned development of ETKF.

Two aspects must be taken into account to apply the ETKF: model error estimation and optimal ensemble size. In that case, due to the deterministic aspect of the filter, observation error estimation is not considered.

The determination of model errors remains a largely subjective issue, as it is very difficult to attribute the error to the physics of the model (Reichle 2008). One way to quantify this model error is by including the uncertainties in both the forcing of the data and the model formulation (Reichle et al. 2008). In this study, a representative value of the variability was employed to perturb the forcing parameters. Considering that the time resolution of the meteorological data was 5 minutes and according to the time step of the modeling, 1 hour, the standard deviation of the data was calculated every hour. The 90th percentile of the standard deviation sample obtained was selected as the representative value to perturb all the meteorological inputs, with the exception of precipitation. In this case, when the measured precipitation was zero, no perturbation was performed; the rest of the measured values were divided into three intervals, whose limits depended on the amount of precipitation, and a standard deviation was calculated for each one. Table 2.3 shows the different representative values employed for perturbing each weather variable.

Table 2.3 Representative values used to perturb the different meteorological variables used in the modeling

| Meteorological input | | Representative value |
|---|---|---|
| Temperature (°C) | | 0.663 |
| Emissivity (%) | | 10.00 |
| Wind speed (m $s^{-1}$) | | 1.363 |
| Air pressure (KPa) | | 0.049 |
| Air relative humidity (%) | | 6.65 |
| Radiation (J $m^{-2}$ $s^{-1}$) | | 110.5 |
| Precipitation (mm) | $P = 0$ | *no perturbation* |
| | $0 < P < 2$ | 0.496 |
| | $2 \leq P < 5$ | 0.810 |
| | $5 \leq P$ | 2.568 |

To select the optimal ensemble size, different simulations with ensembles of 10, 20, 50, 100, and 200 members were performed. The ensemble size that minimized the Root Mean Square Error (RMSE) between observation and simulation was finally adopted as the optimal one. The RMSE for a given ensemble size was calculated as the mean of the RMSE of the simulation of three different DCs performed.

## 2.4. Results

### 2.4.1. Snow variables measured

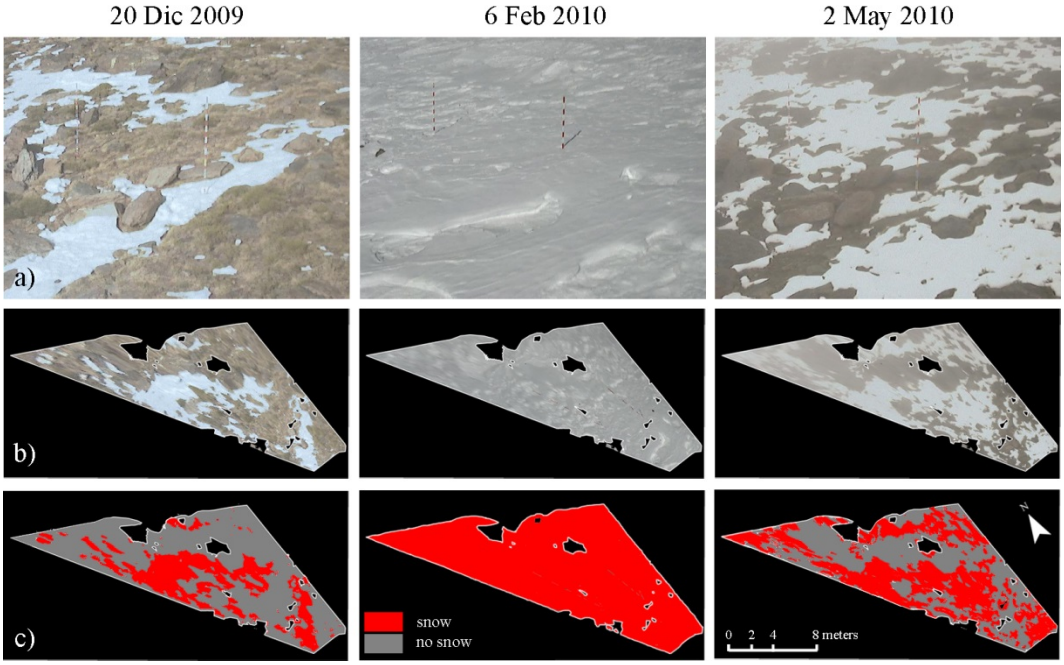


Figure 2.3 Example of the TP georeference process at the study site for selected days during the snow season. a) Original image; b) Georeferenced image; c) Snow mask obtained from the georeferenced image by using the simple K-mean algorithm described in section 2.3.3

About 2000 images from the study period, the two hydrologic years 2009-2010 and 2010-2011, were georeferenced using the DEM obtained in the control area. The results of this process were snow cover maps in the photographed areas, with the same spatial resolution of the DEM (0.05m x 0.05 m) and with the same temporal resolution of the image acquisition process (5 images per day). Figure 2.3 shows different examples of this georeference process.

As can be observed, the snow was correctly detected at different times of the year under different weather conditions: on clear days at the beginning of the snowy season (9 Dec. 2010); on days with a total snow cover and the appearance of shadows (6 Feb. 2011); or on days with a morning mist at the end of the fusion periods (2 May. 2011), which confirmed the usefulness of TP at the scale of the work analyzed. Table 4 shows some statistics of the snow state variables measured using these images.

Table 2.4 Statistics descriptors of the snow state variables measured using TP

| **Snow depth (mm)** | | **SCF** | |
|---|---|---|---|
| min | 0 | days completely covered by snow | 162 |
| max | 1400 | days completely free of snow | 73 |
| mean in days with snow | 612.9 | days partially covered by snow | 401 |
| std in days with snow | 125.2 | days without information | 94 |

Moreover, the high temporal resolution of TP allowed the monitoring of some characteristic fast evolution that usually takes place in this area, mainly during the melting season. Figure 2.4 a) shows the average hourly rate of change in SCF, with the highest rate from autumn initial snow and spring melting of the second year, maximum value of 0.065 $m^2m^{-2}h^{-1}$ (26 Nov 2010); medium range from some winter period and spring melting of the first year, maximum rate of 0.025 $m^2m^{-2}h^{-1}$ (24 Apr 2010); both greatly contrasting with periods with negligible values during some winter periods. Figure 2.4 b) includes a comparison between TP-SCF values (small black dots) and SCF values obtained from different remote sensing sources in the study area at the adequate scale and given dates: a) Landsat, providing covered/non covered pixel classification from Normalized Difference Snow Index (NDSI) values (gray dots), and b) MODIS, providing SCF from MOD10A1 product (black crosses). In general, none of them is able to reproduce the global variability exhibited by snow during given periods, which can be observed from TP. MODIS-SCF values, which covered a greater extension that the cell size, match TP observations during covered periods but not during the melting season (e.g. spring melting cycle of 2010, which is prolonged by MODIS for approximately one month); on the contrary, Landsat classification reproduced this period best but its temporal resolution clearly limited the monitoring of quick changes (e.g. the absence of data during the spring melting of the second year). The potential of TP observations as a complementary data source to these remote sensing sources can be clearly observed.

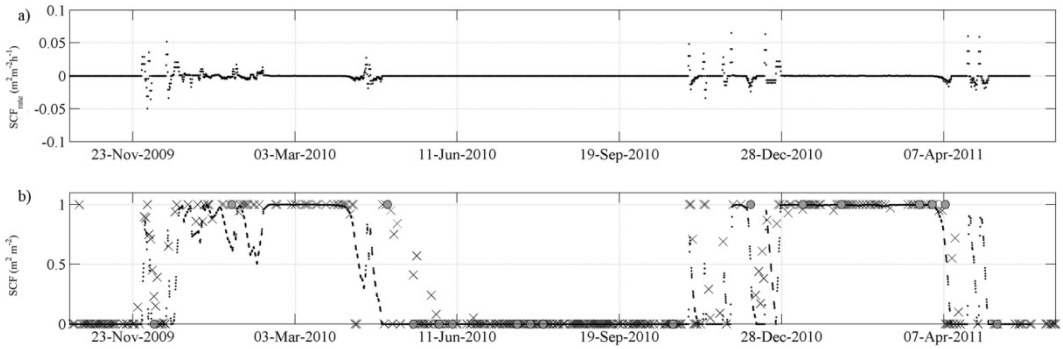


Figure 2.4 a) Average hourly rate of change in SCF throughout the study period b) Comparison between SCF obtained from TP (black dots), Landsat (gray dots) and MODIS (black crosses).

### 2.4.2. Open loop simulation

Figure 2.5 and Figure 2.6 show, respectively, the evolution of SCF and snow depth simulated by the snow model for the three DCs used, and their comparison with the TP-measurements; dispersion graphs are also included in the figures.

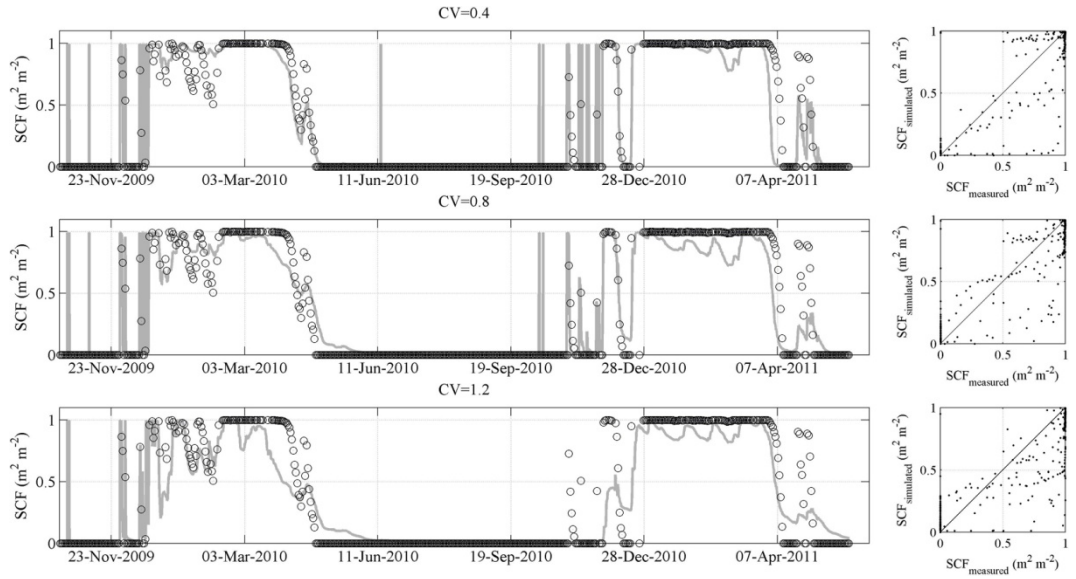


Figure 2.5 Measured (black dots) and simulated open-loop (gray line) SCF evolution for each depletion curve used by the snow model without assimilation (left). Dispersion graphs between measured and simulated SCF (right).

The SCF open-loop simulation (Figure 2.5) produced similar trends for every DC. As a general trend, the DCs with CV=0.4 and CV= 0.8 reproduced, with a high approximation, the behavior of the snow during the whole period with RMSE=0.151 $m^2m^{-2}$ and RMSE=0.145 $m^2m^{-2}$, respectively; and they were even capable of capturing small fusion-accumulation cycles at the beginning and end of the season. The DC curve with CV=1.2 also reproduced long periods with persistent snow adequately, but, however, could not approximate those short, intense cycles at the beginning and end of the annual snow period. A larger error (RMSE=0.190 $m^2m^{-2}$) than previous DCs for the study period was found.

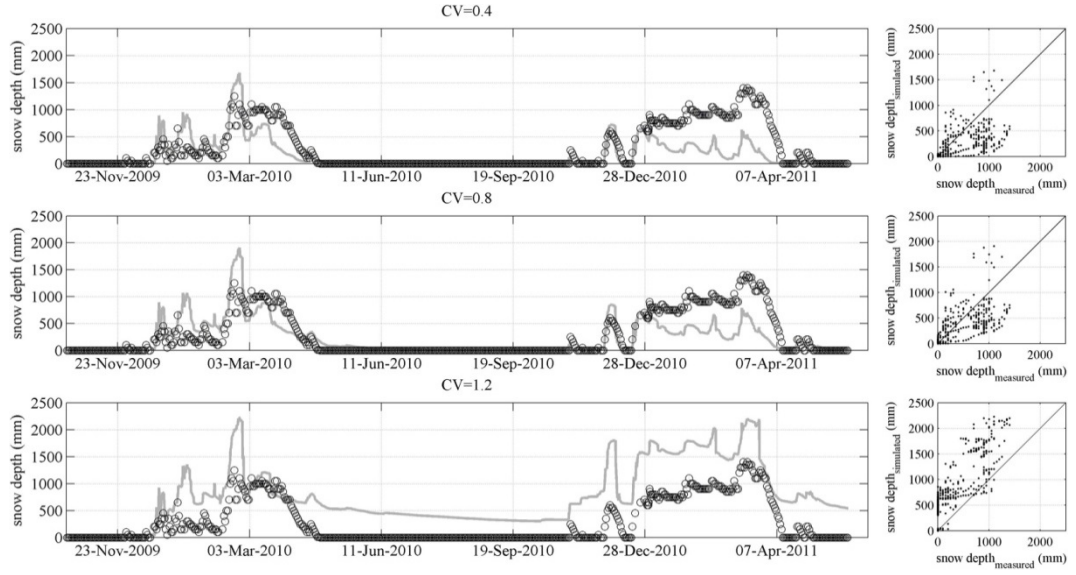


Figure 2.6 Measured (black dots) and simulated open-loop (gray line) snow depth evolution for each depletion curve used by the snow model without assimilation (left). Dispersion graphs between measured and simulated snow depth (right).

A similar behavior can be observed for the simulated snow depth evolution (Figure 2.6). As a general trend, the DCs with CV=0.4 and CV=0.8 underestimate the depth of the snow. During the two years selected, both reproduce with a reasonable approximation the snow depth during the snow season up to the beginning of the spring accumulation period. From then on, both curves give rise to greater fusion fluxes than those observed, mismatching the measured and simulated snow depth results. Conversely, the curve with CV=1.2 overestimates the depth in a generalized manner during the study period, and even generates the presence of snow during the summer season, when nil snow is observed.

### 2.4.3. TP-SCF assimilation simulation

TP-SCF values were used as the observation dataset in the assimilation process. First, the ETKF was calibrated by minimizing the mean RMSE values associated with each DC for a different number of ensemble members (Table 5). It can be seen how the greater the size, the smaller the error, with very significant improvements in the simulation at the beginning of the interval of sizes evaluated (for example, the error produced was reduced to almost one third depending on whether a filter of 10 or 20 members was selected), and a certain stabilization of its value as from a certain size threshold was noted. In view of these results, a size of 20 members was chosen as being optimal for the goodness of the simulation and the associated computational cost, since, starting from this value, the diminution of the associated error was hardly noticeable (O~0.01 $m^2 m^{-2}$ for the SCF).

Table 2.5 RMSE values for SCF estimations with different ensemble sizes. For a given size, the RMSE is calculated as the averaged RMSE values associated with each depletion curve.

| **Ensemble Size** | **$RMSE_{SCF}$ ($m^2m^{-2}$)** |
|---|---|
| 10 | 0.351 |
| 20 | 0.257 |
| 50 | 0.248 |
| 100 | 0.251 |
| 200 | 0.253 |

The simulated snow depth values were tested against the independent snow depth observations (Figure 7), with a decrease in the RMSE values in all the cases when compared to the open-loop simulations (Table 6, and Figures 6 and 7), especially for CV=0.4 and CV=0.8 curves. However, it should be pointed out that, in spite of this global improvement, the assimilation was not able to reproduce the snow depth (Figure 7) with the same degree of approximation for all the accumulation-melting cycles during the study period. This is clear in the case of the DC with CV= 1.2, in which snow presence during the summer season continues to be simulated without actually being observed, resulting in high global RMSE values. Also, CV=0.4 and CV=0.8 curves reproduced the initial and final stages of every annual snow season better, but failed to simulate some intermediate periods, with significant differences between both curves depending on the season and cycles being analyzed. On the whole, despite the major improvement experienced in the three DCs analyzed, the DC with intermediate CV (CV=0.8) was the one which best represented the observations, with a RMSE value of 191.18 mm over the whole study period (equivalent to a 30% of the mean snow depth), against the 279.23 mm and 523.14 mm values obtained for the CV=0.4 and CV=1.2, respectively (equivalent to a 45% and 85% of the mean snow depth, respectively).

Table 2.6 RMSE associated with the comparison between model-assimilated and TP-measured values of snow depth for each depletion curve in the open loop and TP-SCF assimilation simulations (CV=coefficient of variation)

| | **CV=0.4** | **CV=0.8** | **CV=1.2** |
|---|---|---|---|
| $RMSE_{\text{snow depth, open loop simulation}}$(mm) | 321.26 | 285.37 | 555.96 |
| $RMSE_{\text{snow depth TP-SCF assimilation simulation}}$(mm) | 279.23 | 191.18 | 523.14 |

TP-SCF assimilation has allowed both the analysis of the DC that best reproduced the snow dynamics at the subgrid scale and the improvement in the physical model performance. The incorporation of these observations in the modeling by ETKF led, in all cases, to a reduced error in the modeling, situating it within acceptable ranges. To evaluate the degree of improvement of the assimilation in the modeling, a dimensionless performance index, $IND_{Perf}$, was defined as:

$$IND_{perf} = \frac{RMSE_{without\ assimilation} - RMSE_{with\ assimilation}}{RMSE_{without\ assimilation}} \tag{2.18}$$

where $RMSE_{without\ assimilation}$ and $RMSE_{with\ assimilation}$ are, respectively, the errors between observed-simulated values of snow depth with and without assimilation; this index typically ranges between 0 and 1, with increasing values for the higher degrees of improvement. For the three DCs studied, the assimilation improved the simulated values of the snow depth over a 25%, with $IND_{Perf}$ values of 0.13, 0.39 and 0.05 for the curves with CV=0.4, 0.8 and 1.2, respectively. Obviously, a greater improvement was observed for the simulated SCF values, since this variable was directly assimilated, with $IND_{Perf}$ values of 0.60, 0.66 and 0.50 respectively for each curve, being these results an indirect indicator of the correct implementation of the methodology.

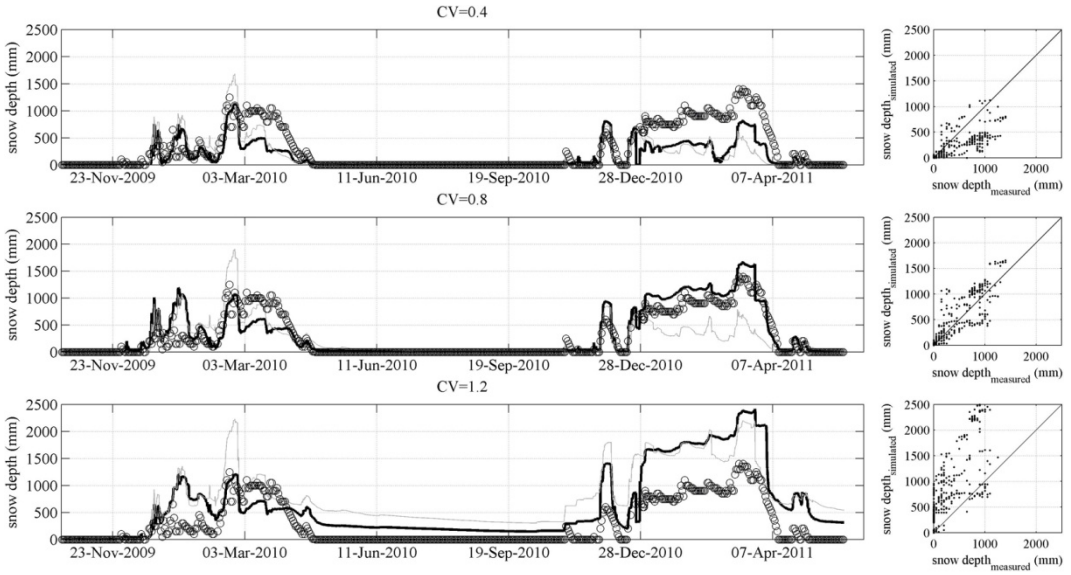


Figure 2.7 Measured (black dots), simulated (gray line), and ETKF-assimilated (black line) snow depth evolution for each depletion curve used by the snow model (left). Dispersion graphs between measured and assimilated snow depth (right)

## 2.5. Discussion

The results shown in the previous section demonstrate the importance of selecting one or other of the DCs in order to model the snow state variables correctly. The shape of these curves is closely related to the physics of the process. Hence, the curve of the highest CV (CV=1.2)

represents a very fast initial melting process, which slows down in its final stage, leaving important amounts of snow concentrated in small areas of land. This could explain the overestimation of the depth produced during the summer season, which, in turn, conditions the results of the second year, so that the use of this DC to parameterize subgrid variability was disregarded. In contrast, the other curves with lower CV values (CV=0.4 and CV=0.8) enable the snow to stay longer covering a larger area, and producing fast melting after crossing a certain threshold, which seems to be more adequate for the conditions at the study site. According to the RMSE values shown in Table 6, the DC with CV=0.8 represents the best global performance of the snow model. Nevertheless, in Figure 7, different trends can be observed between both simulations depending on the type of accumulation-melting cycle throughout the year. To address this, two different situations were identified during the study period, and the RMSE values associated with each of them were calculated: a) short accumulation-melting cycles, that are associated with sporadic snowfall occurrence at the beginning and end of the hydrologic year, usually over non-highly covered conditions; and b) large accumulation-melting cycles during the central part of the snow season. Table 7 shows the RMSE values calculated for both DCs during each cycle period. Hence, in spite of the similarity between both DCs, small aspects can be differentiated. DC with CV=0.4 produces faster decreasing rates than DC with CV=0.8, and is capable of reproducing short accumulation-melting cycles, but cannot maintain the snow presence until the end of the melting period. The RMSE for snow depth is reduced by up to approximately 50% for both types of conditions when the appropriate curve is selected (Table 7). Moreover, these trends are closely related to the conditions of the state of the snow that can be found during each kind of cycle. The snow is usually slightly compacted during short cycles and much more metamorphosed and compacted during longer cycles, especially at the end stages. These results point to the convenience of adopting a selective DC parameterization depending on the succession of accumulation-melting cycles in the snow season in these highly variable environments.

Table 2.7 RMSE associated with the comparison between model-assimilated and TP-measured values of snow depth and SCF for each depletion curve (CV=coefficient of variation) and for different accumulation-snowmelt periods

| | **CV=0.4** | **CV=0.8** |
|---|---|---|
| $RMSE_{\text{snow depth large periods}}$ (mm) | 463.87 | 261.21 |
| $RMSE_{\text{snow depth short periods}}$ (mm) | 128.50 | 234.22 |

Following this, an optimal performance of the assimilation-modeling process could be obtained by selecting the CV=0.4 curve from November 2009 to early March 2010, and shifting to the CV=0.8 until the end of this hydrologic year, to recover the CV=0.4 curve for the initial sporadic snowfall events and then the CV=0.8 curve from the end of December 2010 on. The assimilation process made it possible to overpass the initial overestimation of the simulated snow depth values during the short cycles in 2009 and the initial stage of the long cycle in the winter of 2010 (Figure 5), with any DC, resulting in a really high approximation when the CV=0.4 curve was adopted and TP-SCF values were assimilated (Figure 7). Similarly, the initial underestimation of the simulated snow depth values during the long, persistent cycle in winter and spring 2011 (Figure 6) was greatly improved by the CV=0.8 curve and the assimilated TP-SCF values. Analyzing the terrestrial images and the weather data during both periods (Figure 8) it can be observed that for the first periods (an example is shown in Figure ~~9~~ 8a) the wind recorded during the night of 19 and the morning of 20 Feb 2010 (mean velocity of 15m/s) redistributes the snow in the area, whit a decrease of 500 mm.

For the second period selected (Figure 8b) the precipitation in the form of snow taking place (35 mm) is not sufficient to justify the increase in depth observed in the measurements on 31 Dec 2010 (300 mm), nor is the temperature high enough to cause the subsequent decrease observed on 1 Jan 2011 (100 mm). However, the intensity of the wind recorded on those days (8 m/s) reached fresh and not yet consolidated snow, causing its important redistribution. The snow model used does not incorporate the redistribution action caused by the wind (see section 3.1) and, therefore, does not reproduce those variations in snow depth which are fundamentally due to this agent. The assimilation of TP-SCF data is able to partially correct this absence of wind transport in the physical model, as shown by the ETKF-simulated snow depth values for those conditions (Figure 7).

However, despite these considerations, some significant mismatches in the simulation of snow depth still persisted during the spring of 2010 and, to a lesser extent, in the winter of the 2010-2011 hydrologic year in the ETKF simulations (Figure 7). An additional explanation for this could lie in the performance of the snowfall occurrence simulation made by the model, as the detailed joint analysis of the weather dataset and the TP observations seem to indicate, but no further conclusions can be derived from the present results. All in all, the usefulness of TP data for analyzing the variability of snow at the subgrid scale and improving the physical model performance has been highlighted, in terms not only of SCF assimilation values and DC selection, but also of gaining insight into the significant processes at high resolution time scales in these variable semiarid environments.

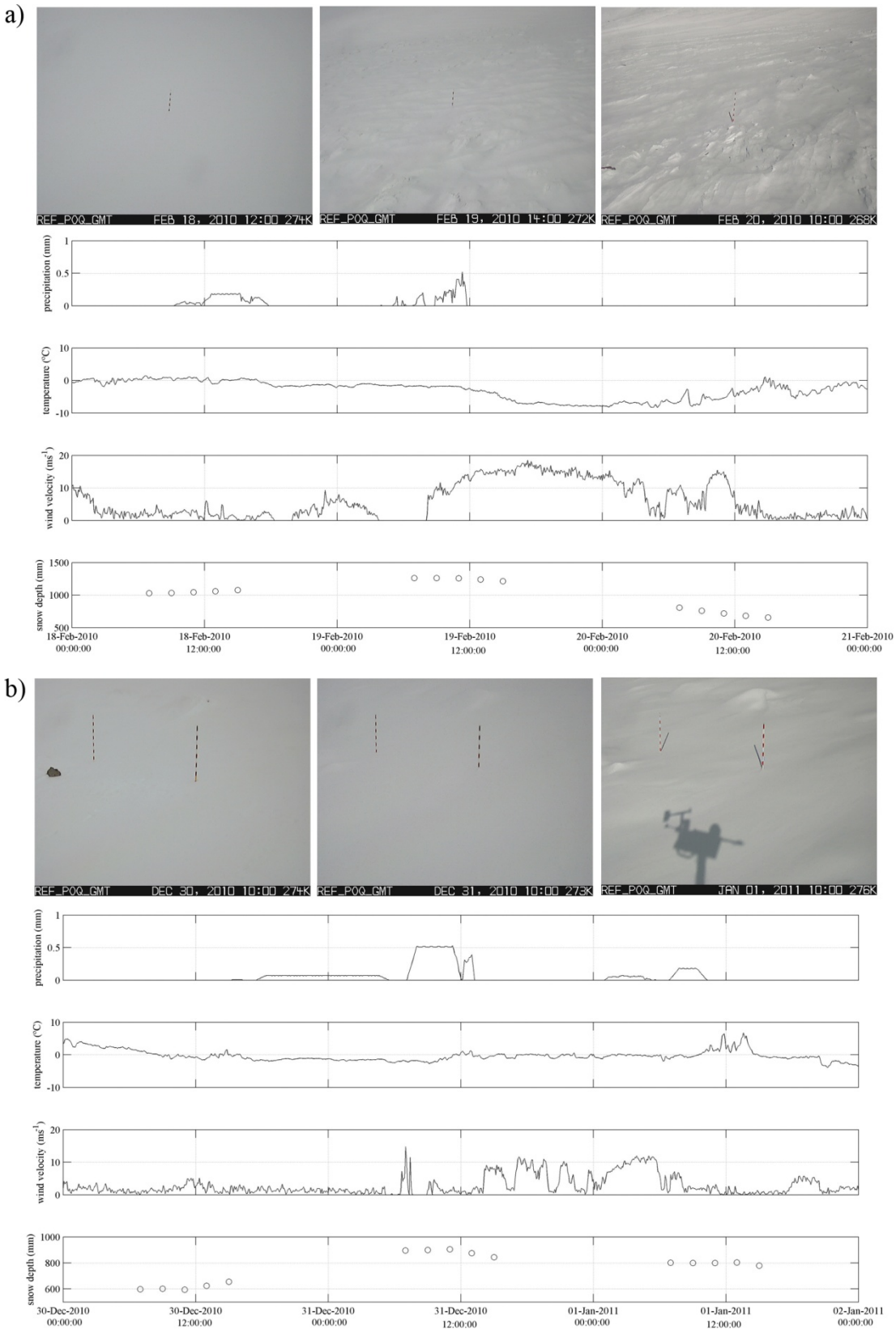


Figure 2.8 Representation of TP images, weather data (5-minutes precipitation, temperature and wind velocity) and measured snow depth during two periods where the assimilation results overpass the initial overestimation of the simulated snow depth: a) from 18 Feb 2010 to 21 Feb 2010 and b) from 30 Dec 2010 to 2 Jan 2011.

## 2.6. Conclusion

The use of TP to study the evolution of snow cover has permitted the continuous monitoring of that layer, adapted to the spatial and temporal scale of the physical processes and has proved to be a simple and economical way to obtain detailed measurements both of SCF and of snow depth. This study shows that disposing of this type of information is especially relevant in highly variable environments like the Mediterranean, in which the great heterogeneity presented by the snow layer requires detailed analysis at a local scale, during given periods whose conditions cannot be captured by conventional remote sensors alone. Specifically, the TP observations allowed the assessment of DC parameterizations over the study site.

The incorporation of this detailed information into the snow modeling process by means of the data assimilation technique selected, ETKF, significantly improved the simulations of snow dynamics at the subgrid scale made with the physical accumulation-melting snow model previously calibrated at the study site. This prevented some of the mismatches that occur at certain moments during the snow season under either highly variable conditions or processes not explicitly included in the physical modeling, which are then extended over the rest of the season, thus affecting the overall goodness of the simulation. The TP-SCF assimilation has permitted us to choose the DC which best reproduces the fusion processes taking place in this type of environment from those proposed in the literature. In this pilot area selected in Sierra Nevada (Spain) in particular, two optimal curves have been identified to better reproduce the change rate of snow variables depending on the kind of cycle taking place and the presumably associated characteristics of the snow, consolidated or not-so-consolidated, with the CV=0.8 and CV=0.4 DCs proposed by Luce et al. 2004 associated with each snow state, respectively. Both curves allowed the total cover of the area to be maintained during the first melting process stages, increasing the speed of the melting process in its intermediate stage and keeping a small fraction covered in its final stage. Nevertheless, over the whole study period, the CV=0.8 curve performed better in the simulations both with and without TP-SCF values assimilation. However, the results point to the adoption of a selective curve procedure depending on the occurring snow cycle as the optimal simulation process.

This type of dynamics is associated, on the one hand, with the type of local micro-relief, and, on the other, with the order of magnitude of the maximum depth of snow accumulated during the annual period. Despite the improvement produced when significant snow transport events occur due to the action of the wind, the TP-SCF values assimilation is not always capable of sufficiently mitigating the mismatch of the modeling for given periods. Further analyses should be made to identify the reasons behind this fact. This demonstrates the importance of this atmospheric conditioning for modeling the snow layer in these highly variable situations. It also indicates the usefulness of having DCs derived directly from local observations under these conditions available, as well as of implementing assimilation techniques of snow maps for the simulation of their distribution at higher spatial scales than that of this work. On both these work lines, TP constitutes an economical and efficient complementary source of data to be combined with remote sensing sources for distributed snow modeling, and provides the required resolution to provide information on the significant processes at the subgrid scale. The cost-efficiency of TP makes this technique a feasible and convenient one to be included in conventional weather monitoring stations in mountainous areas in semiarid environments.

# CHAPTER 3: Subgrid parameterization of snow distribution in a Mediterranean site using terrestrial photography

*Subgrid variability highly conditions the results in snowmelt-accumulation modelling. Snow depletion curves, which summarize the relationship between snow cover distribution and other snow state variables, are usually employed to represent these processes. This study proposed the use of terrestrial photography, whose scales can be adapted to the study processes, to define local snow depletion curve. Snow cover fraction and snow depth are the two datasets employed for this definition. A flexible sigmoid function employed in the study of plant growth is used to define these curves. Four depletion curves are proposed to capture the high variability shown by several snowmelt cycles throughout the years. Each of them represents different snowmelt cycles: 1) cycles with a high accumulated snow depth which came from a metamorphosed snow; 2) cycles with great snow depth preceded by short accumulation phases; 3) cycles with low accumulation that occurs in cold season; and 4) cycles with low snow depth which take places during spring. An accumulation curve is also proposed. The calibration and validation of these curves over the study area show the great accuracy found with root mean squared error of 105 mm for snow depth and 0.2 $m^2m^{-2}$for snow cover fraction.*

This chapter has been prepared to be submitted to *Hydrology and Earth System Sciences:*
Pimentel, R., Herrero and M. J., Polo: Subgrid parameterization of snow distribution in a Mediterranean site using terrestrial photography

## 3.1. Introduction

Snow spatial distribution over mountainous areas is *per se* very heterogeneous due to the high variability of both the driving process and topography. These factors are greater constraints in Mediterranean mountain regions, where the changeable climate conditions make the snow`s allocation still more complex. Moreover, snow plays a crucial role in these areas, constituting large part of the total water resources and determining in most cases the infiltration/runoff regime and the water available during dry season.

To represent snow evolution, numerous snowmelt-accumulation models with different calculus methodologies depending on the study area and scale are found in the literature. From the physical-based point models for the mass and energy balance, which explain snow dynamics over a vertical snow column (1D) (Jordan 1991; Tarboton and Luce 1996; Herrero et al., 2009); to distributed models, which take into account the spatial distribution of the snow using a gridded discretization of the study area (Luce and Tarboton 2004). The former are often not applicable to large areas due to the non-consideration of snow spatial distribution, and thus the latter are generally employed in these cases (Arola and Lattenmaier, 1996; Luce et al, 1997). These models need the definition of an optimal grid size according to the physics of the study processes, which must be small enough to explain the subgrid variability and large enough to represent the global snow process (Blöschl, 1999). Cells of sets of ten meters in size are enough to capture the relationship between spatial distribution and micro-topography (Lapena and Martz 1996; Anderton et al. 2004), which is the main factor that conditions snow distribution at this scale, favouring the generation of turbulent fluxes and snow deposition and erosion (Dadic et al, 2010).

However, a direct extension of the calculations of point models into distributed area must not be done when the cell area is not completely covered, since the mass and energy balance must only

be applied over the snow covered area. Thus, a parameterization of a subgrid scale variability is necessary to represent the snow distribution and the processes that occur at this scale. The most extended method for simplifying these effects and representing the snow`s irregular subgrid distribution is the use of depletion curves, which parameterize the snow processes inside the homogeneous areas considered (Luce et al. 1999). Generally, these curves relate a snow state variable, e.g. snow water equivalent or snow depth, to the fraction of snow on one cell, establishing a direct relationship between snow properties and cell coverage. Different examples of parameterization of depletion curves have been proposed (Ferguson 1984; Buttle and McDonnel 1987; Luce at al. 2004), the use of a depletion curve derived from data observed in the study site being the most practical one.

In semiarid environments several snowmelt cycles take place throughout the year, each one shows a different snow behaviour depending on the time of the year and the weather conditions that take place during the accumulation phases. Thus, a single depletion curve cannot be employed. A sigmoid trend appears as being a common characteristic of all these different snowmelt cycles. Three different phases can be distinguished: 1) an asymptotic trend, at the beginning of the melt process when most of the area is still covered; 2) a linear trend, corresponding to the period where several free of snow patches begin to appear; and 3) an accelerating phase trends to zero, where the melt is faster due to the increasing of free of snow patches. This evolution process follows the same trend observed in the growth of an organ, a plant or a crop, thus the parameterizations used to define this process can be extrapolated to snow evolution. Different curves are proposed to explain this evolution, for example: logistic function (Verhulst, 1838; Richards, 1959), Richards function (Grudriaan and van Laar, 1994), Weibull function (Dumur et al, 1990) and Gompertz function (Winsor, 1932). Yin et al. (2003) proposed a new flexible sigmoid function, which includes the benefit of all of this. Their features are: 1) to be flexible in describing various asymmetrical sigmoid patterns, 2) to have numerically stable parameters in statistical estimation, 3) to predict a zero value at the origin of coordinates and 4) to be easily truncated to represent the asymptotic behaviour. Due to the high variability between periods, this flexible function was employed to represent the evolution of the snow.

This gradual decrease also provides an opportunity to monitor the melt progress by observation of the snow covered area, and thus to update the hydrological model with satellite remote sense information (Kolberg et al., 2006; Herrero et al., 2011). These techniques pose some constraints in adjusting their spatial and temporal resolution to the scale of the snow process in these areas. An alternative would be the use of terrestrial photography, which is taken from the Earth's surface and whose temporal and spatial resolution can be adapted to the scale of these processes (Pimentel et al. 2012). These images are georeferenced using a digital elevation model (DEM) and an algorithm based on graphics design principles (e.g. Corripio et al. 2004, Rivera et al. 2008, Farinotti et al 2010 and Pimentel et al 2012).

With the above-mentioned concerns, the objective of this work was to define empirical depletion curves, which are able to explain the subgrid (30 x 30m) variability and the differences observed between several snowmelts throughout the years and in different years, characteristic of Mediterranean site. To achieve this, terrestrial photography at this scale has been employed to monitor the subgrid snow cover fraction evolution.

This chapter is organized as follows: section 3.2 describes the characteristic of the study site and the data available; section 3.3 introduces the different methods employed: point model,

definition of the depletion curve and georeference process. In section 4.4, the new parameterization is shown and validated with another year of measurements; summaries and conclusions are drawn in section 5.

## 3.2. Study site and data available

This study has been carried out in the Sierra Nevada Mountains, Southern Spain (latitude 37ºN), where the highest altitudes in Spain can be found (3482 m.a.s.l.). They form a linear mountain range which runs 60 km parallel to the Mediterranean coast, which is only 40 km away. Thus, an interaction between semiarid Mediterranean and alpine climate conditions takes place in this area. The snow appears at above 2000 m during winter and spring and, even though snowmelt season extends from April to June, the typical mild Mediterranean winters produce several snowmelt cycles before the final melting. Precipitation is distributed heterogeneously over the area due to the steep orography, fluctuating between years (400-1500 mm). Average temperatures can range during the snow season at from -5ºC to 5ºC, although minimum values of -20ºC can be found in certain times in winter.

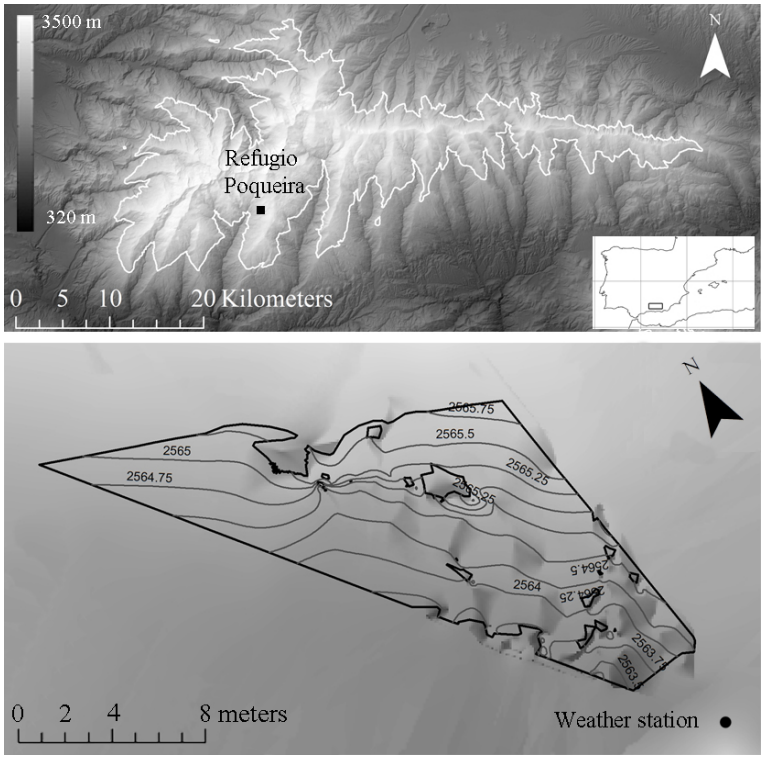


Figure 3.1 Location of the study site at Sierra Nevada Mountains, southern Spain (top), and DEM of the control area located close to the Refugio Poqueira Weather Station (below). The black dot indicate the location of the weather station and the black solid line the area covered by the images obtained from terrestrial photography

A control area of about 900 $m^2$ near the monitoring weather station Refugio Poqueira (Figure 3.1), at 2500 m.a.s.l., sized according to a grid cell area of 30 x 30 m, representative of the variance of global snow processes (Lapen and Martz 1996; Blöshl 1999; Anderson et al. 2004) was selected. This plot is composed of fragmented phyllites and schists, and a characteristic vegetation canopy, consisting of *Genista versicolor* and *Festuca clementei*, two compact and densely branched low shrubs that grow closely together, forming extremely compact, low, continuous cover, which acts as an insulator between the soil and the snowpack, and moreover,

it constitutes the main vegetation cover from 2000 to 2900 m over this area. Therefore, the control area, also represents the micro-relief of the highest areas of Sierra Nevada well.

As mentioned above, a weather station was installed close to the control area. Since 2004 up to the present, 5-minute data have been recorded. This station consisted of a rain gauge with Alter shields to facilitate snow collection, a pyranometer to measure solar radiation, a temperature probe, humidity sensor, wind monitor, and a nanometer. The station has also received an automatic CC640 Campel Scientific since the summer of 2009. Five images per day, every two hours between 8.00 a.m. to 4.00 p.m. of the control area with a resolution of 640 x 504 pixels were stored. This camera is able to capture both the quick snow melting cycles and the spatial heterogeneity exhibited by the snow cover at the study site in relation to the micro-topography. Additionally, two snow measuring rods were installed in the photographed area at representative points where the snow is more persistent during most of the snowmelt cycles throughout the year. Thus, the TP images allowed us to monitor a representative snowpack depth ($h_{ref}$) at the study site with high frequency recordering.

## 3.3. Method

Three consecutive hydrological years, 2009-2012, were analysed at the study site. Snow cover fraction and snow thickness obtained from terrestrial photography during the study period were used to define the new parameterization of snow depletion curves. A flexible sigmoid function proposed by Yin et al. (2003) was employed to fit the data obtained. These curves were incorporated into the snowmelt-accumulation model formulated by Herrero et al. (2009). The model was calibrated from 2009-2012 with the inclusion of the new depletion curves proposed, and the local weather dataset. A fourth year of data (2012-2013) was used to validate these results. This section describes the different items in the calculation process: the obtaining of snow cover fraction and snow depth from terrestrial photography, the definition of depletion curves, its inclusion in the modelling and the calibration and validation processes.

### 3.3.1. Terrestrial photography analysis

To quantify the evolution of snow cover fraction, terrestrial photography obtained at the study site was employed. They were underwent a two-step analysis: georeferencing, to provide the image with spatial coordinates, followed by a snow detection process using a non-supervised clustering algorithm which provided both the SCF and snow depth for each image. Both steps are described below.

#### Georeference

The georeference of each image was made on the basis of the local DEM, whose quality together with the image quality (level of distortion induced by the lens during the acquisition process) determined the final accuracy of the results.

First, the images were lined up to correct possible displacements during the acquisition process. Secondly, the corrected images are georeferenced to a DEM following standard procedures for viewings with computer graphics (Fiume et al. 1989; Foley et al. 1990), which relate the two-dimensional pixels in the images to the three-dimensional points in the DEM. This mapping function transfers the coordinate system of the DEM to the camera position and applies a transformation according to the focal length and view direction. The result is a virtual photograph of the DEM, that is, a representation of it as it would be seen from the point of view of the camera. The two-dimensional representation of the DEM is then scaled according to the

resolution of the photograph (Corripio 2004; Rivera et al. 2008). In this way, the two representations can be superimposed, establishing the necessary correspondence between a pixel in the photograph and its projection coordinates in the DEM. The final result is a map in which all the pixels in the terrestrial photography have been located over the terrain.

### Snow detection

To distinguish the snow-covered and non-covered pixels in each image, a clustering algorithm was applied. These unsupervised methods are generally used to group together data according to some certain notion of similarity. In this case, all the white points in the scene are linked to the presence of snow, so that two clusters can be easily defined: snow-cover and non-covered pixels. A K-mean clustering (MacQueen 1967) was selected; this algorithm classifies the data into a given number of clusters, selecting a random centre within each cluster and minimizing the distance between the data and these centres. This algorithm proved to be efficient enough to differentiate these two kinds of pixels, since it was capable of detecting most of the snow area with no previous calibration or the use of fixed thresholds in the images, with a resulting low level of misclassifications, which were in turn related to the presence of strong shadows in the images (Pimentel et al. 2012). From this pixel classification, the SCF can be easily calculated.

This algorithm was also used to measure the snow depth from the roads built in the control area. The roads were painted in a distinct color, red, which made them easy to differentiate from the remaining objects in the scene. From the clustered results, a linear equation was capable of estimating the depth of the snow from the identified rod pixels identified. This measured depth is considered as representative snow depth of the control area.

## 3.3.2. Snow modelling: Incorporation of depletion curves into point modelling

As mentioned above, the physical point accumulation-snowmelt models are often not applicable to large areas since they do not take into account snow spatial distribution. In spite of this, their calculation can be spatially extended by means of depletion curve approach. This section describes the point model used and the extension to distributed model using depletion curves.

### Snow modelling: Point model

The snowmelt-accumulation model in a Mediterranean site developed by Herrero et al (2009) is a physical model based on a point mass and energy balance. The model assumes a uniform horizontal snow cover surface distributed in one vertical layer. This snow column per unit area defines the control volume, which has the atmosphere as an upper boundary and the ground as a lower one; the lateral mass and energy fluxes between adjacent snows columns are regarded as null. The balance was updated according to:

$$\frac{d\,SWE}{dt} = R - E + W - M \tag{3.1}$$

$$\frac{d(SWE \cdot u)}{dt} = \frac{dU}{dt} = K + L + H + G + R \cdot u_R - E \cdot u_E + W \cdot u_W - M \cdot u_M \tag{3.2}$$

where *SWE* (snow water equivalent) is the water mass in the snow column, and *u* is the internal energy per unit of mass (*U* for total internal energy). In the mass balance, *R* defines the precipitation rate; *E* is water vapor diffusion rate (evaporation/condensation); *W* represents the mass transport rate due to wind; and *M* is the melting water rate. On the other hand, regarding energy fluxes, *K* is the solar or short wave radiation; *L* the thermal or long-wave radiation; *H* the

exchange of sensible heat with the atmosphere rate; *G* the heat exchange with the soil rate; and $u_{R,}$ $u_{E,}$ $u_W$ and $u_M$ are the advective heat rate terms associated with each one of the mass fluxes involved in Eq.(3.1).

Some simplifying assumptions were proposed when applying Eqs. 1 and 2 at the study site. The wind transport term, *W,* was disregarded due to the quick snow metamorphosis, which compacts the snow and reduces its mobility. *G* was also disregarded since, besides being considered a secondary term *per se* in the energy balance (Kuusisto 1986), its value is considerably reduced at this site by the insulating properties of the local vegetation canopy. *P* is direct input from the dataset measured by the weather station. In addition, the terms, *K*, *L*, $E \cdot u_E$ and *H* can be explained as:

$$K = K\downarrow + K\uparrow = K\downarrow (1-\alpha) \tag{3.3}$$

$$L = L\downarrow + L\uparrow = L\downarrow - \sigma_{SB} \cdot T_{sn}^4 \tag{3.4}$$

$$U_E = \left( \frac{K_{U_E}}{\phi_M \cdot \phi_V} \cdot v_a \right) \cdot \left( e_{sn} - e_a \right) \tag{3.5}$$

$$H = \left( \frac{K_H}{\phi_M \cdot \phi_H} \cdot v_a + K_{H0} \right) \cdot \left( T_a - T_{sn} \right) \tag{3.6}$$

where $K\downarrow$ and $K\uparrow$ are downwelling and upwelling short radiation fluxes, $K\downarrow$ is measured directly by the weather station; $\alpha$ is the snow albedo, which in this study is considered to be constant with a value of 0.8; $L\downarrow$ and $L\uparrow$ are downwelling and upwelling long radiation fluxes, where $L\downarrow$ is also measured directly by the weather station; $U_E = E \cdot u_E$; $K_{UE}$ is the bulk latent-heat transfer coefficient, which depends on average roughness of the snow $z_0$; $K_H$ is the bulk sensible-heat transfer coefficient with wind and $K_{H0}$ the same without wind; $v_a$, $e_a$, and $T_a$ are, respectively, the wind speed, the air vapor pressure, and the air temperature at a reference altitude $z_R$ (typically 2 meters); $e_{sn}$ is the saturation vapor pressure for the snow temperature, $T_{sn}$; and $\phi_M$, $\phi_V$ and $\phi_H$ are the stability-correction factors for non-adiabatic temperature gradients for mass, wind and sensible heat, respectively (Dingman, 2002).

### Depletion curves

Depletion curves are functions that are employed to distribute snow point calculation over a fixed area taking into account the spatial variability inside this area. These empirical functions relate the fraction of cell area covered by snow with some other snow state variables. During a snowmelt cycle, the selected depletion curve quantifies the decrease in snow cover within the cell, and thus reducing the area implied in the energy balance. Therefore, it is crucial to make an adequate selection of a suitable DC in the modelling.

Because of the presence of different snowmelt cycles during the snow season and their variability between years, three hydrological years (2009-2010, 2010-2011 and 2011-2012) were employed to define depletion curves. Different methodologies have been employed to define theses curves in scientific literature. For example, Luce and Tarboton (2004) use a probability density function of SWE in the peak accumulation date over a basin; and Kolberg et

al (2006) applied Bayes' theorem to updating these curves using remote sensing data. In most of these cases depletion curves are defined over larger extensions, snow processes being represented at subbasin or watershed scales. Due to the specific characteristics of snow in these areas, a cell of 30 x 30 m was selected. This cell size is much smaller than the area considered by the authors mentioned above so that therefore, terrestrial photography, with adaptable resolution, was used to define it. The variables related by DC were snow cover fraction and snow depth.

To minimize the variability observed between years, depletion curves were defined using dimensional variables. The snow variables represented were $h^*= \bar{h}/\bar{h}_{max}$ (x-axis) and $SCF^*= SCF/SCF_{max}$ (y-axis), dimensioned using the maximum mean snow depth ($\bar{h}_{max}$) and maximum fraction covered by snow ($SCF_{max}$) respectively for each cycle.

Each curve was fitted to the flexible sigmoid function proposed by Yin et al. (2003) adapted to the snow melting:

$$\begin{aligned} SCF_i^* &= SCF_{i_{\max}}^* \left(1+\frac{h_{i_e}^*-h_i^*}{h_{i_e}^*-h_{i_m}^*}\right)\left(\frac{h_i^*}{h_{i_e}^*}\right)^{\frac{h_{i_e}^*}{h_{i_e}^*-h_{i_m}^*}} \qquad if \quad 0 \le h_i^* < h_{i_e}^* \\ SCF_i^* &= SCF_{i_{\max}}^* \qquad if \quad h_i^* \ge h_{i_e}^* \end{aligned} \tag{3.7}$$

In this case the parameters correspond to $SCF_i^*$ and $h_i^*$, dimensioned snow cover fraction and snow depth for the each one of the melting cycles ($i$). Three adjustment parameters were employed $SCF_{i_{max}}^*$, maximum value of $SCF^*$, $h_{i_e}^*$ dimensionless depth when the melt began and $h_{i_m}^*$, dimensionless depth when maximum melt rate was achieved. Gradient descent algorithm was employed to obtain the optimal values of the coefficients proposed in the parametric descriptions.

The defined parameterizations were incorporated into the model. At each iteration, *SCF* was obtained by means of the simulated snow depth using the curve selected. This *SCF* works as a reduction factor of the different energy fluxes in the following time step.

In the same way, during accumulation phases the snow cover of snow is not completely homogeneous. Therefore a parameterization for these cycles is also proposed. The methodology employed to define this "accumulation curve" is the same one used in the case of depletion curves

### 3.3.3. Calibration and validation

After depletion curve inclusion, the new distributed model must be calibrated with this new configuration. Three years of data were employed (2009-2012), where the presence of very different meteorological conditions was found: wet year (2009-2010), very wet year (2010-2011) and a dry year (2011-2012). In this way a wide field of possible meteorological situations have been analysed.

The calibration hypotheses were focused in those parameters that possess the greatest uncertainty, since they are not directly measured. All of them are closely related to the turbulent fluxes at energy balance. In this way, the hypotheses suggested were: 1) the influence of the

stability-correction factor for turbulent transfer ($\phi_M$, $\phi_V$ and $\phi_H$); 2) the importance of the sensible-heat transfer coefficient in windless conditions ($K_{H0}$); and 3) the value of the roughness of the snow ($z_0$). Some authors (Anderson, 1976; Jordan, 1991; Flerchinger et al. 1994) warn that the thickness of the active snow layer must also be considered. Nevertheless, the use of a one-layer model in this study excludes the employment of this calibration parameter.

To evaluate the influence of $\phi$ factors the hypothesis testing were the employment of the formulation proposed by Cline (1997) in contrast with not including these coefficients (Tarboton and Luce, 1996). To study the influence of $K_{H0}$, a comparison between the values obtained in a previous calibration for the point model (Herrero et al, 2009) against the values proposed by Jordan (1991) was tested. And finally to evaluate $z_0$, values commonly used in the literature range from 0.0001 to 0.01m (Jordan, 1991; Marks and Dozier, 1992; Tarboton and Luce, 1996; Marks et al., 2008; Andreadis et al., 2009) was analysed.

Data collected during hydrological year 2012-2013 was performed to validate the results. This validation is done based on the snow variables measured on terrestrial photography for this validation period.

## 3.4. Results

This section shows the results of the different steps described in section 3.

### 3.4.1. Terrestrial photography measurements

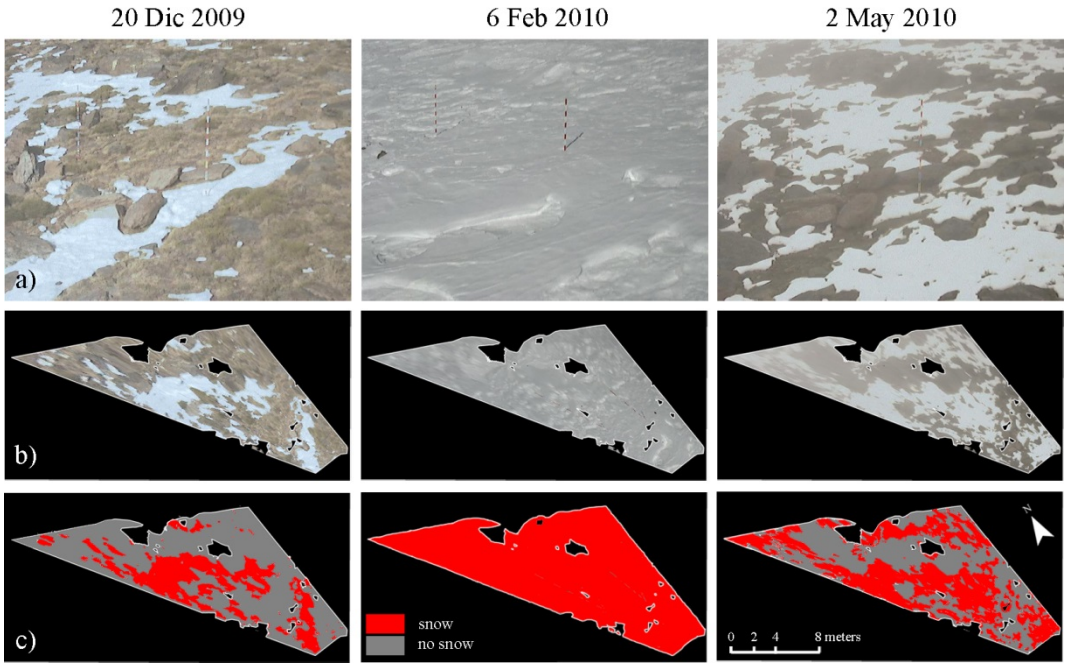


Figure 3.2 Example of the terrestrial photography georeference process at the study site for selected days during the snow season, beginning, consolidates and final a) Original image; b) Georeference image; c) Snow mask obtained from the georeferenced image by using K-mean algorithm

About 2000 images were georeferenced by a 0.05 x 0.05 m DEM obtained thanks to a topographic survey in this area, which was done by a total station Leica TCR 403. The results of this process were snow cover maps in the photographed areas during the study period, with the same spatial resolution of the DEM (0.05 x 0.05 m) and with a temporal resolution according to the frequency of the photographs acquisition process (5 images per day) (Figure 3.2).

In the same way, a continuous record of $h_{ref}$ is measured in the rod with the same temporal frequency of the acquired images. This measurement was transformed into mean snow depth values ($\overline{h}$) by means of a function obtained using the geometry of the DEM in the control area and assuming a spatially uniform melting:

$$\overline{h}=\begin{cases} -0.2764\cdot h_{ref}^{\ 3}+0.8066\cdot h_{ref}^{\ 2}+0.2608\cdot h_{ref} & if \quad h_{ref}\le 0.6 \\ h_{ref}-0.2129 & if \quad h_{ref}>0.6 \end{cases} \tag{3.8}$$

where 0.6 m corresponds to the percentile 98$^{th}$ in the distribution of heights in the control area, which marks the beginning of a completely covered surface.

Figure 3.3 shows a representation of both *SCF* and $\overline{h}$. It shows the high variability observed between the different snowmelt periods and year, and thus it corroborates the need to define different snow depletion curves depending on the analysed period.

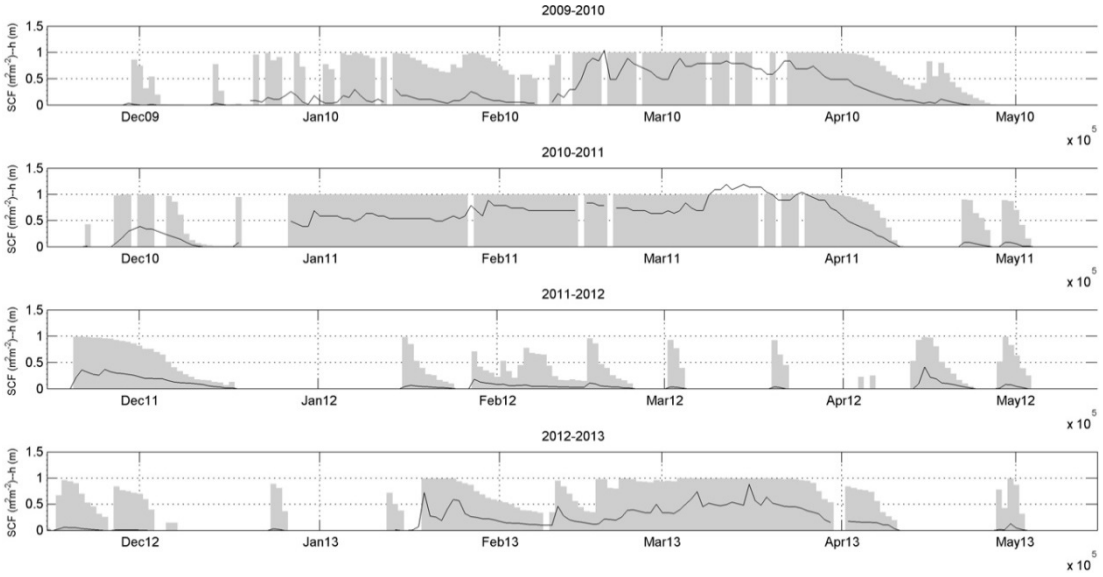


Figure 3.3 Representation of both variables, SCF (gray bars) and snow depth (black line), obtained from terrestrial photography

### 3.4.2. Depletion curves

To define the depletion curve, *h** (x-axis) versus *SCF** (y-axis) for each snowmelt cycle is represented. Among all the observed snowmelt periods, only a few of them were selected for the analysis. The snowmelt cycles disregarded were those that: 1) do not intersect the ordinate axis in zero, since they are not complete melt periods; 2) do not have a great number of measurements, since in these cases multiple fits could be found; and 3) are always covered. With the selected snow periods the sigmoid function proposed by Ying et al. (2003) was fitted. The fit parameters, $h_e^*$ and $h_m^*$, for each of the selected curves are shown in Table 3.1; due to the dimensionless of the variables the third parameter, $SCF_{max}^*$ is always equal to one, correlation coefficients also for each adjust also appear.

Table 3.1 Values of the fit parameters ( $h_e^*$ and $h_m^*$ ) and correlation coefficient ( $R^2$ ) for the depletion curves defined for the analysed snowmelt cycles. Last column shows a classification of the proposed depletion curves based on the fit parameters

| Year | Cycle | $h_e^*$ | $h_m^*$ | $R^2$ | Type |
|---|---|---|---|---|---|
| 2009-2010 | 9 | 0.80 | 0.14 | 0.85 | Curve 1 |
| 2009-2010 | 11 | 0.75 | 0.15 | 0.90 | Curve 1 |
| 2009-2010 | 13 | 0.85 | 0.10 | 0.88 | Curve 1 |
| 2009-2010 | 22 | 0.78 | 0.13 | 0.94 | Curve 1 |
| 2010-2011 | 2 | 0.80 | 0.40 | 0.97 | Curve 2 |
| 2010-2011 | 15 | 0.76 | 0.16 | 0.97 | Curve 1 |
| 2010-2011 | 16 | 1.10 | 0.05 | 0.97 | Curve 4 |
| 2010-2011 | 17 | 1.15 | 0.13 | 0.90 | Curve 4 |
| 2011-2012 | 2 | 0.91 | 0.56 | 0.97 | Curve 2 |
| 2011-2012 | 4 | 0.99 | 0.77 | 0.93 | Curve 3 |
| 2011-2012 | 5 | 1.00 | 0.76 | 0.97 | Curve 3 |
| 2011-2012 | 6 | 1.00 | 0.65 | 0.97 | Curve 3 |
| 2011-2012 | 7 | 1.05 | 0.80 | 0.89 | Curve 3 |
| 2011-2012 | 8 | 1.00 | 0.65 | 0.96 | Curve 3 |
| 2011-2012 | 9 | 1.01 | 0.45 | 0.95 | Curve 4 |
| 2011-2012 | 11 | 0.85 | 0.38 | 0.97 | Curve 2 |

According to the values of the fit parameters obtained, the different snowmelt cycles could be classified into four groups (last column of the Table 3.1). Grouping the measured data following this classification and fitting them to the sigmoid function proposed, four depletion curves were defined (Figure 3.4).

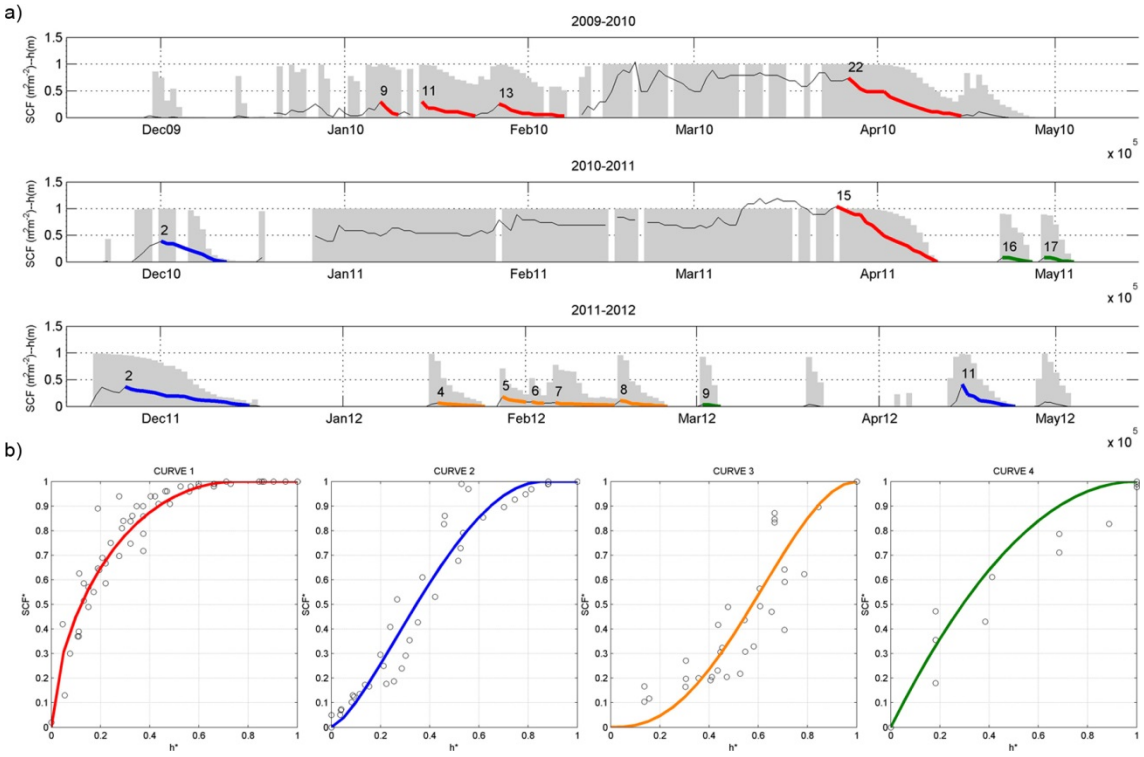


Figure 3.4 a) Selection of the different snowmelt period throughout the year, b) Depletion curves proposed: Curve 1, cycles with high accumulated snow depth which comes from a long accumulation stage; Curve 2, cycles with high accumulated snow depth preceded by a short accumulation phase; Curve 3, cycles with low accumulated snow at the beginning of the snow season; and Curve 4, cycles with low snow accumulated at the end of the snow season.

Table 3.2 Values of the fit parameters ( $h_e^*$ and $h_m^*$ ) and correlation coefficient ($R^2$) for the four depletion curves proposed.

| **Curve** | $h_e^*$ | $h_m^*$ | $R^2$ | **RMSE** |
|---|---|---|---|---|
| Curve 1 | 0.759 | 0.000 | 0.91 | 0.072 |
| Curve 2 | 0.861 | 0.264 | 0.94 | 0.088 |
| Curve 3 | 1.000 | 0.617 | 0.85 | 0.123 |
| Curve 4 | 1.000 | 0.157 | 0.98 | 0.080 |

The values of the fit (Table 3.2) parameters condition the shape of the proposed curve just like the physic of the processes represented by them. On one hand, Curve 1 exemplifies cycles with a high accumulated snow depth which comes from a long accumulation stage being a highly metamorphosed and compacted snow. On the other hand, Curve 2 also represents cycles with great snow depth, although in this case they are preceded by a short accumulation phase. The snowmelt cycle occurs directly after the accumulation stage and is therefore slightly compacted snow. Curve 3 and Curve 4 represent snowmelt cycles where the snow thickness achieved is considerably lesser than in previous cases. Therefore, in these cases the micro topography conditions the melt from the beginning of the cycle. The main difference between both is the season when they take place. The dynamics of these cycles during autumn or winter is different from throughout spring. In the former, the snowmelt rate possesses a fast initial melting followed by a slowdown in its final stage and in the latter the snow decay is faster and approximately constant throughout the melt cycle.

This differentiation between them is also revealed in the value of the fit parameters. $h_e^*$, which mark the beginning of the melt, is lower in Curve 1 than in Curve 2 (0.823 vs 0.905). This is evidence of the effect of the snow consolidation, which delays the beginning of the melt. This parameter is equal to one in Curve 3 and Curve 4, which shows that in these curves the beginning of the cycle immediately occurs after the accumulation. The same thing takes place with $h_m^*$, which determines when the maximum melt rate is reached, in these cases Curve 1 and Curve 4 ( $h_m^*=0$ ) possess a constant rate throughout the cycles, while in the cycles represented by Curve 2 ( $h_m^*=0.488$ ) and Curve 3 ( $h_m^*=0.727$ ) two different rates appears: fast initial (faster in Curve 3) and slow final melting (faster in Curve 2).

To incorporate these new depletion curves into the snowmelt-accumulation model developed by Herrero et al. 2009, and following the above-mentioned concerns, a decision tree to select the optimal curve for each snowmelt cycle is defined. Figure 5 shows this decision tree. The decision questions are related to: 1) the amount of days with previous snow, one month is an optimal period to discriminate the effects of the compaction of the snow; 2) the maximum thickness of the snow achieved in this cycle, the distinguishing value selected being 0.60 m according to the representative value of the topography selected above; and finally 3) the season of the year, discriminate between autumn or winter and spring snow.

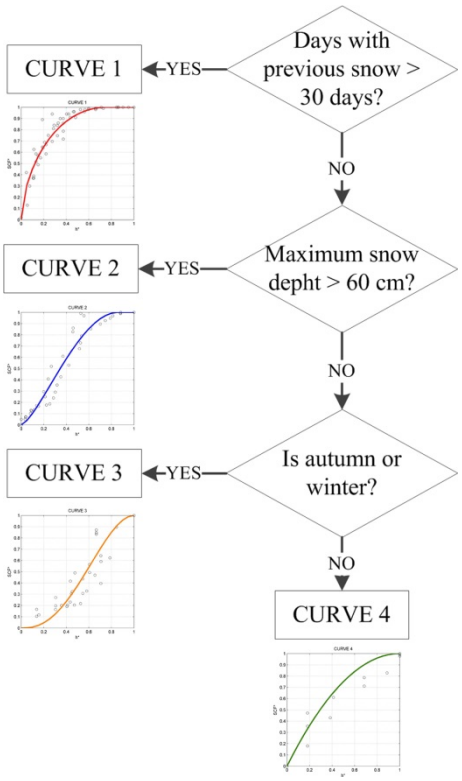


Figure 3.5 Decision tree to select between the different depletion curves proposed

## Accumulation curves

As mentioned above, during its accumulation stage the snow is also distributed heterogeneously over the cell. The processes involved are different from melting cycles and thus, a different curve to explain this distribution is also needed. In this case, the variability between cycles is lower than during the melting stage and thus all the periods are analysed together. As was done in depletion curve definition those cycles with less than a minimum number of data were disregarded. The variables compared are the same (*h* and *SCF*) and in this case they are also dimensionless. Figure 6 shows the proposed fit in this case and also represents the hypothetical accumulation curve defined by the micro relief assuming a spatially uniform accumulation.

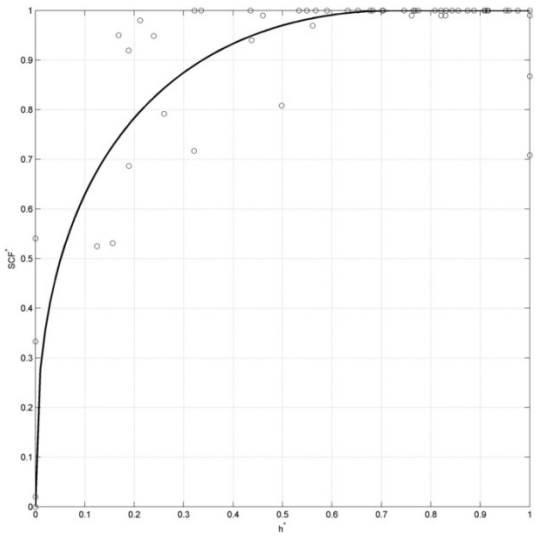


Figure 3.6 Accumulation curve proposed (blue dot); measured data (black cross) and hypothetical curve obtain by means of the assumption of spatially uniform accumulation over the micro-topography

Table 3.3 Values of the fit parameters ( $h_e^*$ and $h_m^*$ ) and objective function ($R^2$ and RMSE) for accumulation curve proposed.

| **Curve** | $h_e^*$ | $h_m^*$ | $R^2$ | **RMSE** |
|---|---|---|---|---|
| Accumulation | 0.707 | 0.000 | 0.85 | 0.143 |

### 3.4.3. Calibration and Validation

As mentioned in section 3.3.3, data from 2009-2012 were used to calibrate the model once the curves were incorporated. The hypothesis employed for that was: a) the influence of $\phi_M$, $\phi_V$ and $\phi_H$ ; b) the importance of $K_{H0}$ ; and c) the most suitable mean value of $z_0$ . Mean error (ME), the absolute error (MAE), the root mean square error (RMSE) and the correlation coefficient ($R^2$), were used as objective functions to determine the goodness in the calibration process. Table 3.4 and Table 3.5 show the different simulations made for both variables with the different calibration hypotheses employed and the comparative statistics for each of the analysed variables.

Table 3.4 Calibration values employed for the different simulation realized and values of the different objective function employed for snow depth.

| **Simulation** | $\phi_M$ , $\phi_V$ , $\phi_H$ | $K_{H0}$ **(W m$^{-2}$ K$^{-1}$)** | $z_0$ **(mm)** | **ME (mm)** | **MAE(mm)** | **RMSE(mm)** | $R^2$ |
|---|---|---|---|---|---|---|---|
| 1 | None | 6 | 25 | 85.111 | 93.235 | 214.855 | 0.732 |
| 2 | Cline | 6 | 25 | 65.029 | 74.668 | 171.210 | 0.856 |
| 3 | Cline | 1 | 25 | 43.122 | 57.175 | 126.683 | 0.920 |
| 4 | Cline | 1 | 5 | -19.385 | 50.392 | 98.123 | 0.945 |
| 5 | Cline | 1 | 1 | -76.972 | 88.336 | 156.752 | 0.948 |
| 6 | None | 1 | 1 | -28.322 | 50.243 | 98.564 | 0.956 |
| 7 | None | 1 | 2.5 | -0.745 | 39.608 | 84.219 | 0.949 |
| 8 | None | 2 | 2.5 | 5.038 | 39.261 | 85.663 | 0.947 |

Table 3.5 Calibration values employed for the different simulation realized and values of the different objective function employed for SCF.

| **Simulation** | $\phi_M$ , $\phi_V$ , $\phi_H$ | $K_{H0}$ **(W m$^{-2}$ K$^{-1}$)** | $z_0$ **(mm)** | **ME (m$^2$ m$^{-2}$)** | **MAE(m$^2$ m$^{-2}$)** | **RMSE(m$^2$ m$^{-2}$)** | $R^2$ |
|---|---|---|---|---|---|---|---|
| 1 | None | 6 | 25 | 0.069 | 0.109 | 0.243 | 0.828 |
| 2 | Cline | 6 | 25 | 0.028 | 0.091 | 0.207 | 0.872 |
| 3 | Cline | 1 | 25 | 0.002 | 0.093 | 0.205 | 0.875 |
| 4 | Cline | 1 | 5 | -0.070 | 0.102 | 0.221 | 0.875 |
| 5 | Cline | 1 | 1 | -0.118 | 0.135 | 0.259 | 0.849 |
| 6 | None | 1 | 1 | -0.066 | 0.091 | 0.201 | 0.897 |
| 7 | None | 1 | 2.5 | -0.040 | 0.079 | 0.180 | 0.911 |
| 8 | None | 2 | 2.5 | -0.033 | 0.077 | 0.177 | 0.912 |

The different simulations show the evident sensitivity to the different parameters on the modelling. In this sense and in general terms, the non-use of $\phi$ factors, a high value of $K_{H0}$ and also high $z_0$ accelerate the melt stage (as can be seen in the positive values of ME in Simulations 1, 2 and 3). Further, this sensitivity in the results is greater for h than for SCF where a high reduction is achieved (e.g. the reduction of RMSE from 214.855mm to 126.683 mm between Simulations 1 and 3). Nevertheless, a very small value for these parameters also delays the extinction of the snow, producing greater mismatching between measured and simulated values (e.g. Simulation 5). Therefore, finally, the optimal calibration values selected were (Simulation 7): a) the no use of $\phi$ factors, as proposed by others (e.g. Tarboton and Luce); b)

$K_{H0}$=1 W m$^{-2}$ K$^{-1}$, a more realistic value for the parameter (Jordan, 1991 and Jordan et al, 1999) than that proposed before; and c) $z_0 = 2.5\,\text{mm}$, reasonable values inside the range 0.0001-0.01m proposed by Jordan, 1991; Marks and Dozier, 1992; Tarboton and Luce, 1996; Marks et al., 2008; Andreadis et al., 2009.

Figure 3.8 and Figure 3.7 show snow depth and SCF measured and simulated with the optimal calibration parameters for the three years period. In the case of SCF simulation (Figure 3.7) the accuracy found is also higher, with a ME= 0.04 mm, MAE=0.079 mm and RMSE= 0.180 mm. All the different snowmelt cycles are represented. As a general trend, simulated values overestimate the measured dataset during short snowmelt cycles, i.e. at the beginning of the first year or during the winter of the third year. On the contrary, the period with persistence of snow usually underestimates the SCF. The snow depth simulation (Figure 3.8) reproduces with a high approximation the snow behaviour throughout the study period, with a RMSE=84.2 mm. This accuracy is lesser for the first year, where, in two months, early January and March of 2010, both simulations have different values. In spite of these mismatches the trends found in both of them follow the same patterns. The other two years are correctly represented, and are able to reproduce the different snowmelt cycles throughout the year, both the intense cycles at the beginning and at the end of the annual snow season and in a long period with persistence of snow.

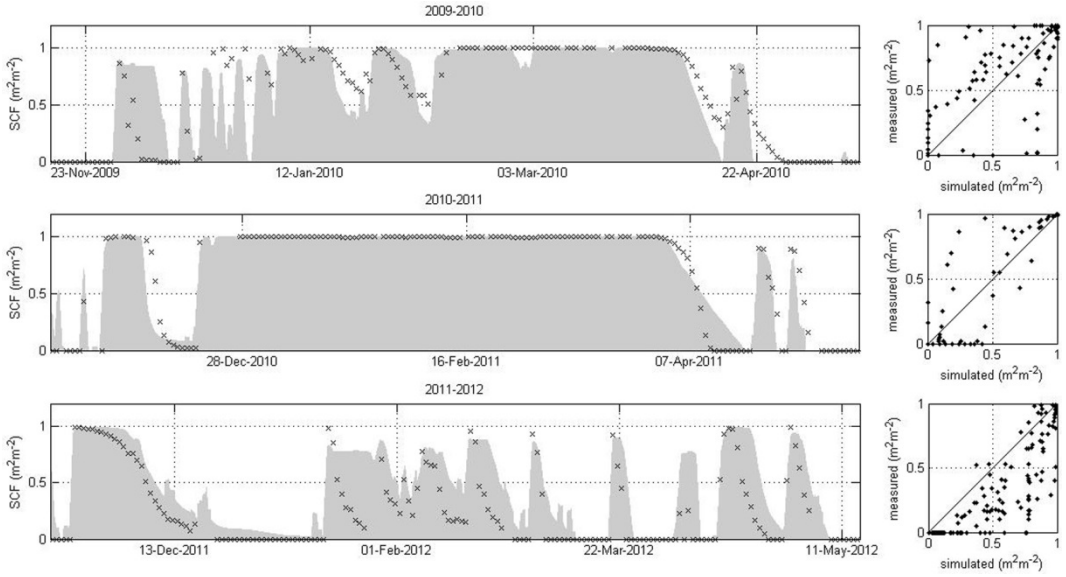


Figure 3.7 Representation of SCF, measured and simulated, for the selected calibration simulation, Simulation 7; and throughout the calibration period (left) and dispersion graphs for each year (right).

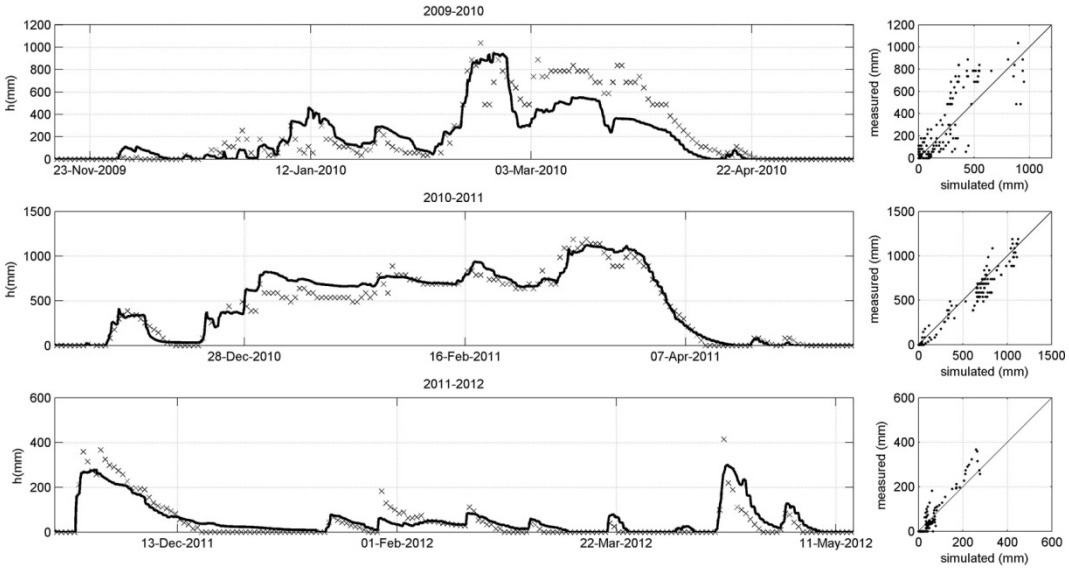


Figure 3.8 Representation of snow depth, measured and simulated, for the selected calibration simulation, Simulation 7; and throughout the calibration period (left) and dispersion graphs for each year (right).

A fourth year of data (2012-2013) is employed to validate previous calibration. Figure 3.9 and Table 3.6 show the results and the statistics of this simulation for both variables, respectively. The results of the calibrated model for this validation year reproduced, with very similar statistics to those achieved for calibration, both variables (Table 3.6). Similar behaviour to that found during calibration period is plotted: a general overestimation of SCF during short cycles and a separation of snow depth on certain dates.

Table 3.6 Values of the different objective function employed for both, snow depth and SCF throughout the validation period.

| Variable | ME | MAE | RMSE | $R^2$ |
|---|---|---|---|---|
| h (mm) | -5.110 | 66.841 | 105.801 | 0.839 |
| SCF ($m^2 m^{-2}$) | -0.112 | 0.134 | 0.219 | 0.8923 |

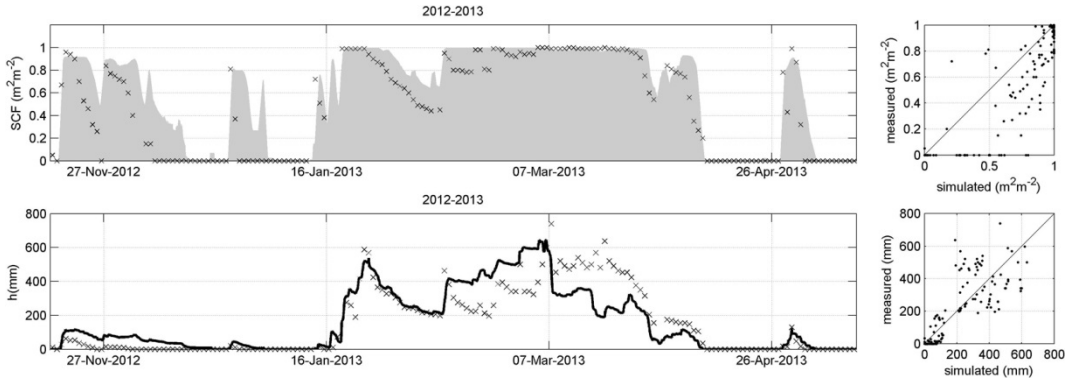


Figure 3.9 Representations of both variables, SCF and snow depth, measured and simulated, throughout the validation period (left) and dispersion graph (right)

## 3.5. Discussion

The four depletion curves proposed are able to explain four different behaviours observed between snowmelt cycles: a) cycles with a large amount of consolidated snow; b) cycles with a large amount of recent snow; c) cycles with little snow during autumn or winter; and d) cycles with little snow during spring. Furthermore, they are able to parameterize the different snow

distribution observed inside the same types of curves. Figure 3.10 represents three images of three different cycles represented by the same curve (Curve 2) at three moments throughout them (90%, 50% and 20% of snow coverage in the cell). Different snow distribution can be observed between images with the same SCF. These differences are marked by the forced atmospheric conditions that reigned during the accumulation phase and the beginning of the melt stage and their relation with the micro topography (e.g. in the images belonging to year 2011-2012 Cycles 13, can observe the effect that the wind produced in the distribution of snow, small accumulation areas appear close to the biggest rocks). However, all these different distributions can be correctly represented with the same curve. Hence, the parameterization is able to capture the subgrid variability in the cell without any need to physically model the process at this scale, for example the interaction between wind and micro topography. Similar effects on snow distribution are observed in the other curves proposed.

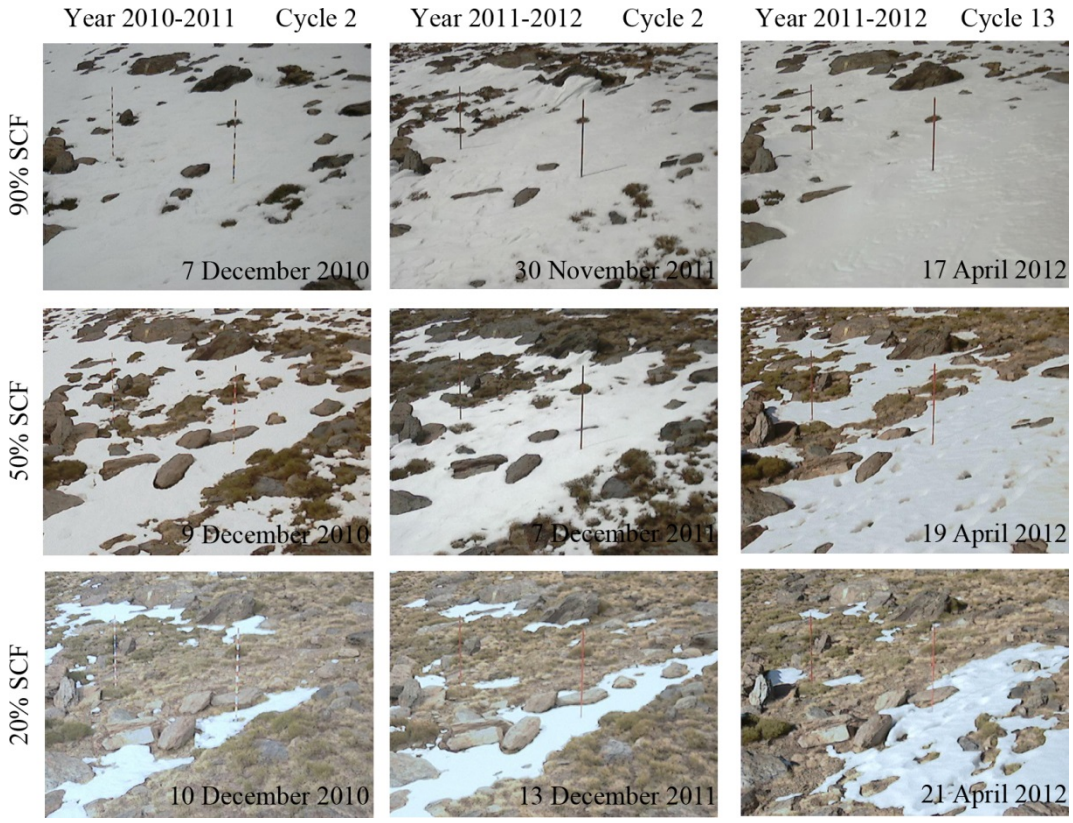


Figure 3.10 Examples of different stages throughout three different snowmelt represented by the same depletion curve, Curve 2.

In spite of the great accuracy shown by the results, in particular events throughout the analysed years, some mismatches take place. Figure 3.11 shows the location of the different mismatches observed in the four years of simulations. It can be grouped in three: 1) Incorrect determination of the fraction of precipitation taking place as rain or snow (blue circles). The model considers precipitation as snowfall whenever the wet-bulb temperature is under 0ºC. In general, the snowfall events are correctly represented. However in certain events this threshold overestimates snow precipitation. This happened during some snowfall at the beginning of the winter (Cases 1 and 5 in Figure 10)), and underestimates it normally in the snow event of spring (Cases 4, 7, 8 and 11 in Figure 10). 2) Impossibility to capture the effects of the blowing snow associated with high gust of wind (green circles). The model does not incorporate the transport action caused by the wind (section 3.2) and although the depletion curves proposed are able to capture different wind effect at cell scale, it cannot reproduce the deposit of snow which comes

from adjacent cells. 3) Bad representation of the effect of the rain over the snow cover (red circles).

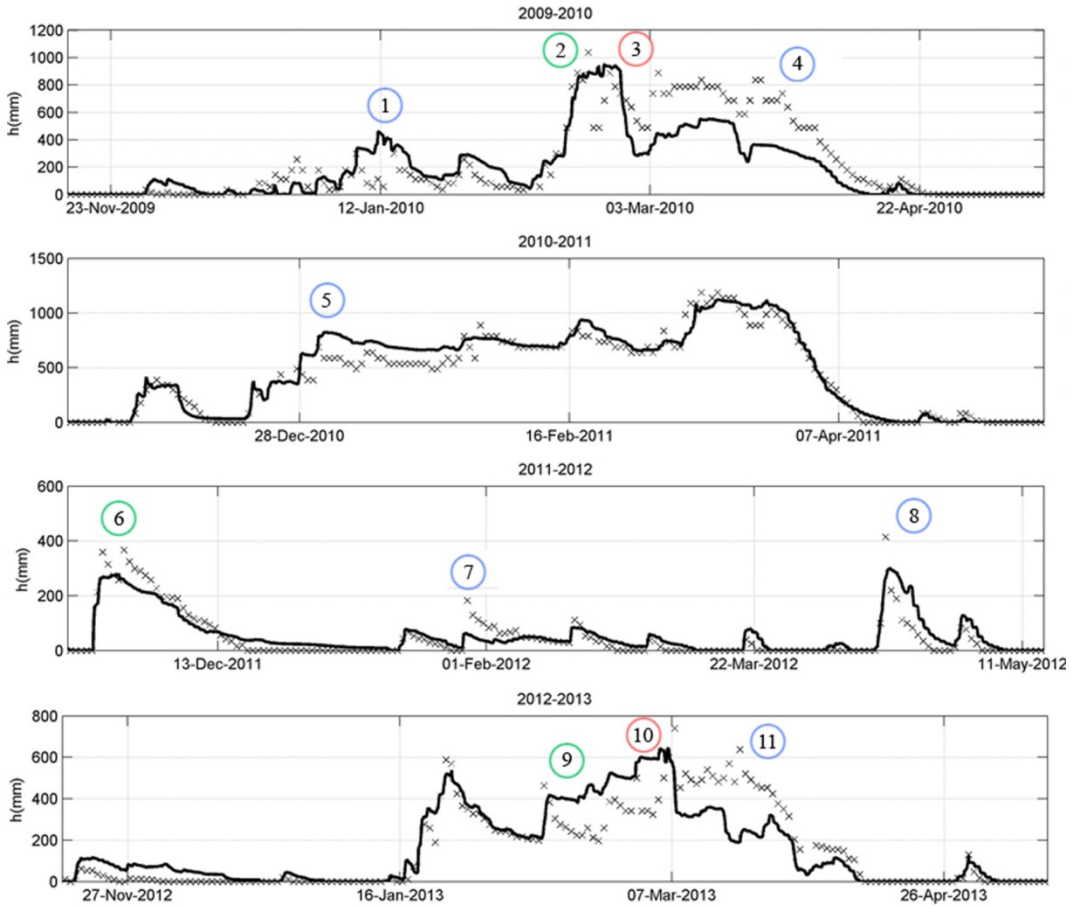


Figure 3.11 Identification of the small mismatches between simulated and measured snow depth throughout the study period and group of that in three different categories: blue circles, incorrect discrimination between rain and snow; red circles, extreme wind event; and green circles, rain over snow

Independently of this, the depletion curves proposed improved the result of the simulations decreasing the associated error by more than those obtained in previous works, where the measured data were incorporated by means of Ensemble Transform Kalman Filter data assimilation (Pimentel et al, 2014).

## 3.6. Conclusions

The use of terrestrial photography allows a continuous monitoring of the snow distribution adapted to spatial and temporal resolution of the physics processes. In this case, it has permitted its measurement, in an economical way, and the evolution of SCF and h over a small control area to study the subgrid variability of the snow at this cell scale (30 m x 30 m), which conventional remote sensors are not able to capture.

Further, thanks to the monitoring of the accumulation and melting stages at this scale and in Mediterranean environments, it has been possible to define different depletion and accumulation curves adapted to the variability of these areas. These curves capture the variability that different agents at this scale, mainly the interaction between wind and microtopography, have on the distribution of snow. The results shown in previous sections demonstrate the importance of selecting one or other depletion curve to represent accurately the snow`s behaviour due to the

different dynamics observed between cycles. Finally, one curve has been proposed for the accumulation stage and four for the melting cycles, which describe the different observed melting dynamics. A decision tree with the variables that condition the melting cycles: days with previous snow, amount of snow accumulated and time of the year, is implemented.

The final optimal calibration exhibits specially well-simulated snow depth values with an error of under 85 mm. The SCF simulation also presents good results, with an error of below 0.18 $m^2$ $m^{-2}$. In both cases, the errors are lower than the associated error obtained in previous works using data assimilation techniques (Pimentel et al. 2014). Therefore, this approach produces similar effects to the assimilation techniques, but in this case based on physics principles.

Despite the improvement produced, assimilation is not always capable of sufficiently mitigating the mismatch occurring which are also identified as incorrect determination of the fraction of precipitation taking place as rain or snow, snow transport events due to strong gusts of wind and rain that is produced over snow.

# CHAPTER 4: Snow evolution in a semiarid mountainous area combining physical hydrological modelling and a spectral mixture analysis of Landsat imagery

*This chapter proposed the use of two approaches, physically distributed hydrological modelling in combination with satellite remote sensing images, to study the evolution of the snowpack in Sierra Nevada Mountain, in southern Spain. The snowmelt-accumulation module from WiMMed (Watershed Integrated Management in Mediterranean Environment) hydrological model was employed, which includes the use of depletion curves to expand the energy and water balance equations over a grid representation of the territory. Two methodologies for obtaining snow cover area maps from Landsat images (16-day images with 30 x 30 m spatial resolution) were tested. Finally, those maps obtained from a spectral mixture analysis were used to evaluate this model at the study site. The results show a significant agreement between observed and simulated snow pixels in the area, which allow one to produce sequences of snow cover maps with a greater resolution than the remote sensing images employed, under variable meteorological conditions. However, some mismatches do appear at the boundaries of the snow area, mainly related to: a) the great number of mixed pixels, not completely covered by snow; and b) the influence of the snow transport by wind, which can be relevant during some events and is not included in the model.*

Part of the results of this chapter has been presented as oral communication in:

- The 3rd Remote Sensing and Hydrology Symposium (RSHS'14) and The 3rd International Conference of GIS/RS in Hydrology, Water Resources and Environment (ICGRHWE'14), which will be published in the "Red Books", *Proceedings of the International Association of Hydrological Sciences*,(*PIAHS):*

Pimentel, R., Herrero and M. J., Polo: Snow evolution in a semiarid mountainous area combining snow modelling and Landsat spectral mixture analysis.

- SPIE Remote Sensing, 2012:

Pimentel, R., Herrero, J. and M. J. Polo, 2012: Terrestrial photography as an alternative to satellite images to study snow cover evolution at hillslope scale. Proceeding, *Remote Sensing for Agriculture, Ecosystems, and Hydrology XIV*, Edimburgh, SPIE. Remote Sensing, 8531.

## 4.1. Introduction

Snowpack makes up natural water storage during the accumulation season and contributes to river runoff or groundwater during melting stages. Therefore, water from the melting of the snowpack constitutes a basic resource for human consumption, agriculture irrigation or hydroelectric production in mountainous areas, whose importance increases in semiarid environments due to the recurrence of drought periods. Moreover the particular weather features of these regions make snow dynamics behave in a particular manner, with transient states from complete snow cover in most of the areas to the absence of snow that may undergo sudden changes and successive accumulation-melting cycles. Thus, snow dynamics is conditioned on one hand by snow accumulation, redistribution and ablation, and the associated meteorological driving processes, and on the other hand by the influence of rough topography, with strong gradients of exposure, vegetation and shadowing. This particular dynamics triggers increases in *per se* heterogeneous snow distribution, and, consequently, makes it difficult to measure and monitor its evolution.

The traditional approaches that study snowpack evolution using simple empirical relationships between snowmelt flux and selected meteorological variables (Kustas et al., 1994), or those based on the study of past snowmelt period (Beniston, 1997), cannot be applied under these changeable conditions. Physical approaches based on mass and energy balances, which make

their calculation distributedly, are usually needed to capture this outstanding heterogeneity over these areas. Furthermore, spatially distributed hydrological modelling has become one of the most commonplace techniques to study snow evolution. Besides, by reproducing the physical processes involved in snow dynamics (Garen and Marks, 2005), these kinds of models can produce a spatial distribution of snow at the significant scales of the reproduced processes, i.e. in a small catchment at high spatial resolution, or on the contrary, a large catchment at a very small resolution (Bavera et al., 2014). A great effort has been dedicated to developing physical snow models, with different examples in the literature (Blöschl et al., 1991; Jordan, 1991; Marks et al., 1999). However, the examples in semiarid regions are scarcer, where special considerations have to be included in their modelling. In this sense, Herrero et al. (2009) developed a point snowmelt-accumulation model in Sierra Nevada (southern Spain). Their results showed the important role of the evaporation fluxes and the significance of the longwave radiation flux emitted from the snowpack in these environments (Herrero and Polo, 2012). However, the extension of physical models to large areas in those regions requires scaling from point to cell calculations; this is usually made through the use of depletion curves, which also capture subgrid variability (Luce et al., 1999; Pimentel et al., 2014). Moreover, these models need distributed datasets of the model state variables to calibrate and validate their GIS-based calculation (Schmugge et al., 2002; Franz and Karsten, 2013). One of the most vital snow properties for snow modelling is snow spatial extent (Blösch, 1991; Dozier & Painter, 2004), which can be obtained by means of remote sensing techniques in a relatively feasible way (Parajka and Blösch, 2008).

Among the large amount of remote sensing information (e.g. NOAA, daily images with 1 x 1km cell size; MODIS, daily images with 250 x 250m cell size; Landsat Thematic Mapper, 16-day images with 30 x 30m cell size) the selection of either dataset is closely related to the scale of the study processes. Spatial resolution is the limiting factor for the snow in a semiarid region, since the extremely changeable conditions favour a specific snow distribution, which usually appears as being medium to small sized patches (Sade et al. 2014). Hence, those datasets with a higher spatial resolution, such as Landsat Thematic Mapper data, are recommended in these studies (Marks and Winstral, 2001; Pimentel et al., 2012), since, for example, MODIS snow products with a 500m x 500m spatial resolution, are not able to capture the significant subgrid distribution present in reality. Another alternative for the study of the snow extension over these changeable areas is the use of terrestrial photography (TP), which is taken from the Earth's surface and whose spatial and temporal resolution can be adapted to the study problem. However its use over large and very rough mountainous areas is limited since, on one hand, a large number of images is required, and, on the other hand, there is a lack of information associated with the non-visible areas that may be significant in some cases.

This work analyses the spatial distribution regime of the snow in the watershed of the Guadalfeo river basin, at the Sierra Nevada mountains (Spain), by means of the application of the point snowmelt-accumulation model developed by Herrero el al. (2009), extended at the cell scale in Pimentel et al. (2014), in combination with a 10-yr series of snow cover maps (30 x 30m) obtained from Landsat imagery. Two methodologies were tested: 1) the use of difference indexes to obtain binary maps (covered and non-covered pixels); and 2) a spectral mixture analysis model to calculate fractional snow cover maps (percentage of coverage inside each pixel). The performance of both methodologies is assessed by means of snow cover maps (10 x 10m) obtained thanks to TP in a small monitored area located in the same watershed.

The chapter is organized as follow: section 4.2 describes the characteristics of the study site and the available dataset; section 4.3 introduces the methods: the snowmelt accumulation model and the extraction of snow maps; section 4.4 presents the results and their discussion; and, finally, the conclusions are drawn in section 4.5.

## 4.2. Study site and available data

The study site is located at Sierra Nevada Mountains, southern Spain. They are a linear mountain range parallel to the coastline of the Mediterranean Sea, with altitudes ranging from 1500 to 3500 m.a.s.l. The typical mountain alpine climate is modified by its proximity to the sea, which generates semi-arid and tropical conditions in the surrounding area, mainly in the southern hillside closer to the sea. This results in the presence of a consolidated snow cover only from December to June and over altitudes higher than approximately 2000 m.a.s.l. All these characteristics generate an enhanced altitudinal gradient, which, together with the different existing land uses and a diverse presence of vegetation and soil types, produces a very complex mountainous system (Figure 4.1) that is protected as a National Park and a Biosphere Reserve. There are two specific study sites. On one hand, the Guadalfeo River Basin upstream of Rules dam (black line Figure 4.1), which has an extension of 1057.3 km$^2$. This site has been previously studied and hydrologically modelled. On the other, a small area inside the previous area, located in the Caballo Mountain hillside, was employed for the validation of the snow cover maps obtained from Landsat imagery (red line Figure 4.1).

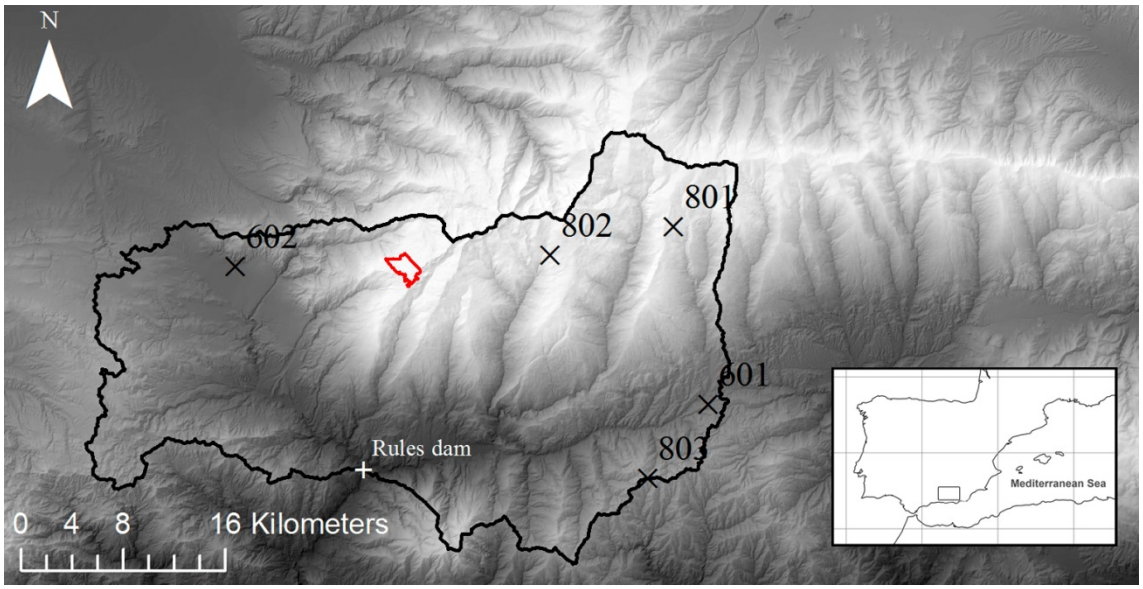


Figure 4.1. Location of Sierra Nevada Mountain Range in Spain, limits of the study area (black line), monitored area by means of TP (red line), Rules dam (white cross) and weather stations employed in the study (black crosses).

### 4.2.1. Meteorological information

Different weather station networks are available in this area; in this work, hourly and daily dataset of precipitation, temperature, radiation (shortwave and longwave), pressure, wind velocity, and relative humidity from the Agroclimatic Information Network of Andalusia (RIA) and the Guadalfeo Project Network (Herrero et al., 2011) are employed as input of the snow model. Given the rough topography, specific interpolation algorithms had to be used; including, in the case of temperature and precipitation, the interpolation was based on the consideration of and elevation trend at different times (Herrero et al., 2007). As for radiation, topographic

effects, like shadowing are also considered (Aguilar et al., 2010). Albedo was calculated according to Pimentel el al. (2013) (Appendix C) and atmospheric longwave emissivity gets use of the formulation proposed in Herrero and Polo (2012).

### Images available

67 Landsat TM and ETM+ scene were employed in the study for the 10-yr period from 2004 to 2013. Figure 4.1 shows the dates and names of the images selected, dates where TP in the monitored Caballo hillside are available are marked with an asterisk. These images were used to validate the results of Landsat analysis.

Table 4.1. Selected Landsat scenes including the study site for the 2004-2013 period. Dates marked with an asterisk represent those where TP is also available.

| Date | Name | Date | Name | Date | Name |
|---|---|---|---|---|---|
| 14 Nov 2004 | LE72000342004319ASN00 | 11 Dec 2008 | LE72000342008346ASN01 | 19 Jun 2011* | LT52000342011170MPS00 |
| 01 Jan 2005 | LE72000342005001ASN00 | 12 Jan 2009 | LE72000342009012ASN00 | 25 Oct 2011 | LT52000342011298MPS01 |
| 02 Feb 2005 | LE72000342005033ASN00 | 13 Feb 2009 | LE72000342009044ASN00 | 10 Nov 2011 | LT52000342011314MPS01 |
| 18 Feb 2005 | LE72000342005049ASN00 | 17 Mar2009 | LE72000342009076ASN01 | 04 Dec 2011 | LE72000342011338ASN00 |
| 06 Mar 2005 | LE72000342005065ASN00 | 04 May 2009* | LE72000342009124EDC00 | 20 Dec 2011 | LE72000342011354ASN00 |
| 17 Nov 2005 | LE72000342005321ASN00 | 29 Jun 2009* | LT52000342009180MPS00 | 05 Jan 2012 | LE72000342012005ASN00 |
| 12 Nov 2006 | LT52000342006316MPS00 | 06 Dec 2009 | LT52000342009340MPS00 | 21 Jan 2012 | LE72000342012021ASN00 |
| 14 Dec 2006 | LT52000342006348MPS00 | 23 Jun 2010 | LT52000342010023MPS00 | 22 Feb 2012 | LE72000342012053ASN00 |
| 30 Dec 2006 | LT52000342006364MPS00 | 29 Apr 2010 | LT52000342010119MPS00 | 09 Mar 2012 | LE72000342012069ASN00 |
| 07 Jan 2007 | LE72000342007007ASN00 | 15 May 2010* | LT52000342010135MPS00 | 10 Apr 2012* | LE72000342012101ASN00 |
| 16 Feb 2007 | LT52000342007047MPS00 | 31 May 2010* | LT52000342010151MPS00 | 12 May 2012* | LE72000342012133ASN00 |
| 12 Mar 2007 | LE72000342007071ASN00 | 08 Jun 2010* | LE72000342010159ASN00 | 13 Jun 2012 | LE72000342012165ASN00 |
| 20 Mar 2007 | LT52000342007079MPS00 | 18 Jul 2010* | LT52000342010199MPS01 | 03 Oct 2012* | LE72000342012277ASN00 |
| 07 May 2007 | LT52000342007127MPS00 | 26 Jul 2010 | LE72000342010207EDC00 | 20 Nov 2012* | LE72000342012325ASN00 |
| 15 May 2007 | LE72000342007135ASN00 | 03 Aug 2010 | LT52000342010215MPS00 | 07 Jan 2013* | LE72000342013007ASN00 |
| 24 Jun 2007 | LT52000342007175MPS00 | 22 Oct2010 | LT52000342010295MPS00 | 24 Feb 2013* | LE72000342013055ASN00 |
| 22 Oct2007 | LE72000342007295ASN00 | 09 Dec 2010* | LT52000342010343MPS00 | 13 Apr 2013* | LE72000342013103ASN00 |
| 07 Nov 2007 | LE72000342007311ASN00 | 10 Jan 2011* | LT52000342011010MPS00 | 31 May 2013* | LE72000342013151ASN00 |
| 27 Feb 2008 | LE72000342008058ASN00 | 03 Feb 2011* | LE72000342011034ASN00 | 16 Jun 2013* | LE72000342013167ASN01 |
| 30 Mar2008 | LE72000342008090ASN00 | 23 Mar 2011* | LE72000342011082ASN00 | 18 Jul 2013* | LE72000342013199ASN00 |
| 18 Jun 2008 | LE72000342008170ASN00 | 31 Mar 2011* | LT52000342011090MPS00 | 19 Aug2013 | LE72000342013231ASN00 |
| 04 Jul 2008 | LE72000342008186ASN00 | 08 Apr 2011* | LE72000342011098ASN00 | | |
| 25 Nov 2008 | LE72000342008330ASN00 | 10 May 2011* | LE72000342011130EDC00 | | |

## 4.3. Methods

The accumulation-snowmelt cycles from 2004 to 2013 were simulated at the study site using the physical and distributed model developed and calibrated by Herrero et al. (2009; 2011). The selected Landsat TM and ETM+ images from the same period were processed and snow cover maps were derived. They are assessed thanks to high resolution snow cover maps obtained from TP in the Caballo hillside monitored area. The model performance was tested against these results. This section describes both the snow maps obtainment and validation and the snowmelt-accumulation model.

### 4.3.1. Snow cover maps obtainment

### Landsat scene

Landsat imagery was selected to represent the significant scales of the snow heterogeneity observed in semiarid areas. 67 images from 2004 to 2013 were selected and analysed in this study (Table 1). This section describes first the different levels of pre-processing needed to transform row image digital numbers into reflectance values, and second, the two methodologies employed to obtain snow cover maps from these datasets.

#### *Pre-processing*

Pre-processing is composed of four different and sequential steps: radiometric, atmospheric, saturation and topographic corrections. First, radiometric calibration by means of rescaling factors (Chander et al., 2009) to transform the calibrated Digital Number (DN) in the original images into radiance values at the sensor was applied. Secondly, the atmospheric Dark Object

Subtraction (DOS), was selected; this algorithm assumes that all atmospheric effects are represented by a blackbody in the image, which by definition must absorb all the solar radiation (Moran et al., 1992; Chavez, 1996), and together with this assumption, several simplifications in the reflectance physic equation, such as a Lambertian surface and a cloudless atmosphere were made. After the atmospheric correction, the obtained reflectance values require additional corrections due to the saturation problems that usually appear in these snowy areas associated with the radiometric configuration of the satellite. Based on the hypothesis of a high correlation between spectral bands for snow, a multivariate correlation analysis between bands was made to recover the snow saturated pixels values (Karnieli et al., 2004). Finally, a C-correction with land cover separation algorithm (Hantson and Chuvieco, 2011) was employed to homogenize direct solar and non-solar illuminated areas in this mountainous rough terrain. Figure 4.2 shows the flow chart of the different stages in the pre-processing of Landsat images.

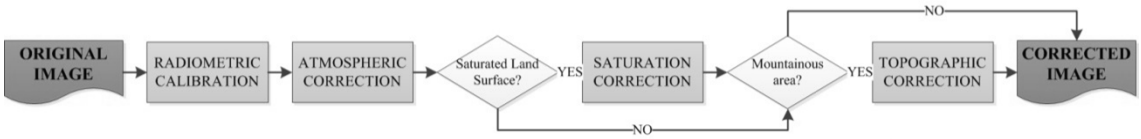


Figure 4.2. Flow chart of the correction process of each Landsat image used in the study

### *Snow maps*

Binary (snow/non-snow pixels) snow cover maps from Landsat images are easily obtained based on the physical properties of the snow along the electromagnetic spectrum: a very high snow reflectance in the visible region and the snow brightness temperature in the microwave region. (Dozier, 1989; Herrero et al., 2011). However, when a subgrid classification is required, a more complex analysis to estimate the snow cover fraction in each cell can be carried out by means of a spectral mixture analysis (Painter et al., 2009). These techniques assume that the reflectance measured by the sensor from a given cell is a combination of the individual reflectance from the different kind of surfaces present within, the endmembers, and provide a finer resolution in both border areas and internal heterogeneous areas in the snow region, not only in the final snowmelt cycle but also during the whole snow season.

*Binary snow cover maps*

Obtaining binary snow cover maps from Landsat dataset can be achieved from the physical properties of the snow along the electromagnetic spectrum: snow has very marked different extreme values in visible (high reflectance) and infrared regions (low reflectance). The use of Normalized Difference Snow Index (NDSI), which compares electromagnetic answers over these spectral regions, allows the discrimination between covered and non-covered snow pixels (Dozier, 1989; Herrero et al., 2011).This index is defined as follows:

$$NDSI = \frac{TM2 - TM5}{TM2 - TM5} \tag{4.1}$$

where $TM_i$ corresponds to the reflectance value in Landsat band i. The discrimination between covered and non-covered pixels is made based on two thresholds: NDSI>0.15 and TM1>0.06. Additionally, a threshold with the minimum elevation with snow presence is employed (Herrero et al., 2011).

*Fractional snow cover maps*

However, this simple classification is prone to errors due to the presence of mixed pixels, not only composed of pure snow, apart from it not being able to represent the snow dynamics under this spatial fixed resolution. Hence, obtaining the fraction of the pixel covered by snow enable us to provide a more adequate description of the processes. The endmembers spectral mixture analysis (Rosenthal and Dozier, 1996; Roberts et al., 1998) allows the obtainment of fractional snow cover in each analysed pixel. This analysis assumes that the radiance measured at the sensor, $R_{S,\lambda}$, is a linear combination of the radiance values reflected from each spectral endmembers, that is, pure surface covers present in the area. Following this,

$$R_{S,\lambda} = \sum_{i=1}^{N} F_i R_{\lambda,i} + \varepsilon_\lambda \tag{4.2}$$

where $F_i$ is the fraction of the endmember i; $R_{\lambda,i}$ is the reflectance obtained after the different pre-processing steps of endmember $i$ at wavelength $\lambda$; N is the number of spectral endmembers taken into account; and $\varepsilon_\lambda$ is the residual error at $\lambda$ associated with the fit of the N endmembers. The least-squares fit to $F_i$ is solved with a reflective Newton method.

Three significant endmembers were identified in the study area; snow, vegetation (brush creeping vegetation) and rocks (phyllite), their spectrum being obtained from a digital spectral library (http://speclab.cr.usgs.gov/) (Figure 4.3).

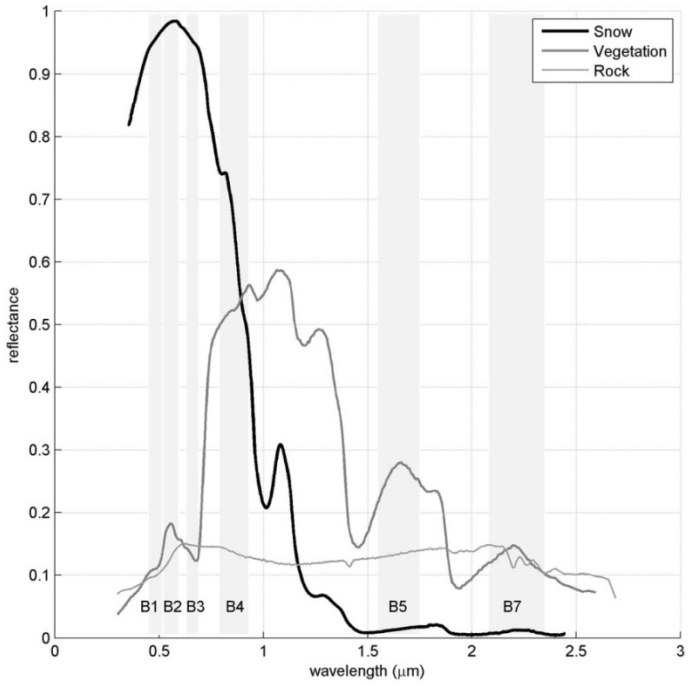


Figure 4.3. Spectral reflectance of the three endmembers (vegetation, snow and rock) identified in the study area, obtained from the USGS digital spectral library. The Landsat TM and ETM+ bands are also represented.

### Terrestrial photography

Snow cover maps from TP are obtained in a two steps process: a) georeferencing and b) snow detection. The first one is achieved following some basic principles of computing design (Foley; 1909; Fiume 1293) and with the support of a Digital Elevation Model (DEM). The aim of this process is to find a function that relates the two dimensional pixel in the photo to the three

dimensional point in the DEM (Corripio et al, 2009; Pimentel et al, 2012). The second step is performed using machine learning techniques. An unsupervised k-means algorithm is employed to distinguish between covered and non-covered pixels. The results are snow cover maps with the same spatial resolution of the DEM and the temporal resolution of the acquisition process. Thus, the results can be adapted to the temporal and spatial resolution of the processes studied.

### Validation of snow cover maps

Snow maps obtained from TP at 10 x 10m spatial resolution were employed to validate both snow maps, binary and fractional, from Landsat TM and ETM+ (30 x 30m) in the Caballo Mountain hillside (red line in Figure 4.1).

To make the comparison between both, virtual fractional snow maps at 30 x 30m resolution were obtained from binary TP maps. Different performance metrics were employed to evaluate the accuracy of the analysis (Painter et al., 2009). On one hand binary metrics:

$$\text{Precision} = \frac{TP}{TP + FP} \tag{4.3}$$

$$\text{Recall} = \frac{TP}{TP + FN} \tag{4.4}$$

$$Accuracy = \frac{TP + TN}{TP + TN + FP + FN} \tag{4.5}$$

where, TP represents true positive (snow in both pixels compared); TN represents true negative (no snow in either pixels compared); FP represents false positive (snow in the evaluated dataset and no-snow in the validated dataset); and FN represents false negative (no-snow in the evaluated dataset and snow in the validated dataset).

And on the other hand fractional metrics:

$$RMSE = \sqrt{\frac{1}{(\mathrm{N}-1)} \sum_{j=1}^{N} \left[ Evaluated\ SCF(\mathrm{j}) - Validated\ SCF(j) \right]^2} \tag{4.6}$$

### 4.3.2. Snow modelling

The snowmelt-accumulation model for Mediterranean sites developed by Herrero et al (2009) is a physical model based on a point mass and energy balance, which is extended to a distributed way by means of depletion curves (Herrero et al., 2011; Pimentel et al., 2014).

The model assumes a uniform horizontal snow cover surface distributed in one vertical layer. In the control volume defined by the snow column per unit area, which has the atmosphere as an upper boundary and the ground as a lower one, the water mass and energy balance can be expressed by:

$$\frac{d\,SWE}{dt} = R - E + W - M \tag{4.7}$$

$$\frac{d(SWE \cdot u)}{dt} = \frac{dU}{dt} = K + L + H + G + R \cdot u_R - E \cdot u_E + W \cdot u_W - M \cdot u_M \tag{4.8}$$

where *SWE* (snow water equivalent) is the water mass in the snow column, and *u* is the internal energy per unit of mass (*U* for total internal energy). In the mass balance, *R* defines the precipitation rate; *E* is water vapour diffusion rate (evaporation/condensation); *W* represents the mass transport rate due to wind; and *M* is the melting water rate. On the other hand, regarding energy fluxes, *K* is the solar or short wave radiation; *L* the thermal or long-wave radiation; *H* the exchange of sensible heat with the atmosphere rate; *G* the heat exchange with the soil rate; and $u_R$, $u_E$, $u_W$ and $u_M$ are the advective heat rate terms associated with each one of the mass fluxes involved in Eq. (4.7).

The calibration of the model by field data shown in Herrero et al. (2009) was used in this work to simulate the whole study period.

This approach permits an easy extension to a distributed model making calculations simultaneously in each cell. However, a direct extension cannot be done when the cell area is not completely covered by snow. In such cases, the parameterization of subgrid processes is made by including depletion curves, which are empirical functions that relate the fraction of cell area covered by snow to some other snow state variables, and quantify the decrease in snow cover within the cell to take into account the reduction of the area implied in the energy-mass balance. Because of the annual occurrence of different snowmelt cycles during the snow season and their variability between years, different depletion curves were proposed for each kind of melting/accumulation cycle identified in the area (Pimentel et al., 2014). A general sigmoid parameterization was proposed:

$$\begin{aligned} SCF_i^* &= SCF_{i_{\max}}^* \left(1+\frac{h_{i_e}^*-h_i^*}{h_{i_e}^*-h_{i_m}^*}\right)\left(\frac{h_i^*}{h_{i_e}^*}\right)^{\frac{h_{i_e}^*}{h_{i_e}^*-h_{i_m}^*}} \qquad if \quad 0 \le h_i^* < h_{i_e}^* \\ SCF_i^* &= SCF_{i_{\max}}^* \qquad if \quad h_i^* \ge h_{i_e}^* \end{aligned} \tag{4.9}$$

where $SCF_i^*$ and $h_i^*$ are dimensionless expressions for the snow cover fraction and snow depth obtained for each melting cycle (i) by means of the maximum snow cover fraction and snow depth at the beginning of the snowmelt period respectively . The three parameters: $SCF_{i_{max}}^*$, maximum value of $SCF^*$; $h_{i_e}^*$, dimensionless depth when melting begins; and $h_{i_m}^*$, dimensionless depth when the maximum melt rate is achieved were obtained from in situ measurements.

## 4.4. Results and discussion

This section firstly shows the different snow maps resulting from both analyses, binary and fractional, were shown. Then the validation process of these images is drawn, through the use of TP over the small control area of Caballo Mountain hillside, to determine the methodology that best represents the area covered by snow. Finally, the snowmelt-accumulation model was validated in the Guadalfeo River basin with the selected snow cover maps.

### 4.4.1. Snow cover maps

Binary and fractional snow cover maps, for the 10-yr series of Landsat images were obtained. Figure 4.4 shows the evolution of the global snow area at the study site throughout the period 2004-2013 using both methodologies. Parallel temporal trends can be observed, with

overestimation of snow area for binary maps, as expected, since there is a threshold over which this analysis results in a completely covered classification. This is particularly relevant during accumulation phases, with maximum differences usually obtained for the maximum SCF values of every year. Melting stages generally exhibit closer values, especially during the final melting cycle of each hydrological year. A Root Mean Squared Error (RMSE) of 15.6 $km^2$ was obtained by comparing both kind of results over the study period, which involves a notable change by using spectral mixture analysis given that the maximum snow cover area found ranged from 370 to 330 $km^2$.

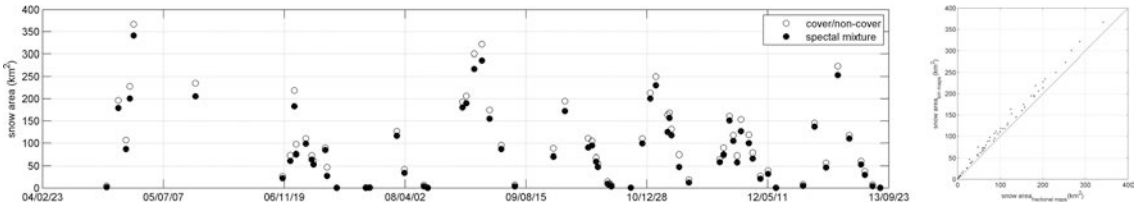


Figure 4.4. Comparison throughout the ten year analysed between the snow area resulting from both binary and fractional maps obtained from Landsat images (left). Dispersion graph of the comparison (rigth).

Figure 4.5 A) depicts the snow distribution for three selected dates during the study period, associated with different states throughout the snow season (beginning of accumulation, consolidated snow and beginning of melting). Moreover, Figure 4.5 B) includes the fraction of area associated with covered (SCF=1), non-covered (SCF=0) and mixed (0<SCF<1) situations for all the dates studied. Obviously, the covered-non covered analysis does not discriminate mixed cells. The results show that the non-covered area is similarly represented by both this algorithm; however, a significant portion of cells considered as snow-covered do not correspond to SCF=1, with an associated area that can be close to 50% of the estimated snow area by the binary analysis.

These mismatched pixels are usually located along the border sites of the snow, as can be seen in Figure 4.5 A), where the interaction between the melting snow and rocks is stronger. Furthermore, the spectral mixture methodology allows the representation of the distribution of these mixed pixels over the area.

### 4.4.2. Validation of snow cover maps

To assess the accuracy of snow maps obtained from Landsat imagery, TP was employed. A total of 24 TPs from the same days on the Landsat scene were georeferenced (dates marked with an asterisk in Table 1). A DEM of 10 m cell size was used. The maps obtained were reshaped to 30 x 30m to make the comparison with those obtained from Landsat. The information provided by these maps was assumed to be the "truth" for pixels that either have or do not have snow (a threshold of 15% of total coverage in each pixel is adopted to consider a pixel as being covered).

These TP-snow maps were compared with both the binary maps and the spectral snow ones obtained from Landsat and shown in previous section. In the analysis, two questions were answered for both methodologies: on one hand if Landsat snow maps locate snow in the same place that TP-snow maps; on the other hand, whether the amount of snow in terms of snow cover fraction, pixel by pixel over the complete area is correctly represented by the methodologies employed. The first question is solved by means of the binary metrics shown in Eqs. (4.3, 4. 4, and 4.5) precision, recall and accuracy; and the second one with the statistics Eq. (4.6): RMSE (pixel by pixel analysis) and $RMSE_{global}$ (complete area).

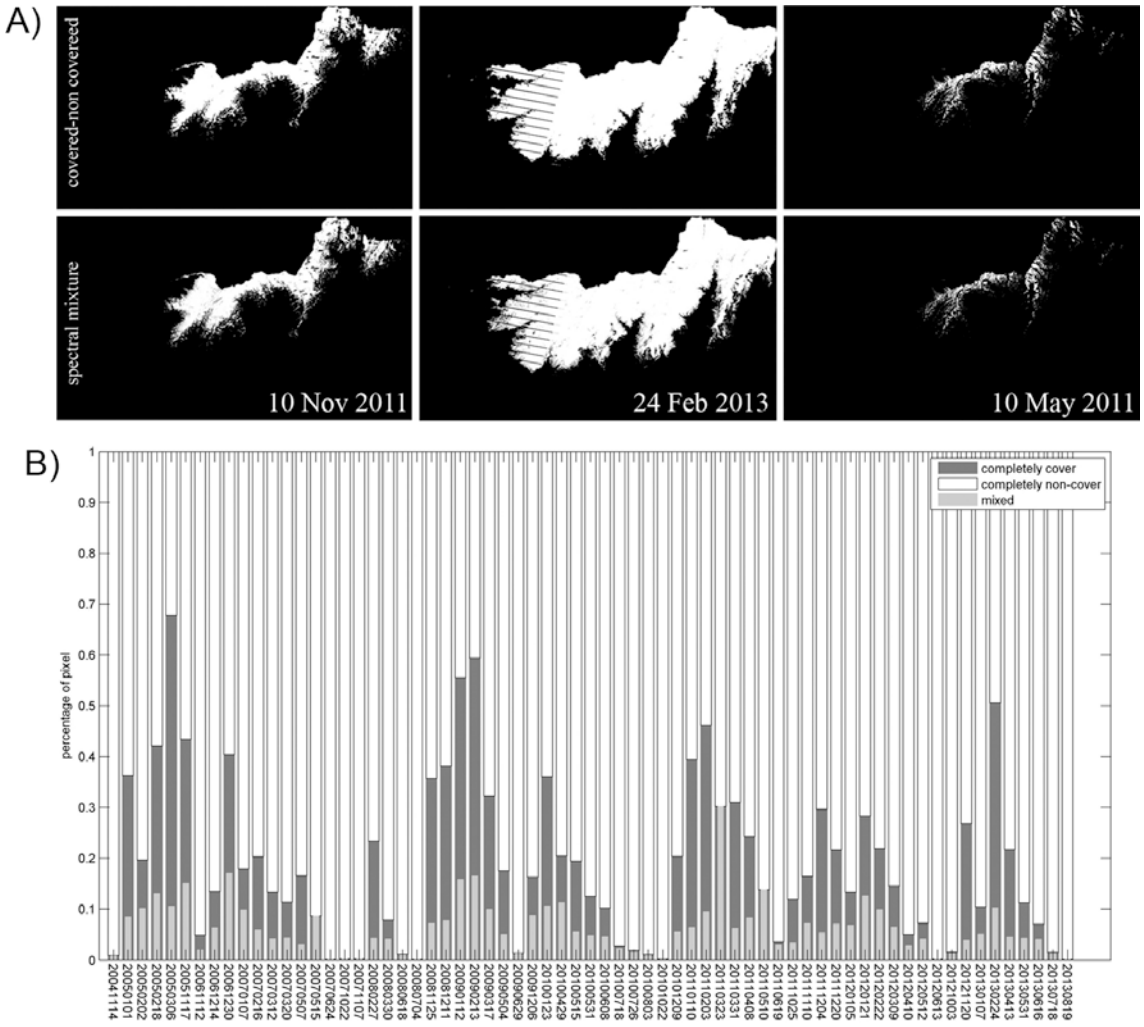


Figure 4.5 A) Selected snow maps for 10 Nov 2011, 24 Feb 2013 and 10 May 2011 (up, covered-non covered classification, and down, spectral mixture analysis). B) Bar graph which the percentage that each kind of pixel representes.

Figure 4.6 shows the different values for the binary metrics obtained. Precision, which describes the percentage of all positive mapping results that truly identify snow, ranges from 0.65 to 1 with a mean value of 0.80 for binary maps and from 0.52 to 1 with a mean value of 0.79, from fractional maps. Recall describes the fraction of all the snow in the scene that is identified. It ranges from 0.5 to 1 with a mean value of 0.79 for binary maps; and, from 0.65 to 1 with a mean value of 0.80 in the case of fractional maps. Finally, accuracy, which represents all the pixels correctly identified, as snow and no-snow, ranges from 0.7 to 1, with a mean of 0.89 for binary maps; and, from 0.9 to 1 with a mean of 0.96 from fractional maps. In Figure 4.6 A) more statistics of this analysis are shown. Figure 4.6 B) shows a representation of these metrics in relation to the total area measured in each of the images. Acceptable values for precision and recall, greater than 0.8, were achieved over a threshold of 0.3 over the percentage of snow in the whole area. Thus, the worst performance of these metrics was associated with lower values of snow area. In the case of accuracy, the performance was high for the images analysed. Moreover, in most of the cases, binary metrics of fractional maps (crosses) have greater values than those obtained for binary maps (dots).

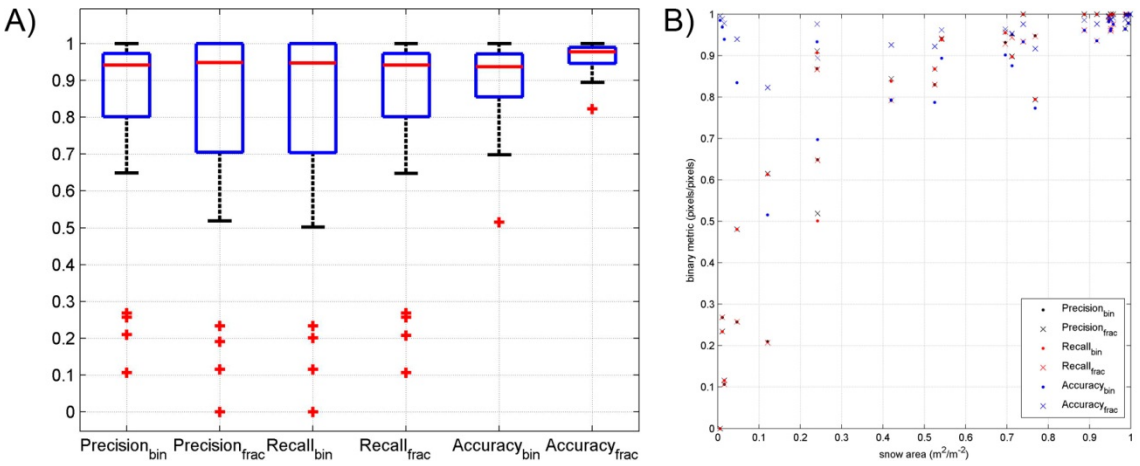


Figure 4.6 Binary metrics (precision, recall and accuracy) of both binary and fractional maps versus snow maps obtained from TP. A) Boxplot of each metric. On each box, the red central mark represents the median, the blue edges are the 25$^{th}$ and 75$^{th}$ percentiles, the black whiskers extends to the most extreme data point not considered outliers, and red crosses are the different outliers. B) Representation of the snow cover over the total area versus each of the values of the binary metrics

Hence, binary metrics show a generally good performance in snow detection for both methods, with mean values of around 80% for precision and recall. Better achievements are obtained for fractional than for binary maps, with a mean improvement of 3%. In the case of accuracy, the performance reaches values of 95% for fractional maps, which represents a mean of 7% compared to binary maps.

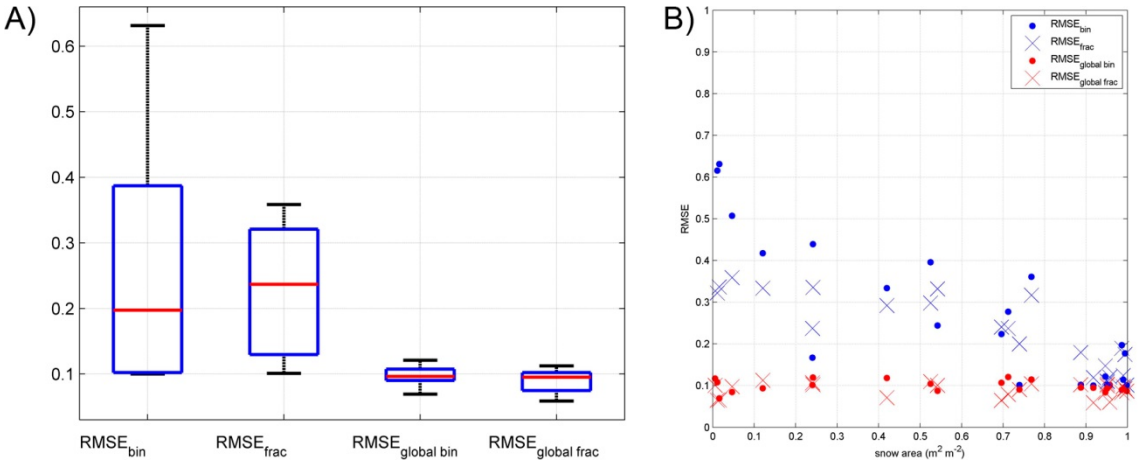


Figure 4.7 Binary metrics (precision, recall and accuracy) of both binary and fractional maps versus snow maps obtain from TP. A) Boxplot of each metric. On each box, the red central mark represents the median, the blue edges are the 25$^{th}$ and 75$^{th}$ percentiles, the black whiskers extends to the most extreme data point; B) Representation of the snow cover over the total area versus each of the values of the binary metrics

Figure 4.7 shows the values of the comparison in terms of snow fractional cover. Figure 4.7 A) shows different statistics for RMSE and $RMSE_{global}$ using both methods. Binary maps reach a value for RMSE of 0.25 $m^2$ $m^{-2}$, while fractional maps reduce this error to 0.20 $m^2m^{-2}$. If the errors are calculated over the whole area, the improvement is outstanding ,as the mean error is reduced in both cases to values lower than 0.10. Figure 4.7 B) shows these errors compared to the percentage of snow measured in the whole area. For $RMSE_{global}$, the distribution follows a constant trend around 0.1 $m^2$ $m^{-2}$, in both binary maps (red dots) and fractional maps (red crosses), with a slight improvement for the case of fractional maps. The behaviour is different for RMSE, its improvement achieved by fractional maps was greater. They follow a decreasing trend with the measured snow area. Two intervals can be distinguished: a first one of between 0

and 0.7 of snow area, with a mean RMSE of 0.25, and a second one that ranges from 0.7 to 1, with a mean RMSE of 0.1.

According to these results, snow fractional maps represent with a greater precision recall and accuracy in the snow area and also produce smaller errors in pixel to pixel and in global comparisons. Therefore they can be used as "truth" snow cover maps for calibration and validation. Moreover, some uncertainty can be included thanks to the results of the validation process. Another important aspect to be mentioned related to uncertainty is the spatial resolution selected for the comparison. The selection of a larger cell size, as for example in Painter et al. 2009, could reduce the errors. Nevertheless, due to the representative scale of the snow patches characteristic of snow distribution over this area, increasing the cell size analysis would be meaningless.

### 4.4.3. Snow cover simulations

The 10-yr study period was simulated with the distributed snow model previously described with the calibration values obtained in Chapter 3. Based on the results of the previous section, the snow fractional maps obtained from Landsat were used to validate these simulations. Figure 4.8 shows the comparison of both, the snow area in the watershed simulated over the study period and the average snow area value obtained from each Landsat image (black dots). A great level of accuracy in the simulation can be generally observed. A global RMSE=0.046 $km^2$ $km^{-2}$, associated with 48.72 $km^2$ of snow area, is obtained. The dispersion graph also shows this outstanding fact.

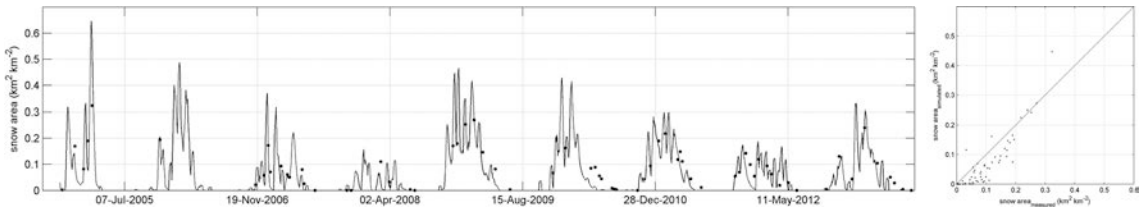


Figure 4.8. Evolution of mean SCF over the watershed. Black line represents simulated values and black dots are the estimates from spectral mixture analysis of Landsat imagery

Figure 4.9 shows a comparison between the spatially simulated and observed distribution of snow throughout the watershed for the three selected images. As can be observed, the border cells are not always correctly represented. Moreover, some snow-free areas that appear inside the completely covered area are not represented by the model. This characteristic snow distribution can usually be found and is generally due to wind effects. As the model does not considered the redistribution of snow by wind transport, therefore these mismatches are likely to appear when windy conditions between two consecutive images are not negligible.

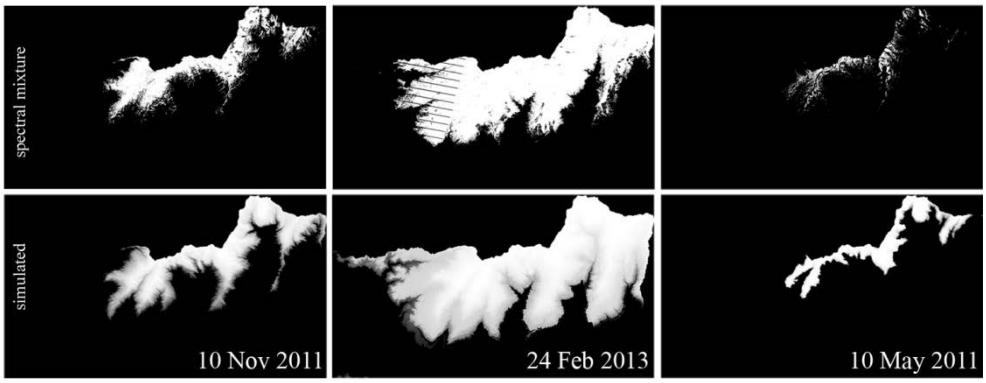


Figure 4.9. Comparison between measured (up) and simulated (down) snow cover fraction maps for three selected dates belong to three different stages of the snow cycle

To analyse this performance in a numerical way, the same binary metrics employed in validation process were calculated (Figure 4.10). In this case, snow fractional maps are considered as being the "truth" in the comparison. Precision values range between 0.3 and 1 with a mean value of 0.78. Recall, with a mean value of 0.70, indicates that a slight underestimation in the total snow area simulated takes places. In the case of accuracy, higher values were obtained, with a mean value of 0.94. Figure 4.10 A) shows other statistics of the analysis. As in previous analysis Figure 4.10 B) helps to understand when the worst performance was obtained. The greatest mismatches took place when the snow areas were most reduced. In general, this period belonged to the final stage of the melting process, when the distribution of snow was more heterogeneous and a greater number of mixed pixels appeared. An example of that can be found in the right maps of Figure 4.9 belonging to 10 May 2011, where a very patched snow surface can be observed.

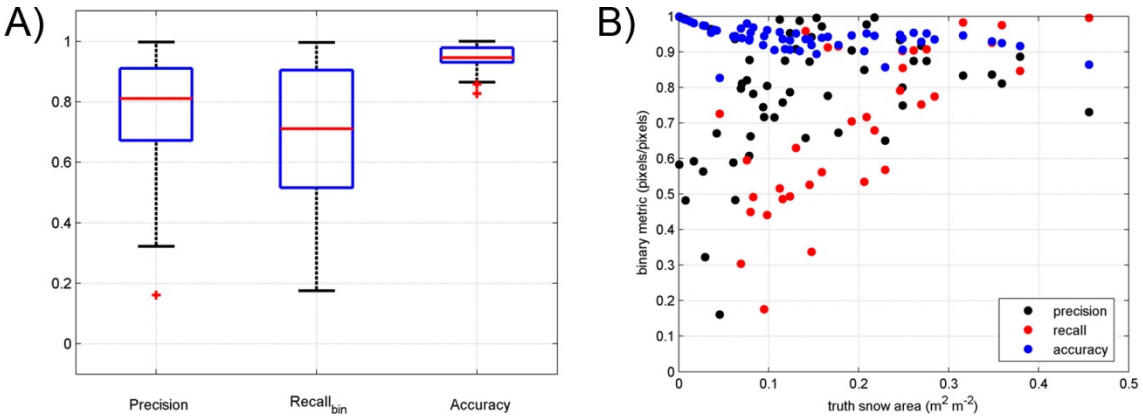


Figure 4.10. Binary metrics (precision, recall and accuracy) of both binary and fractional maps versus snow maps obtain from TP. A) Boxplot of each metric. On each box, the red central mark represents the median, the blue edges are the 25$^{th}$ and 75$^{th}$ percentiles, the black whiskers extends to the most extreme data point not considered outliers, and red crosses are the different outliers. B) Representation of the snow cover over the total area versus each of the values of the binary metrics

## 4.5. Conclusions

The distribution of snow cover under highly variable conditions was obtained using Landsat imagery. Two methodologies were tested against snow cover maps at a higher resolution obtained by means of TP. Fractional snow cover estimated by spectral mixture analysis, was selected as the best methodology, and reveals itself as a powerful tool for providing time map series to be used in snow modelling. The spectral mixture analysis allows an adequate estimation of the coverage of snow in each pixel of the area, which resulted in a global

reduction of the snow cover area close to 50% in the mixed identified cells when compared to a simple covered-non covered classification analysis. This is especially important in these semiarid mountainous regions where the particular snow dynamics favours the appearance of a large number of mixed pixels.

The calibrated model by Herrero et al. (2009, 2011) has been validated by the good agreement between simulated and observed snow maps. The combination of these snow cover fraction maps with physical distributed snow modelling allows an indirect validation of other simulated snow variables, i.e. snow water equivalent and snow depth. The mismatching areas may correspond, among other effects, to locations and periods for which wind transport, not being considered in the snow model due to its complexity at high altitudes, is not negligible. The spatial resolution of Landsat data makes this source a powerful tool when combined with quantifying classification techniques, such as the spectral mixture analyses used in this work.

# CHAPTER 5: CONCLUSIONS

## 5.1. General conclusion

This study highlights the need of considering microscale effects in snow modelling in semiarid environments, since certain processes at this scale highly condition the heterogeneous spatial distribution of the snow over these areas. A combination of both snow physical modelling and snow observation is employed to describe these effects.

The use of terrestrial photography to study the snow evolution at the microscale resolution has permitted the continuous monitoring of this layer, adapting the resolution of the observation to the scales of the processes. Besides its use as raw observation datasets to calibrate and validate models' results, terrestrial photography constitutes valuable information to complement weather stations observations. It allows the discriminating possible mistakes in meteorological observations (i.e. overestimation on rain measurements) and a better understanding of snow behaviour agains certain weather agents (i.e. blowing snow). Thus, terrestrial photography is a feasible and convenient technique to be included in weather monitoring stations in mountainous areas in semiarid regions.

Terrestrial photography observations have been used as indirect dataset to the implementation of a data assimilation scheme. An ETKF has been developed and significantly improved the simulations of snow dynamics at the subgrid scale. This prevented some of the mismatches that occur at certain moments during the snow season due to the highly variable conditions or to some processes not explicitly included in the physical modelling being significant. The assimilation of snow cover fraction has also led to choosing the depletion curve standardization that best reproduces the snow distribution at subgrid scale. The results point to the adoption of a selective curve procedure depending on the occurring snow cycle as the optimal simulation procedure. This selection is in line with the variability shown between different snowmelt cycles during the snow season. Despite the improvement produced, however, this selective depletion curve is not always capable of sufficiently mitigating the mismatch of the modelling for given periods.

These results led to a different approach to explore further the microscale information. The terrestrial photography datasets at this resolution were also employed as direct observations to define snow depletion curves in the study area. Two general depletion curves were proposed from the analysis of each accumulation-melting cycles to represent the accumulation or the melting stage in each cycle; furthermore, the sigmoid curve associated to the melting periods was split into different parameterizations depending on the snow state and trend, to associate the choice to some physical properties of the snow. As a result, four depletion curves are proposed to explain the variability found between cycles and years. The different melting cycles identified were classified according to: a) cycles with great amount of consolidated snow; b) cycles with a great amount of recent snow; c) cycles with little snow during the cold season; and d) cycles with little snow during spring. The inclusion of this flexible parameterization from local observations in the modelling led to an improved performance of the simulations, with better accuracy than those obtained with the previous data assimilation scheme.

The new parameterization proposed was finally included in the completely distributed snowmelt-accumulation model; decision-tree algorithm based on information related to the physical state of snow was implemented in the model for the automatic selection of each curve

during the calculation process.. The snow cover fraction maps obtained from the 10-yr simulation of the study area through the resulting distributed model were validated against the snow cover maps resulting from endmembers multispectral mixture analysis of Landsat TM and ETM+ imagery. These “observed” snow cover fraction maps (30x30m) had been previously assessed by means of the use of terrestrial photography at hillside scale (10x10m) over one of the study areas in this work. This validation process showed how the spectral mixture analysis allows an adequate estimation of the coverage of snow in each pixel of the study area, with a high improvement from a simple covered-non covered classification analysis, which resulted in a global reduction of the snow cover area close to 50% in the group of cells identified as mixed under the simpler approach. This is especially important in these semiarid mountainous regions where the particular snow dynamics favours the appearance of a great number of these mixed pixels.

A satisfactory accuracy was found in this final validation process both in the average and distributed results; nevertheless, in a pixel by pixel analysis some mismatches still remained in areas and periods highly conditioned by wind transport effects. The results allow focusing further efforts on these areas and conditions to incorporate with accuracy the wind terms in the energy and mass balance equations from sound interpolation algorithms, and transport coefficients. The implementation of additional terrestrial photography monitoring systems at selected sites within these identified areas may help to assess this wind contribution to the final snow distribution evolution in semiarid environments.

Microscale data observations from terrestrial photography have led to identify states for which nor their direct (assimilation) nor indirect use (improving the depletion curves expression) resulted in a better performance of the snow model at the study site. Weather observations allow us to assess possible reasons for that, being wind significance and the correct determination of the fraction of snow/rainfall in the model, two issues to be addressed. Additional assimilation processes may identify whether these or additional uncertainty sources are the main reason behind the model mismatching for such states. However, this work highlights the capability of physical modelling for not only reproducing environmental variables and their evolution, but also to gain insight into the modelled processes. Furthermore these results, a mixed approach to generate depletion curves and also assimilate terrestrial photography data, from the partition of the dataset in different periods, could improve the model performance at this area for distributed simulations. Finally, the combination of the distributed model with the assimilation of the improved Landsat-derived snow maps is a sound basis for an operational system of snow distributed evolution forecasting system at this area.

## 5.2. Future Research Lines

This thesis shows the importance of considering snow microscale distribution in snow distributed modelling. From the above findings and limitations, the following research lines are now open.

Snow modeling:

- To further analyze the specific areas where the snow simulation is not supported by snow observations. Wind influence has been identified as the main mismatched factor. The inclusion of wind influence on snow dynamics must be done in the modelling. This study must be focused in two aspects: 1) a better representation of wind interpolation over rough

terrain; and 2) the study of advective transport capacity of wind. Furthermore, this analysis must be done at different scales to identify effects that can be significant when upscaling the results. Nevertheless, other factors could be affecting this mismatched (i.e. the curvature of terrain, the solar radiation of specific point, the slope…) and the reasons behind must be addressed in this additional study.

- To take advantage of data assimilation in the modeling at medium-large scales. To implement this, data-fusion techniques applied to remote sensing information provide higher spatial and temporal resolutions in the snow maps dataset series, not only for calibrating-validating objectives but also for the assimilation process. Terrestrial photography has proven to be a good complementary tool to increase the spatial and temporal resolution of snow observations at the cell and hillside scales. These data-fusion techniques, for example the combination of Landsat (30 x 30m spatial resolution and 16-day temporal resolution) and MODIS (250 x 250 m and daily images) information, allow covering the lack of information between consecutives images. A global scale analysis can be done from these three snow data sources, which will highlight microscale processes influence on the distributed evolution of the snowpack.

Snow observation:

- To assess the potential use of terrestrial photography to provide information of other snow variables as part of conventional snow monitoring systems. Up to now only snow cover fraction, and snow depth values have been derived from terrestrial photography in this study. Other snow characteristics such as albedo, snow age or snow roughness could be monitored from information in the images such as brightness or temperature colour. Moreover, different terrestrial imagery that focuses in a different interval of the electromagnetic spectrum can facilitate additional information of the snow state, providing a high-frequency multiscale scope for its analysis from the combination of different distances, angles and spatial resolutions.

# APPENDIXES

# Appendix A: Monitoring snow cover area in semiarid regions using terrestrial photography

*Terrestrial photography is a powerful alternative to remote sensing when scale issues arise (e.g. snow evolution in semiarid regions) since its spatiotemporal resolution can be adapted to the scale of the process. This work shows a graphic user interface (GUI) developed in MATLAB to facilitate the specific steps in those image analyses required to quantify the area covered by snow: (1) a georeferencing process, to provide spatial coordinates to the images, and (2) a snow detection process, to distinguish snow-no snow pixels. This tool has been evaluated over the Sierra Nevada Mountains (southern Spain), where in three different locations it was able to successfully capture the variability of snow behavior. The capability and versatility of terrestrial photography for easy and continuous monitoring of snow was shown from the results.*

This chapter has been presented as oral communication in HIC 2014-11th International Conference on Hydroinformatics: Pimentel, R., Pérez-Palazón, M. J., Herrero, J. and M. J., Polo: Monitoring snow cover area in semiarid regions using terrestrial photography.

## A.1. Introduction

The important role of snow in hydrologic mountain regimes increases in semiarid environments. (Elder et al., 1991). In these areas, due to the presence of recurrent drought stages, snowpack constitutes one of the main reservoirs of water during the dry season. However, measuring and monitoring snow evolution is hard work in these areas, where the extreme and highly variable climate conditions increase the heterogeneity of snow distribution. Snow cover area (SCA) is one of the best snow state variables to explain this snow spatial heterogeneous behaviour (Rango et al., 1976; Herrero et al., 2013).

Currently, the most popular techniques employed for the detection of snow in medium-large areas include satellite remote sensing. Simple procedures, based on physical properties of the snow throughout the electromagnetic spectrum, are employed to distinguish between snow and non-snow areas (Dozier et al., 1981; Hall et al., 2008). However, the efficiency of these techniques may be reduced when the representative scale of the study problem is lower than their fixed resolution (e.g. NOAA, daily images with 1 x 1 km cell size; MODIS, daily images with 250 x 250m cell size; Landsat, 16-day images with 30 x 30 m cell size). Snow in semiarid regions is subject to some of these limitations such as the persistence of small snow patches (O~1m) during many weeks in early summer and the rapid snow melt on sunny and warm days. Thus, the use of other monitoring methods is needed.

An economic alternative to the conventional satellite remote sensing techniques is the use of terrestrial photography. These images are taken from the Earth's surface and have the advantage of a flexible adaptation to temporal and spatial resolutions of the processes studied (Pimentel et al., 2012). Terrestrial photography is not projected over a horizontal plane and does not possess any spatial reference, so that a georeferencing process has to be applied. Basic graphics design principles are employed to define the georeference algorithm (Corripio, 2004). The snow is detected by using a non-supervised clustering algorithm, in which case only the visible range of the spectrum is employed.

In accordance with previous considerations, this study proposes the implementation of the algorithm needed to obtain snow cover maps (georeferencing process and snow automatic detection), by means of a GUI developed in MATLAB. This implementation allows the obtainment of snow georeference maps by users in an easy way. The tool was tested over different locations in Sierra Nevada Mountain, southern Spain.

## A.2. Methods

A GUI to georeference terrestrial photography and detect snow, was developed by means of MATLAB's Graphical User Interface Design Editor (GUIDE). This section explains the methodology employed by both. Figure A. 1 shows the flux diagram of the process to obtain snow maps.

### A.2.1. Georeferencing process

The aim of this process is to find a function to relate the two-dimensional pixels in the images to the three-dimensional points in a Digital Elevation Model (DEM). This function allows the projection over a horizontal plane of images also giving a correct spatial location. Standard procedures for viewing with computer graphics are employed to achieve this (Fiume, 1898; Foley et al., 1990). A transformation matrix, which includes translation, rotation and projection, is applied to the DEM points. This mapping function translates the coordinate system of the DEM to the camera position and applies a transformation according to the focal length and view direction (Figure A. 1 b). The result is a virtual photograph of the DEM, that is, a representation of it as it would be seen from the point of view of the camera (Figure A. 1 c). The two-dimensional representation of the DEM is then scaled according to the resolution of the photograph (Rivera et al., 2008). In this way, the two representations can be superimposed thanks to some control points known in both; establishing the necessary correspondence between a pixel in the photograph and its projection coordinates in the DEM (Figure A. 1 e). The final result is a map in which all the pixels in the TP have been located over the terrain (Figure A. 1 f).

The final accuracy of the resulting map is closely related to the quality of the DEM together with the image quality (level of distortion induced by the lens during the acquisition process).

### A.2.2. Snow detection process

To distinguish the snow-covered and non-covered pixels in each image, a clustering algorithm was applied. These unsupervised methods are generally used to group together data according to a certain notions of similarity. In this case, all the white points in the scene are linked to the presence of snow, so that two clusters can be easily defined: snow-covered and non-covered pixels. A K-mean clustering (MacQuenn, 1967) was selected; this algorithm classifies the data into a given number of clusters, selecting a random center within each cluster and minimizing the distance between the data and these centers. This algorithm proved to be efficient enough to differentiate these two kinds of pixels since it was capable of detecting most of the snow area with no previous calibration or the use of fixed thresholds in the images, with a resulting low level of misclassifications, which were in turn related to the presence of strong shadows in the images (Pimentel et al. 2012). From this pixel classification, the SCF can be easily calculated (Figure A. 1 g).

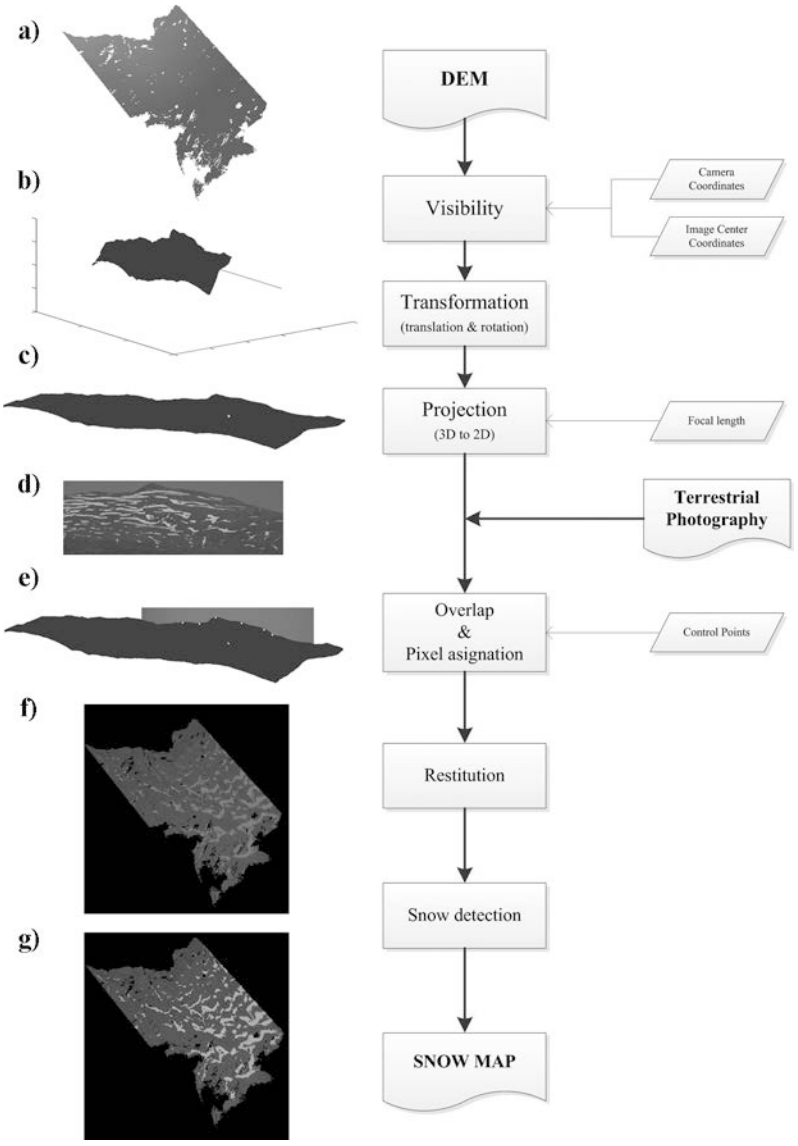


Figure A. 1 Diagram flux of the snow map obtaining process

## A.3. Graphic User Interface

The GUI developed in MATLAB is shown in Figure A. 2. All the inputs required are specified in configuration file: 1) the camera location coordinates; 2) the coordinates of the central point of the image; 3) the location of some control points in both the DEM and the image; 4) the focal length of the camera; and 5) the paths of the DEM and terrestrial photography. This file is loaded in ZONE A (Figure A. 2), where, moreover, the information available is shown. In this area a pull-down menu to select between the different loaded images also appears. The georeference and snow detection processes are realized by means of two buttons located in the two different visualization areas in the GUI (Figure A. 2 ZONE C and ZONE B, respectively). Finally, in ZONE D the user can select, from different formats, how to save the snow maps.

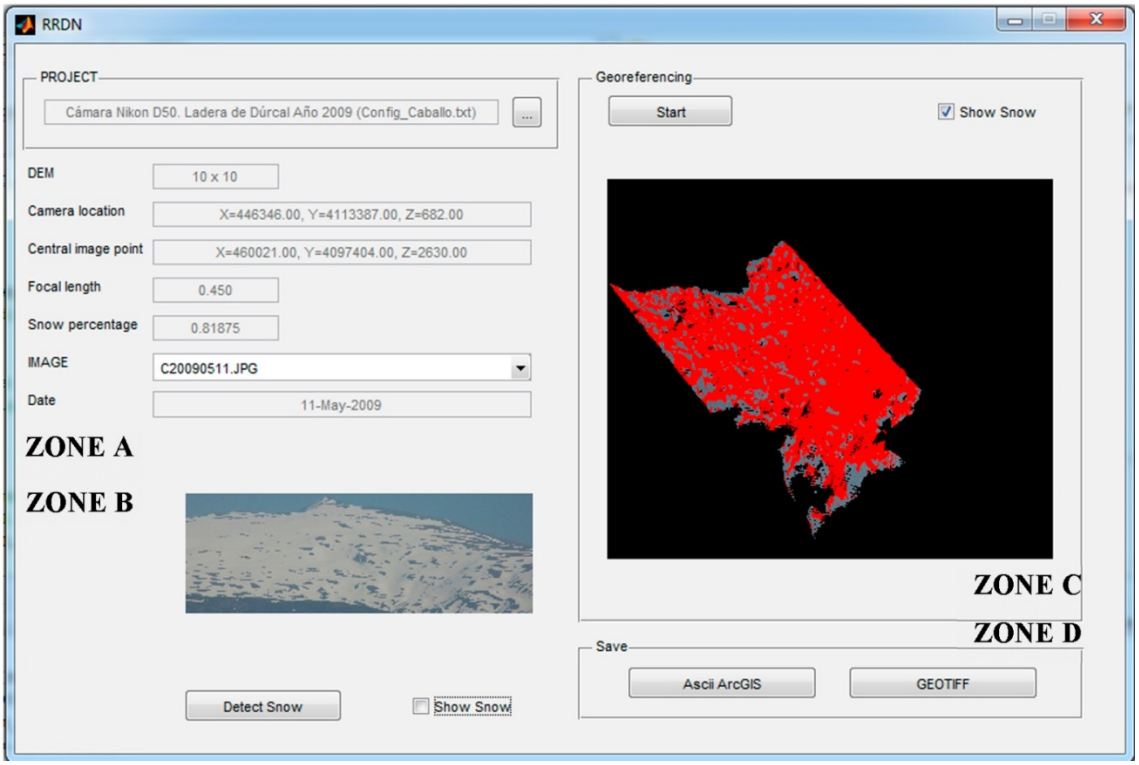


Figure A. 2 GUI tool for georeferencing terrestrial photography and detecting snow. Four areas can be distinguished: ZONE A, where the input file is loaded and information available on it is shown; ZONE B, where the original terrestrial photography is visualized and the button for snow detection is located; ZONE C, the second visualization area, where the georeferenced button appears; and ZONE D, where different output formats can be selected.

## A.4. Application example

This tool has been applied over different locations in Sierra Nevada Mountains, southern Spain. They form a linear mountain range 60 km long, parallel to the coastline of the Mediterranean Sea. The mountain climate is modified by its proximity to the sea, which generates semi-arid Mediterranean and tropical conditions in the surrounding area. These conditions make the snow, which usually appears in altitudes of over 2000 m, be distributed irregularly. (Figure A. 3)

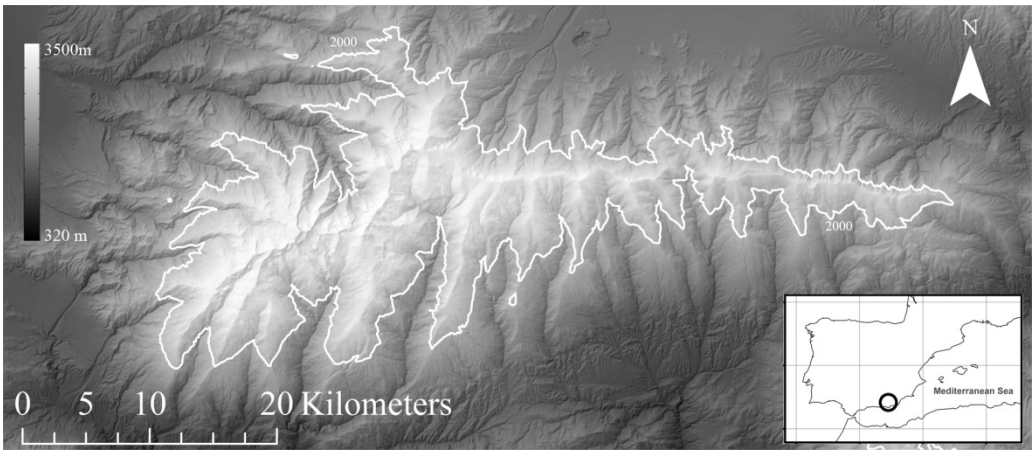


Figure A. 3 Location of Sierra Nevada Mountain, southern Spain

Several automatic cameras were installed over this area to capture different behaviour in snow dynamics. shows different technical information about the cameras installed and the images reordered.

Table A. 1 Technical information of each one of the cameras employed

| Camera | Installation | Temporal resolution | Spatial scale | Photo resolution (pixels) |
|---|---|---|---|---|
| Sony IPELA SNC-RZ50P | 2011/11/20-opperational | 4 images per hour (4 different location, from 7 a.m. to 7 p.m.) | Hillside (O~10m) | 640 x 480 |
| Canon EOS Digital Rebel XS | 2011/09/15-2013/09/15 | 8 images per day (from 8 a.m. to 19 p.m.) | Basin (O~100m) | 3888 x 2592 |
| CC640 Campel Scientific | 2009/07/22-opperational | 5 images per day (from 8 a.m. to 4 p.m.) | Detail (O~m) | 640 x 504 |

Figure A. 4 shows different examples of some of the images processed. Those selected show the validity of the techniques at different scales, from right to left: hillside scale, basin scale and detail scale. In each case the spatial resolution of the final snow maps depends on the DEM employed (10 m x 10m; 30 m x 30 m and 0.1 x 0.1 m). Temporal resolution matches the resolution of the acquisition process.

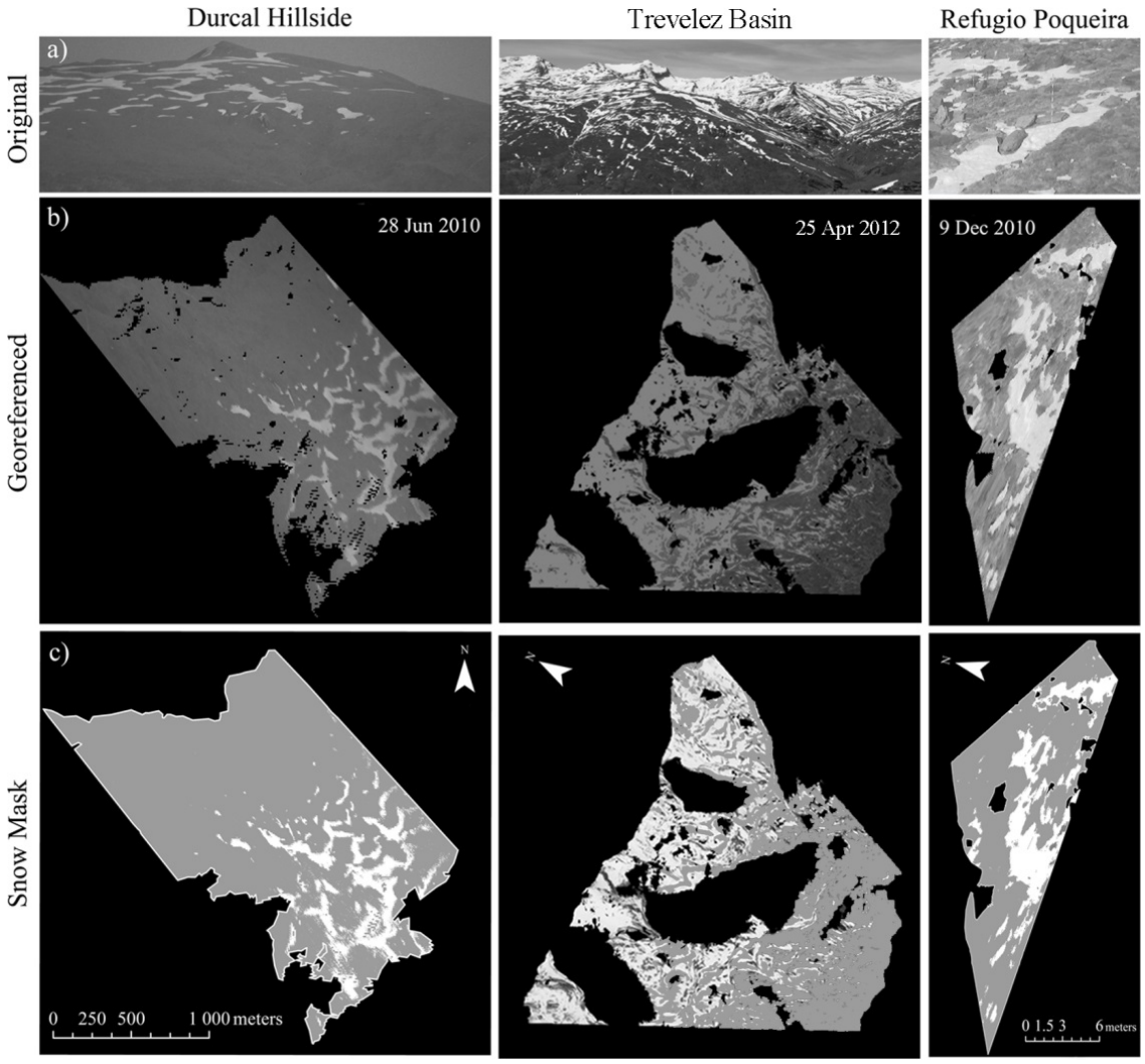


Figure A. 4 Selected examples of terrestrial photography processing: a) Original terrestrial images; b) Image Georeference; and c) Snow mask

## A.5. Conclusion

The use of terrestrial photography greatly improves the quality of snow cover evolution measurement and provides us with a deeper insight into the seasonal, weekly, and daily variability exhibited by snow processes in semiarid climates. This results in a sounder knowledge of the dynamics of such processes and their better further modeling at the watershed scale. The implemented GUI facilitates the automation of the georeference process in an easy way. It has also been evaluated under different spatial scales, showing a good accuracy in all the cases. Thus, the capability and versatility of terrestrial photography for easy and continuous monitoring of snow has been demonstrated from the results. Additionally, the different formats of output snow maps allow its inclusion in other software like ENVI or ARCGIS, frequently used in GIS-based applications.

# Appendix B: Graphic user interface to preprocess Landsat TM, ETM+ and OLI images for hydrological applications

*This work presents a graphic user interface (GUI), developed in MATLAB, which comprises all the preprocessing steps required to correct a Landsat TM, ETM+ and OLI. The only inputs required by the GUI are the metadata file of each Landsat image together with the digital elevation model (DEM) of the study area. The users can select among different preprocessing steps depending on their needs: (1) radiometric calibration, (2) atmospheric correction, (3) saturation problem and (4) topographic correction. The users can also choose the format of the output images (ascii ArcGIS, ascii ENVI and GEOTIFF) based on their final applications. This GUI allows faster results than other Landsat image preprocessing applications, due to the analysis of particular selected areas and the inclusion of a simple but accurate atmospheric correction.*

This chapter has been chapter has been presented as oral communication in HIC 2014-11th International Conference on Hydroinformatics:
Pimentel, R., Herrero, J. and M. J., Polo: Graphic user interface to preprocess Landsat TM, ETM+ and OLI images for hydrological applications.

## B.1. INTRODUCTION

Hydrological models, mainly those that are based on physical approaches and make their calculation in a distributed way, need distributed observation of the model state variables to calibrate and validate their GIS-based calculation. Satellite remote sensing techniques are a powerful tool for acquiring this information since they have the ability to measure hydrological variables (e.g. snow cover, water quality, land use and vegetation) and their evolution on spatial, spectral and temporal domains. In general, these techniques infer surface variables from measurements of the electromagnetic radiation of the land surface (Schmugge et al., 2002). Within the large amount of satellite remote sensing information (e.g. NOAA, daily images with 1 x 1 km cell size; MODIS, daily images with 250 x 250m cell size; Landsat, 16-day images with 30 x 30 m cell size), the selection of one or another is closely related to the scale of the processes studied. In semiarid regions, such as Mediterranean environments, the extreme variability of weather agents means that a high spatial resolution is needed to obtain an accurate representation of the hydrological process. Thus, Landsat imagery is usually employed over these areas (Pimentel et al., 2012; Pimentel et al., 2013). Besides, they currently offer the longest and most consistent historical archive of satellite data as they are able to capture large evolution changes (Wulder et al., 2008).

Landsat images (TM, ETM+ and OLI) require several levels of preprocessing: a) to obtain the reflectance values needed to calculate the diverse hydrological variables; b) to distinguish between the possible product artifacts and the true changes in the Earth processes; and c) to be able to compare acquired images on different dates under different acquisition conditions (Roy et al., 2002). This preprocessing is usually composed of both radiometric calibration and atmospheric correction. Stages where rescaling factors are needed to transform the encoded Digital Numbers (DNs) to absolute units of spectral radiance (Chander et al., 2009); and atmospheric effects that modify the radiation between sensor and surface, e.g. the scattering produced by water vapor and aerosol or the appearance of clouds are suppressed (Chavez et al., 1996; Liang et al., 2001). However, if the study area is on rough terrain, added difficulties

appear. In these cases, the changeable illumination conditions throughout the year produce topographic shade on the scene. Thus, a topographic correction is needed to equalize sunny and shaded areas (Hantson and Chuvieco, 2011). Moreover, saturation problems can appear over specific land surface cover, when the configuration of the sensor is not able to scan correctly and, thus, a saturation radiometric correction is needed. Therefore, four preprocessing steps could be required for a correct obtainment of reflectance values.

According to all these consideration the aim of this work is to develop an interactive tool, which includes the entire preprocessing steps required to obtain the reflectance value from Landsat TM, ETM+ and OLI and enable one to select between the different steps, since, depending on the study problem, not all these four stages are required: 1) Radiometric calibration; 2) Atmospheric correction; 3) Saturation Correction; and 4) Topographic correction.

### B.1.1. Material and methods

### Landsat images

Landsat program began in the early 1970`s and different missions with increased sensor technologies have been placed in orbit on board satellites. Within the different satellites, this study has been carried out to preprocess images coming from Landsat 4 (L4) and Landsat 5 (L5), which carry the Thematic Mapper (TM), Landsat 7 (L7), which includes the Enhanced Thematic Mapper Plus (ETM+) and Landsat 8 (L8) with the Operational Land Imager (OLI). presents different information about the Landsat satellites analyzed.

Table B.1. General information about each Landsat satellites analyzed

| Satellite | Sensor | Launch date | Decommission | Altitude (km) | Inclination (degrees) | Repeat cycle (days) |
|---|---|---|---|---|---|---|
| Landsat 4 | TM | July 16, 1982 | June 30, 2001 | 705 | 98.20 | 16 |
| Landsat 5 | TM | March 1, 1984 | January, 2013 | 705 | 98.20 | 16 |
| Landsat 7 | ETM+ | April 15, 1999 | Operational | 705 | 98.20 | 16 |
| Landsat 8 | OLI | February 11, 2013 | Operational | 705 | 98.20 | 16 |

Each image is composed of different band throughout the electromagnetic spectrum, whose denomination changes depending on the satellite studied. Only the bands located in the visible and near infrared areas of the spectrum are taken into account in this study.

### Preprocessing stages

Figure B.1 shows the different steps in the preprocessing of a Landsat image. As mentioned before, in certain cases not all the corrections are made. Radiometric calibration and atmospheric correction are always required, the former to obtain physical magnitude (radiance $Wm^{-2}sr^{-1}\mu m^{-1}$) of encoded photograph information and the latter to give a reflectance value free of atmospheric effects (range from 0 to 1). On the contrary, saturation and topographic correction are only needed when a land surface is saturated and when the mountainous terrain produces shadows on the scene. The following subsections describe each one of these processes.

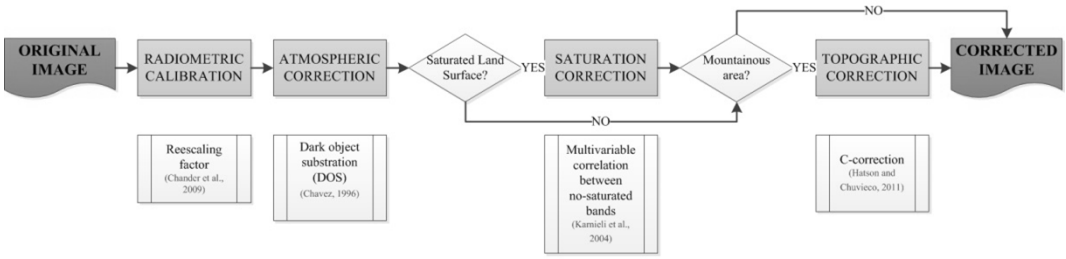


Figure B.1 Flow chart of the preprocessing stage of a Landsat image

### *Radiometric calibration*

This first obligatory stage consists of the transformation of calibrated digital number ($Q_{cal}$) of the Landsat images into absolute units of at-sensor spectral radiance ($L_\lambda$). Different rescaling factors depending on the band analyzed, sensor and configuration gain are required to obtain the radiance value (Chander et al., 2009). This information is available in the metadata file which goes with each Landsat image.

### *Atmospheric correction*

Electromagnetic radiation travels two ways through the atmosphere, from the sun to the land surface and from the latter to the satellite. While it travels, different processes, such as scattering and absorption by gases, aerosol and water vapor, modify its properties. Thus, the effects of these processes have to be removed in the analysis. Different methods of an increasing difficulty have been described in the literature to achieve this, from image-based procedures or dark-object subtraction (DOS), to radiative transfer codes (RTCs).

In this study, due to its objective of minimizing the number of inputs and the difficulty in finding available atmospheric data (e.g. type of aerosols, visibility of the atmosphere or content of water vapor), DOS was the technique applied. These methods are based on the assumption of all the scattering effects being the same as that of a blackbody on the scene (Moran et al., 1992). Some simplifications of the reflectance physic equation that relates the at-sensor radiance and the surface reflectance have also been considered (Chavez, 1988). Among these hypotheses are the assumptions of: a Lambertian surface, cloudless atmosphere, fixed values for the downwelling transmittance parameters (Gilabert at al., 1994) and neglected values for atmospheric transmittance and diffuse radiance.

### *Saturation correction*

To obtain better land-cover discrimination on each Landsat scene, the radiometric configuration of the satellite sensor changes depends on the main land-surface cover present on this scene. Different categories are defined: (1) land (non-desert, no-ice); (2) desert; (3) ice/snow; (4) water; (5) sea ice and (6) volcano/night. Occasionally, specific land surfaces constitute a very small area on the scene. In these cases sensor calibration is not the most adequate process and some radiometric-saturation problems may appear.

To correct this saturation, the assumption of a high correlation between spectral bands for snow has been adopted. Based on this hypothesis, a multivariable correlation analysis between bands is employed to recover the snow saturation pixels (Karnieli et al., 2004).

### *Topographic correction*

In mountain areas, the complex topography favors a variation in the reflectance response for similar land-cover types due to the difference between direct solar and non-solar illuminated areas. Therefore, a correction homogenizing these differences is necessary, which is the aim of topographic correction. In this study, a C-correction (Teillet et al., 1982) with land-cover separation algorithm was employed. This method assumes a Lambertian surface and establishes a linear fit between the illumination angle and the different band reflectances. Additionally, it takes into account the diffuse irradiance by a semi-empirical estimation of the C factor. In order to consider the multiple reflective properties of the different vegetative soil covers, the pixels were classified into bare soil and vegetated areas by using the Normalized Difference Vegetation Index (NDVI) (Moran et al., 1992).

## B.2. Graphic User Interface

The MATLAB tool for creating GUI was used to develop the application that includes all the pre-processing steps required to correct Landsat images. Figure B.1 shows the final interface, which allows user employment in an easy way. The GUI is divided into four areas: ZONE A, load area; ZONE B, preprocessing selection area; ZONE C, visualization area and ZONE D, save area.

The only inputs required for the GUI are a DEM of the study area and the metadata file of the Landsat scene. The inclusion of these files in the GUI is done by an interactive browser button (right ZONE A). These two files are required to select study area from the total Landsat scene and to apply the topography correction, and to obtain basic information about the Landsat scene (e.g. radiometric calibration coefficients, time of acquisition, solar parameters). The selection of the different preprocessing stages is done in ZONE B; the different buttons are consecutively activated following the flux chart shown in Figure B.2. A visualization of the selected area and some data of the Landsat scene (date and satellite studied) are shown in ZONE C. In ZONE D the user can select between different formats how to save the result of each correction. The selection of saved corrections is done by means of the activating the different check boxes located on the right of each correction. A final button to clear the inputs and change the images appears in the bottom right area.


Figure B.2 GUI tool for preprocessing Landsat images. Four zones can be distinguished: ZONE A, where the two inputs are loaded; ZONE B, area where the different preprocessing steps can be selected; ZONE C, where the selected area of the Landsat scene and some data are visualized; and ZONE D, area where the different output format can be selected.

## B.3. Application examples

Two application examples were used to test the Correction Landsat GUI. The first one corresponded to a very rough terrain, Sierra Nevada Mountain southern Spain, where topographic correction was needed to equalize sunny and shaded areas. The second one is an example in the same location area but, in this case, it aimed to evaluate the saturation correction. For that purpose, a small snow saturated area was analyzed before and after the application of the correction.

### B.3.1. Mountainous terrain

To evaluate topographic correction a Landsat scene in a mountainous area was selected. Figure B.3 shows the study area before and after the application of the topographic correction, in this case Band 4 is represented.

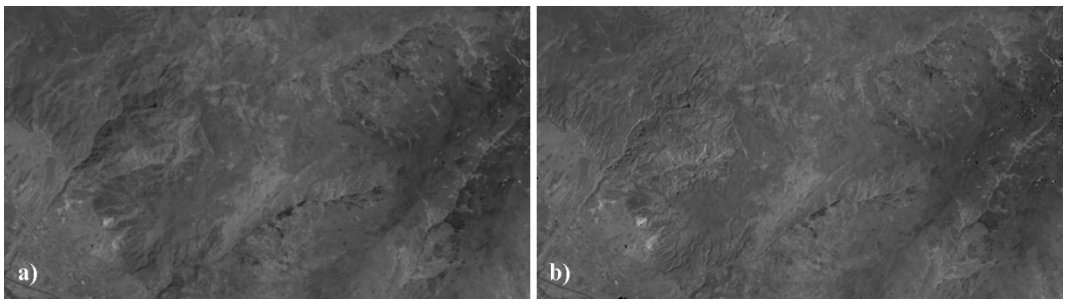


Figure B.3 Band 4 of Landsat scene of 2007/06/24 a) before and b) after topographic correction

In Figure B.3 a) shows some shadows in the terrain depending on the aspect of the hillsides, mainly on the left part. After the application of topographic correction these differences were

reduced, obtaining a more homogeneous terrain (Figure B.3 b). To account for this improvement basic statistics of the reflectance values were calculated in both cases (Table B. 1). The results show a negligible difference in maximum, minimum and mean values and a reduction in standard deviation, which shows the terrain to be less heterogeneous than before the correction.

Table B. 1 Statistic descriptors of the reflectance value before and after the application of saturation correction

| | a) Before topographic correction | b) After topographic correction |
|---|---|---|
| Maximum | 0.523 | 0.526 |
| Minimum | 0.019 | 0.017 |
| Mean | 0.195 | 0.207 |
| Standard Deviation | 0.060 | 0.045 |

### B.3.2. Snow saturation

To evaluate the saturation correction, a Landsat scene where snow constituted less than 5% and, thus, was not calibrated as snow images, was selected. A study area where snow appeared was selected. Table B. 2 shows the variation before and after the application of the saturation correction over Band 1 of the Landsat image.

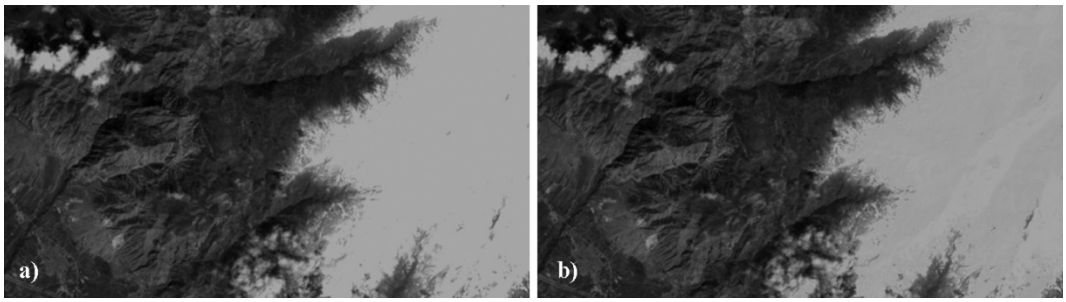


Figure B. 4 Band 1of Landsat scene of 2011/03/27 a) before and b) after saturation correction

In Table B. 2 a) it can be observed that all the snow pixels have a similar value (snow is saturated), after the application of the saturation correction (Figure B. 4 b) small differences appear over these pixels. To explain this improvement, basic statistics of the reflectance values of the snow pixels were calculated in both cases over snow area (Table B. 2). The larger value of standard deviation after the correction shows that the correction is correctly applied.

Table B. 2. Statistic descriptors of the reflectance value before and after the application of saturation correction

| | a) Before saturation correction | b) After saturation correction |
|---|---|---|
| Maximum | 0.526 | 0.530 |
| Minimum | 0.077 | 0.077 |
| Mean | 0.464 | 0.475 |
| Standard Deviation | 0.055 | 0.079 |

## B.4. Conclusion

This GUI is an easy tool for preprocessing Landsat images. Its computer-friendly environment enables a non-expert remote sensing user to easily correct Landsat images for hydrological uses. Moreover, it gives faster results than other Landsat preprocessing applications, since it means working only in particular selected areas and uses a more simple but accurate atmospheric correction. This is especially efficient when the atmospheric properties needed in a more complex model are unavailable. Further, it also includes the problematic of self-shadowing due to the rough terrain and saturation problems, which are not comprised in other specific software

where its implementation being necessary in each specific case. Finally, the different formats of output images permit their inclusion in other software such as ENVI or ARCGIS, which are frequently used in GIS-based applications. However, some initial hypotheses, such as cloudless skies, prevent cloudy images from being corrected with this GUI.

# Appendix C: Estimating snow albedo patterns in a Mediterranean site from Landsat TM and ETM+ images

*The albedo of snow affects the shortwave radiative flux at the land-atmosphere interface, so that it therefore plays an important role in the snow mass and energy balance. In semiarid areas, their particular climate conditions enhance the spatiotemporal variability of the snow albedo during the snow cover periods, increasing its difficulty in being measured and monitored. Satellite remote sensing is a powerful tool for measuring snow albedo evolution. Ten years of Landsat-5 and Landsat-7 Thematic Mapper images were analysed to determine a trend in the albedo evolution throughout the year in a Mediterranean site, Sierra Nevada Mountain (Southern Spain). A pattern in snow albedo from all snow pixel in each Landsat scene was obtained. It ranges from 0.8 in new snow to 0.4 in old dirty snow, with a decreasing rate of 0.003 albedo per day. This trend was validated with 5 specific location, where the snow is more persistent while the pixel remains well-illuminated.*

This chapter has been presented as oral communication in SPIE Remote Sensing, 2013 and published:

Pimentel R., Herrero J. and M. J. Polo, 2013: Estimating snow albedo patterns in a Mediterranean site from Landsat TM and ETM+ images, Proceedings, *Remote Sensing for Agriculture, Ecosystems, and Hydrology XVI*, Dresde, Germany, SPIE 8887.

## C.1. Introduction

Snow constitutes a basic component inside hydrological regime in mountain areas (Elder et al., 1991). This importance increases in Mediterranean locations, where water resources are particularly important to the development of these regions. Therefore, it is essential to know the behaviour and evolution of the snow layer, especially during the snowmelt phase when water becomes part of the total runoff. Because of the changeable weather condition of a Mediterranean climate, several snowmelt cycles can take place throughout the year. These variable characteristics do not allow the application of an empirical relation between atmospheric variables and snowmelt flux to predict snow evolution. Thus, the best way to reproduce this variability is by the use of an energy balance approach calibrated with local measurements, so that snow evolution can be modelled (Herrero et al., 2009).

Albedo plays in important role on the snow modelling since it affects the shortwave radiative flux (0.3-2.5 μm), quantifying the amount of solar radiation absorbed and reflected by the snowpack (Malik et al., 2011). Moreover, it is one of the main factors involved in the melt season due to the dominant importance of the radiation during these periods (Blösch, 1991; Dozier and Painter, 2004). Its importance is greater in these semiarid areas where the level of solar energy incomes throughout the year is very high (Aguilar et al., 2010).

Measuring and monitoring snow albedo present difficulties, which increase when the measurements are spatially distributed. Satellite remote sensing is the most extended technique used to monitor snow albedo, since this source captures the variability of snow albedo in each of the three domains: time, space and frequency (Dozier et al., 1981; Hall et al., 1995). However, these measurements are limited by the fixed resolution of satellite images (e.g. NOAA, daily images with 1x1 km cell size; MODIS, daily images with 250x250 m cell size; Landsat, 16-day images with 30x30 m cell size) and the spectral wavelength range, as each satellite takes information in certain bands of the electromagnetic spectrum. Moreover, some considerations that complicate the acquirement of snow albedo from remote sensing must be taken into

account. First there are the atmospheric effects between sensor and surface, such as the scattering produced by water vapour and aerosols or the presence of cloud cover that make it difficult to obtain information over the surface. Other added difficulties are the degree of anisotropy of the measured surface, which conditions the relation between the incident and reflected angle; and the narrowband to broadband conversion (Kimes et al., 1992: Liang, 2000). Besides these considerations, in Mediterranean mountain areas it is also important to consider the effects of the topography, which usually produces hard shadowing over the scene. Shaded areas show less reflectance than expected, whereas in sunny areas the effect is the opposite and, therefore the reflectance response from the same snow is different (Riaño et al., 2003).

According to all these consideration, Landsat TM and ETM+ are the most recommended images to study snow albedo evolution in a semiarid climate. Its extreme conditions favour a particular spatial distribution of the snow, which usually appears as small patches. So, the spatial dimension is the limiting factor; a bigger cell size would introduce areas not covered by snow and reduces the number of pure snow pixel (Pimentel et al., 2012). In this context ten years of these images in a Mediterranean mountain area in Southern Spain were analysed to estimate snow albedo patterns throughout the years. It facilitates the snow albedo integration in the modelling of the snow in a Mediterranean site.

## C.2. Study site

This study was carried out in Sierra Nevada Mountains, Southern Spain, with altitudes ranging from 1500 to 3500 m. They form a linear mountain range 60 km long, parallel to the shoreline of the Mediterranean Sea (Figure C.1). The mountain climate is modified by its proximity to the sea, only 35 km away, which generates semi-arid Mediterranean and tropical conditions in the surrounding area. Precipitation greatly fluctuates between years; it can range from 400 mm, in a dry year, to 1500 mm, in a wet year, and it is distributed heterogeneously over the area due to topography effects. The average temperature ranges from -5ºC to 5ºC during the snow season, which typically extends from December to June. The snow appears in altitudes of 2000 m and is characterized by those climate conditions. It has a strong spatiotemporal distribution, high evaporation rates and several snowmelt cycles during the snow (Herrero et al., 2011).

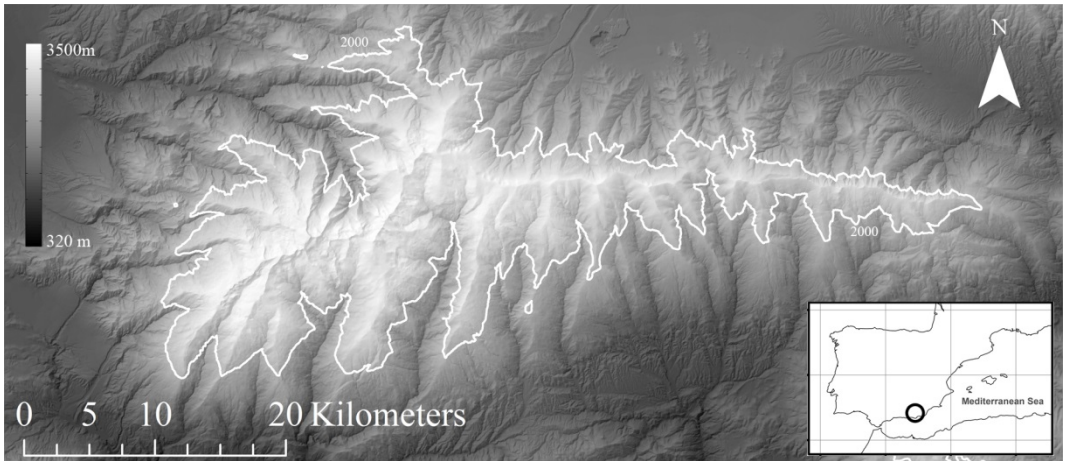


Figure C.1 Location of Sierra Nevada Mountain Range, Southern Spain

## C.3. MATERIAL AND METHODS

The data corresponding to ten water years, from 2000 to 2010, of Landsat Thematic Mapper (TM) and Enhanced Thematic Mapped Plus (+ETM) images, were analysed to study snow

albedo evolution. A total of 58 images were selected, which corresponded to cloudless days and with the presence of snow. Moreover, although from May of 2003, the ETM+ sensor did not record the images in the correct way, as the scan line corrector failed and several black lines appeared in these images constituting about 22% of the area recorded. This problem did not affect the centre of the scene, place where most of the study area is located. Table 5.1 shows the different dates selected and the sensor that capture each images (Landsat 5, TM or Landsat 7, ETM+).

| | Date | Sensor |
|---|---|---|
| 2000-2001 | 20/01/2001 | Landsat 7 +ETM |
| | 07/02/2001 | Landsat 7 +ETM |
| | 11/03/2001 | Landsat 7 +ETM |
| | 27/03/2001 | Landsat 7 +ETM |
| | 12/04/2001 | Landsat 7 +ETM |
| | 30/05/2001 | Landsat 7 +ETM |
| 2001-2002 | 25/01/2002 | Landsat 7 +ETM |
| | 26/02/2002 | Landsat 7 +ETM |
| | 01/05/2002 | Landsat 7 +ETM |
| | 02/06/2002 | Landsat 7 +ETM |
| | 10/06/2002 | Landsat 5 TM |
| 2002-2003 | 12/01/2003 | Landsat 7 +ETM |
| | 28/01/2003 | Landsat 7 +ETM |
| | 01/03/2003 | Landsat 7 +ETM |
| | 04/05/2003 | Landsat 7 +ETM |
| | 29/06/2002 | Landsat 5 TM |
| | 15/07/2003 | Landsat 5 TM |
| 2003-2004 | 14/12/2003 | Landsat 7 +ETM |
| | 03/03/2004 | Landsat 7 +ETM |
| | 23/06/2004 | Landsat 7 +ETM |
| | 09/07/2004 | Landsat 7 +ETM |
| 2004-2005 | 14/11/2004 | Landsat 7 +ETM |
| | 01/01/2005 | Landsat 7 +ETM |
| | 02/02/2005 | Landsat 7 +ETM |
| | 18/02/2005 | Landsat 7 +ETM |
| | 06/03/2005 | Landsat 7 +ETM |
| 2005-2006 | 17/11/2005 | Landsat 7 +ETM |

| | Date | Sensor |
|---|---|---|
| 2006-2007 | 12/11/2006 | Landsat 5 TM |
| | 30/12/2006 | Landsat 5 TM |
| | 07/01/2007 | Landsat 7 +ETM |
| | 16/02/2007 | Landsat 5 TM |
| | 12/03/2007 | Landsat 7 +ETM |
| | 20/03/2007 | Landsat 5 TM |
| | 07/05/2007 | Landsat 5 TM |
| | 15/05/2007 | Landsat 7 +ETM |
| | 24/06/2007 | Landsat 5 TM |
| 2007-2008 | 22/10/2007 | Landsat 7 +ETM |
| | 07/11/2007 | Landsat 7 +ETM |
| | 27/02/2008 | Landsat 7 +ETM |
| | 30/03/2008 | Landsat 7 +ETM |
| | 18/06/2008 | Landsat 7 +ETM |
| | 04/07/2008 | Landsat 7 +ETM |
| 2008-2009 | 25/11/2008 | Landsat 7 +ETM |
| | 11/12/2008 | Landsat 7 +ETM |
| | 12/01/2009 | Landsat 7 +ETM |
| | 13/02/2009 | Landsat 7 +ETM |
| | 17/03/2009 | Landsat 7 +ETM |
| | 04/05/2009 | Landsat 7 +ETM |
| | 29/06/2009 | Landsat 5 TM |
| 2009-2010 | 06/12/2009 | Landsat 5 TM |
| | 23/01/2010 | Landsat 5 TM |
| | 29/04/2010 | Landsat 5 TM |
| | 15/05/2010 | Landsat 5 TM |
| | 31/05/2010 | Landsat 5 TM |
| | 08/06/2010 | Landsat 7 +ETM |
| | 18/07/2010 | Landsat 5 TM |
| | 26/07/2010 | Landsat 7 +ETM |
| | 03/08/2010 | Landsat 5 TM |

Table 5.1. Analysed Landsat scenes

Several levels of preprocessing are required to obtain the snow albedo from the Landsat images. Generally, these steps include atmospheric correction, angular models that convert directional reflectance to spectral albedo, and narrowband to broadband conversion (Ranson et al., 1991; Liang et al., 2000). In this study, the surface is considered to be Lambertian, that is, the degree of anisotropy of the land surface is not considered and, therefore, the angular correction is not applied (Schepman-Strub et al., 2006). However other considerations have been taken into account, such as the problem of radiometric saturation or the shadows produced by the abrupt topography. Figure C.2 shows the preprocessing steps applied to each image.

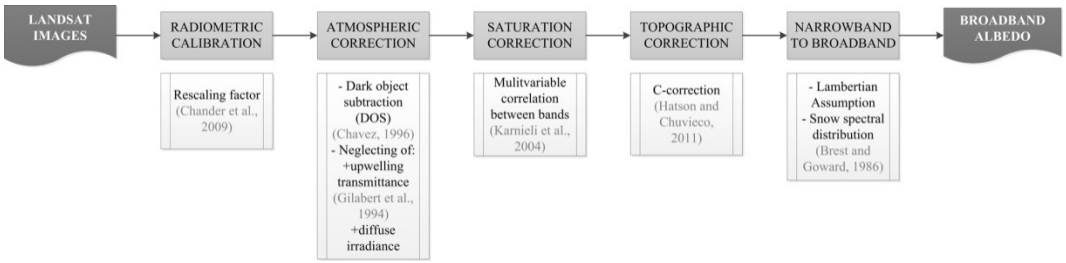


Figure C.2 Flow chart of the transformation of each Landsat scene into a map of snow albedo

### C.3.1. Radiometric Calibration

In this first step, the calibrated Digital Numbers ($Q_{cal}$) of the Landsat images are transformed into absolute units of at-sensor spectral radiance ($L_\lambda$). Conversion from $Q_{cal}$ back to $L_\lambda$ requires knowledge of the lower and upper limit of the original rescaling factor. The Equations and parameters to achieve this purpose are summarized by Chander et al. 2009 (Chander et al., 2009).

### C.3.2. Atmospheric Correction

The electromagnetic radiation measured by satellites is modified while travelling from the sun to the Earth's surface and from the Earth's surface to the sensor. The main processes that affect this radiation are scattering and absorption by gases, aerosol and water vapour. These effects must be removed from the analysed images. Several methods such as, radiative transfer codes (RTCs); image-base procedures; and dark-object subtraction (DOS), are described in the literature to achieve it (Kaufman and Sendra, 1988).

In this study, the DOS methods were used. They are simpler than RTCs, and when the necessary atmospheric data by RTCs are not available, they simplify the procedure with great accuracy. The DOS approach assumes different simplifications of the reflectance physic equation, which relate the at-satellite radiance and the surface reflectance (Chavez, 1988). This infers a Lambertian surface and a cloudless atmosphere. Moreover, this equation is simplified when supposing that all the scattering effects are the same as that a blackbody in the scene (Moran et al., 1992; Chavez, 1996), adopting fixed values for the downwelling transmittance parameters of the atmosphere for each band (Gilabert et al., 1994) and neglecting the upwelling atmospheric transmittance and the diffuse irradiance.

### C.3.3. Saturation Correction

To obtain a better land-cover discrimination in each Landsat scene, the radiometric configuration of the satellite sensor changes depends on the main land-surface cover present in this scene. Different categories are defined: (1) land (non-desert, no-ice); (2) desert; (3) ice/snow; (4) water; (5) sea ice and (6) volcano/night. Snow in the Landsat scene, where the study site is included, constitutes less of a 5 % in the maximum snow extension, and becomes insignificant at the end of the snow season. For this reason, the calibration of the sensor is not the most adequate for studying the snow and, therefore, several bands are radiometric-saturated. This saturation is greater in winter when the difference between snow and the rest of the cover in the scene is greater.

To correct this saturation, the assumption of a high correlation among between spectral bands for snow is adopted. Based on this hypothesis, a multivariable correlation analysis between bands is employed to recover the snow saturation pixels (Karnieli et al., 2004).

### C.3.4. Topographic Correction

In mountain areas, the complex topography favours a variation in the reflectance response for similar land-cover types due to the difference between direct solar and non-solar illuminated areas. Therefore, a correction that homogenizes these differences is necessary, which is the aim of the topographic correction. In this study, a C-correction (Teillet et al., 1982) with land-cover separation algorithm was employed. This method assumes a Lambertian surface and establishes a linear fit between the illumination angle and the different bands reflectance. Additionally, it takes into account the diffuse irradiance by a semi-empirical estimation of the C factor. In order to consider the multiple reflective properties of the different vegetative soil covers, the pixels were classified into bare soil and vegetated areas by using the Normalized Difference Vegetation Index (NDVI) (Hantson and Chuvieco, 2011).

## C.4. Broadband Albedo Obtainment

The spectral reflectances obtained must be integrated to produce a measurement of surface albedo. In this case, a Lambertian assumption was adopted, so that the degree of anisotropy was not considered and, consequently, the reflectance in each can be assimilated as narrowband. To achieve this integration it is essential to know the wavelength location of the narrow bands and the spectral reflectance of the surface analysed, i.e. snow.

### C.4.1. Snow detection

Because of the spectral reflectance differences between snow and snow-free areas, discrimination between them must be carried out. This is based on two different physical properties of the snow regarding its reflectance along the electromagnetic spectrum: 1) the very high snow albedo in the visible region and 2) the snow brightness temperature in the microwave region, which is significantly lower than that of snow-free ground because of volume scattering in the snowpack (Liang, 2000). Snow has a very high reflectance for wavelengths below of 0.8 μm, so it is easy to detect snow by fixing a threshold, which discriminates between cover and no-cover pixels. This technique presents the disadvantage of using only a single band, and it usually confuses snow with cloud cover since both have a similar response for wavelengths of below 1 μm. Thus, the use of a spectral band in the visible region plus one centred near 1.65, μm in the infrared where snow has a very low reflectance and the maximum difference with the clouds, is the most useful method (Riaño et al., 2003). Several ratios have been proposed to discriminate the snow by using two bands; the normalized difference snow index (NDSI) is mostly used (Pimentel et al., 2012). In this work, two thresholds were used to discriminate the snow, one for NDSI and another to Band 1 of the Landsat images. These thresholds were NDSI>0.4 and TM1>0.1 (Dozier, 1989; Herrero et al., 2011).

### C.4.2. Narrowband to broadband albedo

Both sensors analysed, TM and ETM+, have the same multispectral wavebands with a similar spectral coverage, so that all the images are processed in the same way. First, separation of the snow reflectance spectrum in several homogeneous parts is made, and then the assignation of a percentage of the total spectrum to each portion is calculated. Four portions are established: 0.3-0.725, 0.725-1.0, 1.0-1.4 and 1.4-4 μm (Brest and Goward, 1987). Band 2 represents the visible part of the spectrum (0.3-0.725). Band 4 is used to cover the two portions in the near-infrared (0.725-1.0) and (1.0-1.4); in this part the range is approximately 0.3 times less than the values for Band 4 (Dozier, 1989). And finally, Band 7 is employed in the rest of the spectrum (Figure C.3). The weighting function for snow surface is:

$$Albedo = 0.493 \cdot (Band\,2) + 0.203 \cdot (Band\,4) + 0.150 \cdot (0.3 \cdot (Band\,4)) + 0.154 \cdot (Band\,7) \quad (1)$$

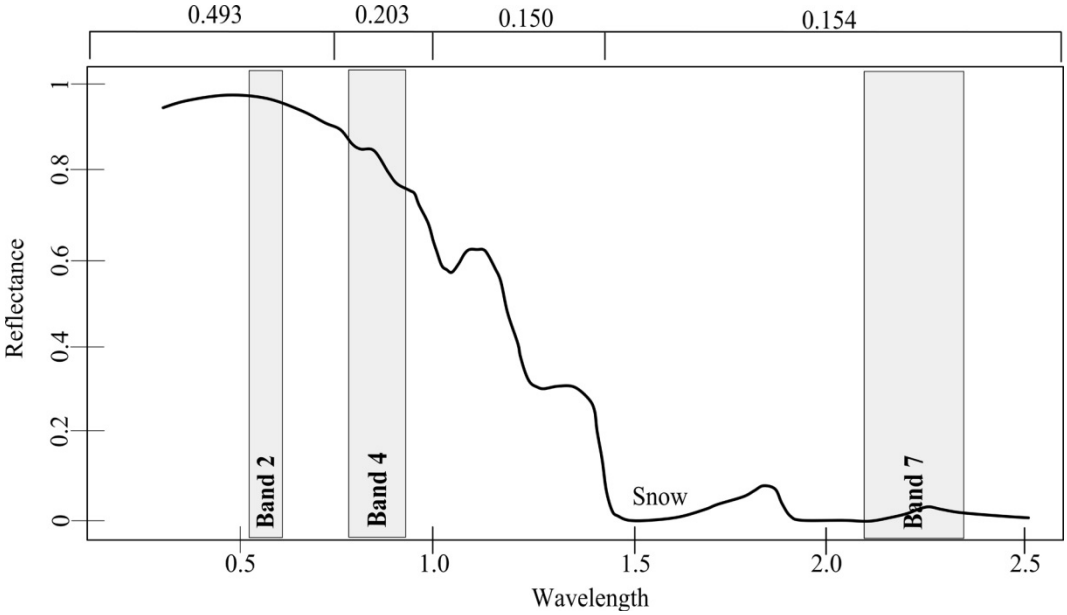


Figure C.3 Snow spectral reflectance

## C.5. RESULTS AND DISCUSSION

Snow albedo maps belonging to ten water years were obtained; Figure C.4 shows some of these maps where some anomalous snow albedo values appear. They are outside the normal snow albedo interval, which ranges from 0.40 to 0.85 for old dirty snow and fresh low density snow (Dingman, 2002). These values are mainly located in the perimeter of the area covered by snow (lower values) and in some higher point (upper values). The first ones correspond to pixels not completely covered by snow, whose albedo belongs to a mixed surface composed of snow and other soils. The second ones are pixels located in a particular place, where the topographic correction applied overestimates snow albedo.

Thus, it would be necessary to establish a rule to exclude these erroneous pixels in the study of trends and, therefore, to fix a maximum and minimum value representative of the snow albedo in this area. To study how the snow albedo values are distributed, cumulative density functions (cdf) for the value of albedo in each pixel of every image are represented. Figure C.5 shows these cdfs, which are grouped in two areas depending on the period of the year: (a) left side, where cdfs with a higher slope corresponding to images taken at the beginning and the end of the snow season (September, October and June, July and August) are located; and (b) right side, where cdfs represented have a lower slope belonging to the images taking in the middle of the snow season (November, December, January, February, March, April and May).

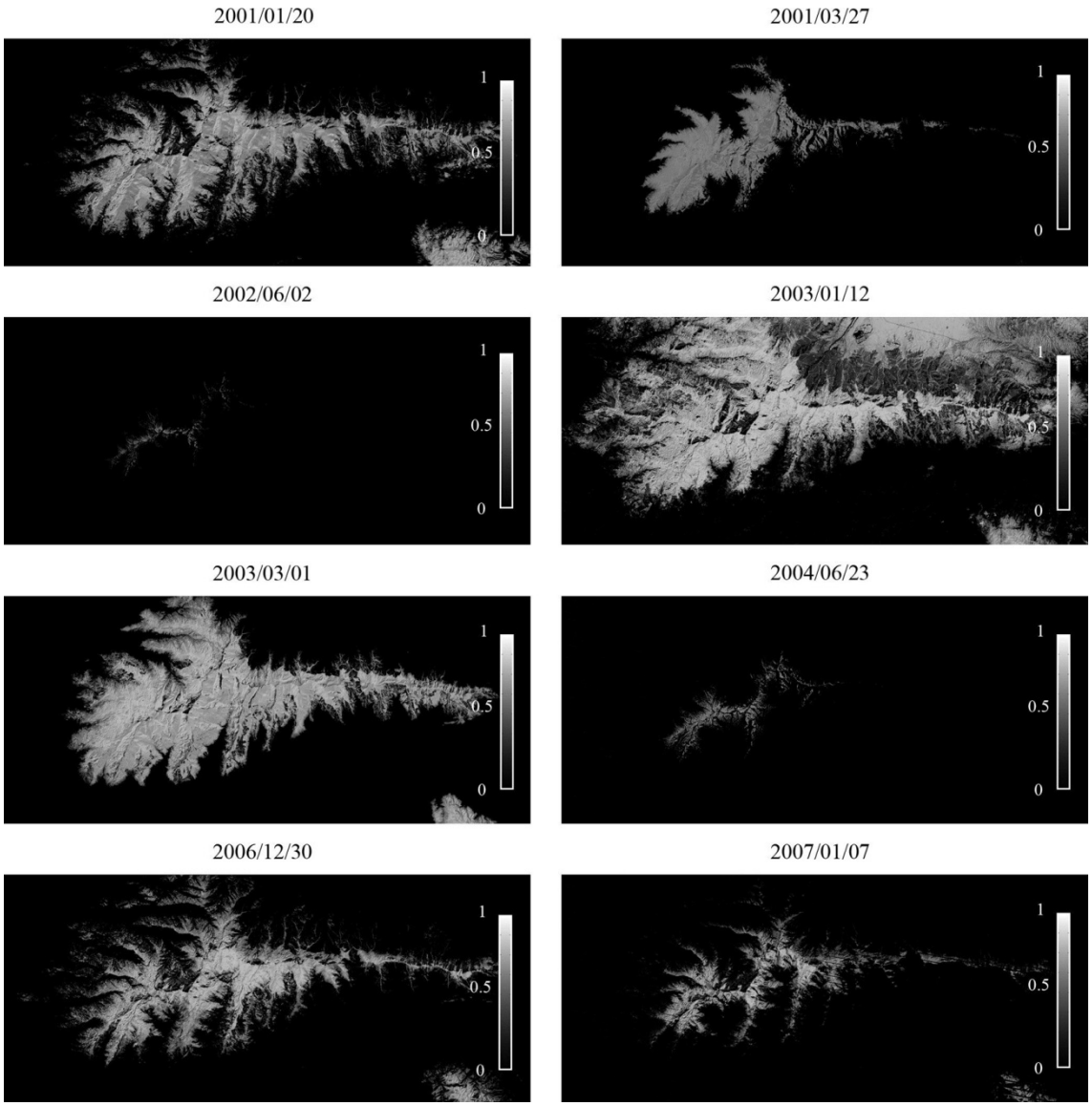


Figure C.4 Snow albedo maps from different period throughout the study period

That is, cdfs (a) represent periods with little snow, where the totally covered snow pixels are fewer, since most of them are mixed pixels. Therefore, a high percentile, of around 90$^{th}$, was selected to represent the minimum snow albedo of completely covered pixels. 99$^{th}$ percentile was selected to distinguish the maximum value for albedo, excluding higher values as they must be anomalous. In cdfs (b) the number of pixels totally covered by snow is greater and, therefore, 30$^{th}$ percentile is enough to detect pixels with an underestimated albedo value. As for the maximum value in cdfs (b), the 99$^{th}$ percentile is chosen, just like in the previous case. This selection rule was performed and different statistics were calculated using the remaining (Figure C.6).

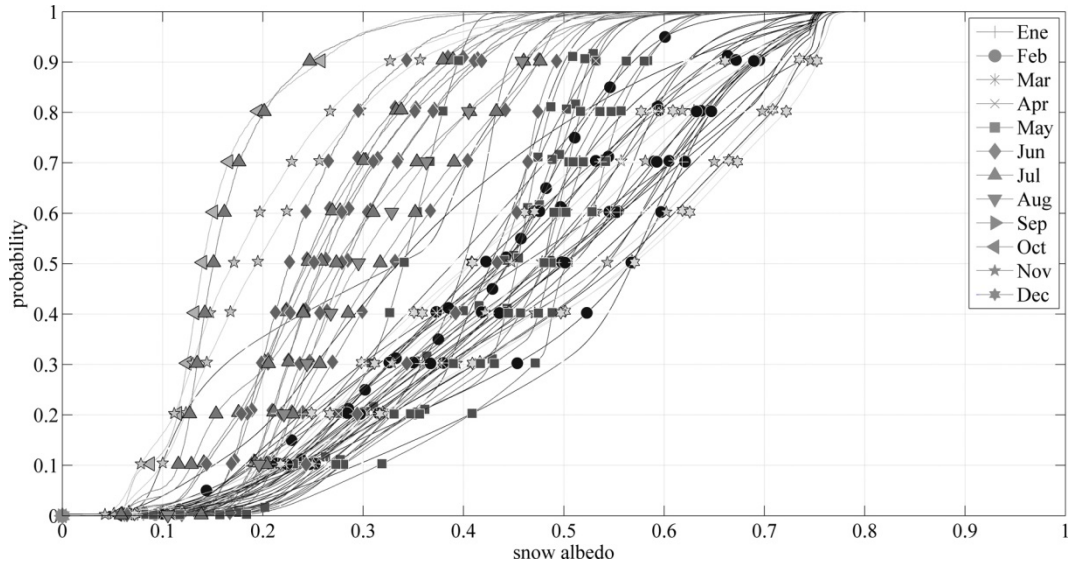


Figure C.5 Cumulative density function of each albedo map

A more realistic range is achieved with the selection of the pixels as described above. When assessing the values obtained, on one hand, the minimum values followed approximately the same trend throughout the year with a mean snow albedo value of 0.395. On the other hand, the trend of maximum values can be divided into two parts: a constant part, with a mean value of 0.799, from October to April; and a linear decreasing part from April to the end of the period, with a slope of -0.003 per day. Median values showed a similar trend as a maximum, but with lower values than expected, which were more homogeneous and close to the maximum values. This underestimation may be due to a bad execution of topographic correction, which does not homogenize the illuminated and non-illuminated zone, mainly during the autumn and winter, when the radiometric saturation is larger.

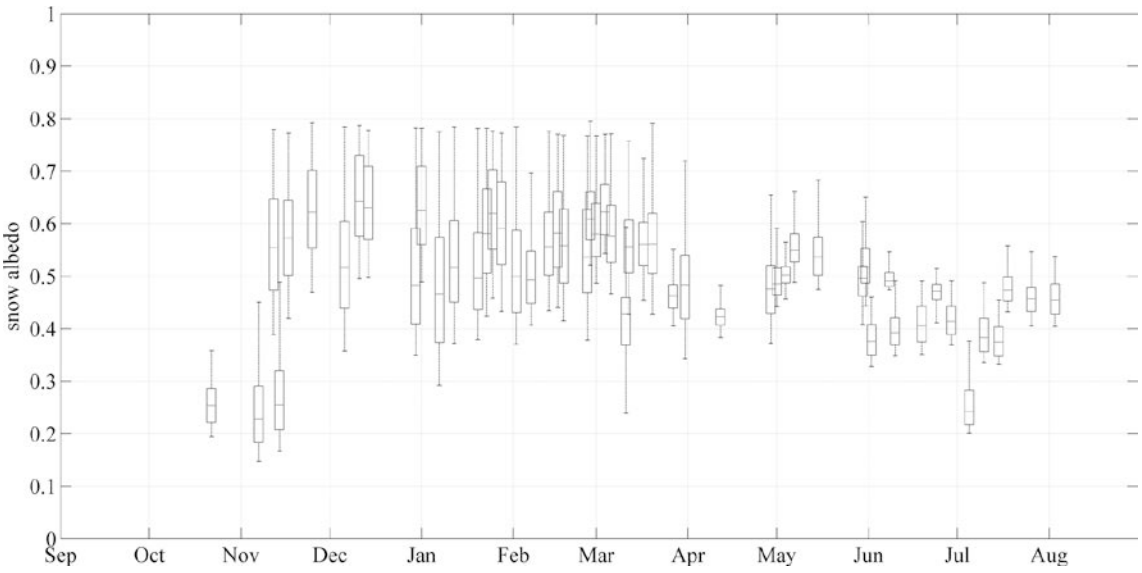


Figure C.6 Statistics of snow albedo maps throughout the year. Each box represents the statistics for the albedo of the pixel covered by snow in one single Landsat image. The central mark is the median, the edges of the box are the 25th and 75th percentiles, the whiskers extend to the most extreme maximum and minimum data points

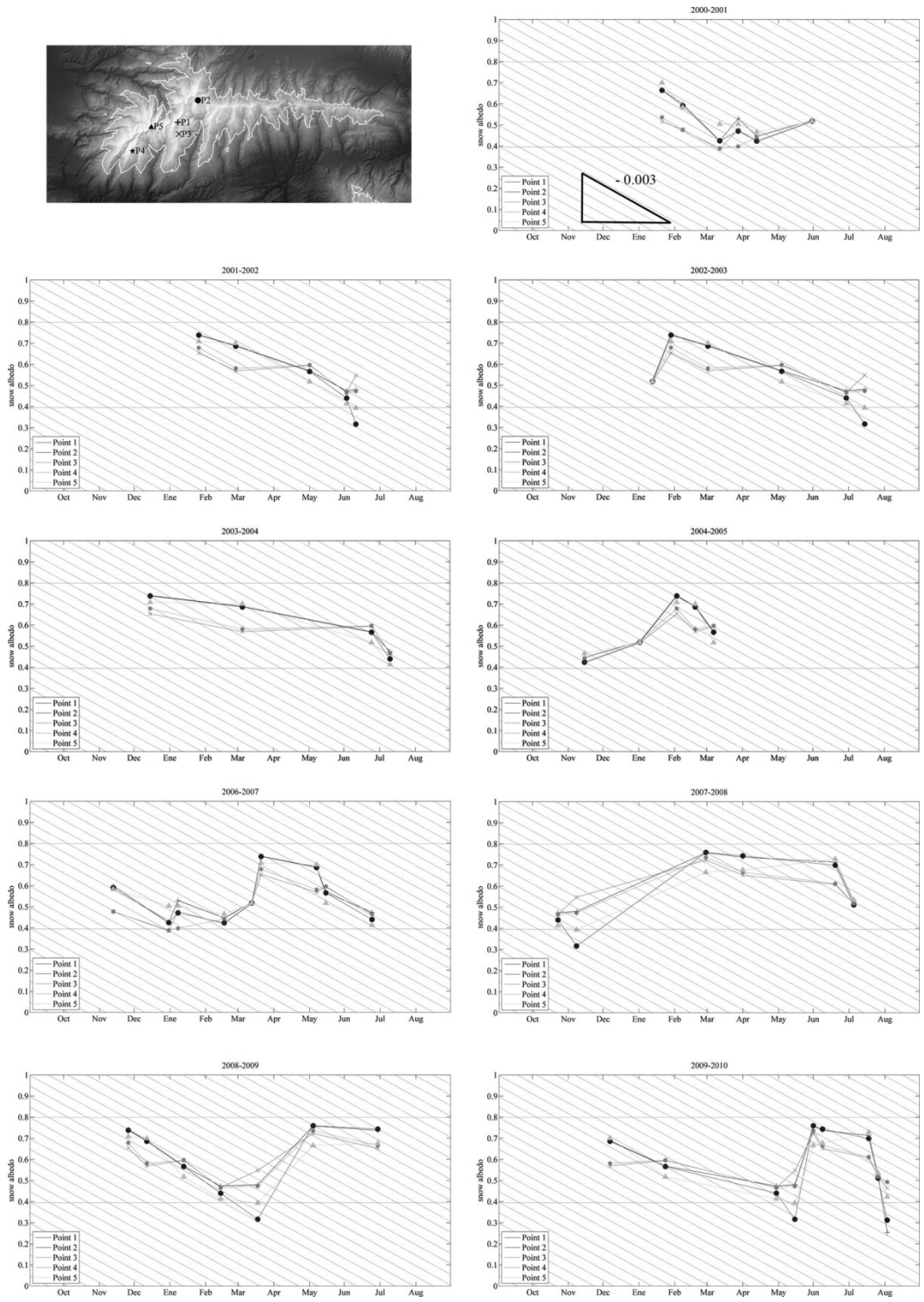


Figure C. 7 Snow albedo evolution throughout the study years in 5 selected locations (top-left pictures). The grid in each picture represents maximum, the minimum and the slope trend during melting season.

To verify the trend found in the maximum values, closer to the values proposed in the literature, five individual pixels located in areas where the snow stays longer were analyzed. For these pixels, a representation of snow albedo each year was made (Figure C. 7). All these snow albedo values ranged between the constant maximum and minimum values calculated. Moreover, in most of the year, the trend observed at the end of the snow season followed approximately the same trend as the maximum values (-0.003 per day). Some exceptions can be

observed in 2003-2004, 2007-2008 and 2009-2010. In 2003-2004 and 2007-2008, there were no snow maps between March and July. During these periods, some snow events took place so a maximum value must be represented between these dates, and, consequently, the trend was different. In 2009-2010 a strange snow event took place in June, as shown by the high snow albedo in the figure. Weather conditions in this period of the year facilitate a quicker melt, and for that reason the slope in the snow albedo evolution was greater and did not follow the trend.

Therefore, the pattern shown by maximum values appears to be more representative and realistic of the snow albedo evolution than other statistics values. Several problems shown by Landsat images in the study area and the particular snow distribution favour the appearance many values that distort the mean ones. An improvement in correction techniques must be included to obtain more realistic mean values.

## C.6. CONCLUSION

Landsat TM images are a powerful tool for measuring snow albedo distribution and its evolution. In mountainous areas such as Sierra Nevada, however, their use poses some constraints since their abrupt topography and the radiometric configuration of the sensors generate areas with hard illumination gradients and some radiometric saturation problems. The different methods applied to solve these problems resulted inadequate in obtaining snow albedo value in some specific period of the year. Some anomalies remained in given areas, mainly during the first stage of the snow season, with resulting reflectance values not being accurate enough. In addition to this, the particular snow cover distribution in this area, where snow-free patches are very frequent, favours a significant number of mixed pixels (made up of snow and other surfaces) in the Landsat images, which increases the number of snow albedo values rejected for the analysis.

The results in the snow-covered pixels finally accepted showed a maximum albedo value of around 0.8 for recent snow, which decreases following a stable rate of 0.003 per day. This trend is more realistic than those observed in the mean, which has lower values. A minimum value of 0.4 was also identified, associated with the oldest snow. The observed trends were validated with some selected pixels, where the presence of snow was confirmed from field observations. These results can be incorporated into physically based-distributed snowmelt models to study snow evolution in Mediterranean watersheds and other semiarid regions

# REFERENCES


Aguilar, C., Herrero, J. and M. J. Polo, 2010: Topographic effects on solar radiation distribution in mountainous watersheds and their influence on reference evapotranspiration estimates at watershed scale. *Hydrol. Earth Syst. Sci.,* **14,** 2479–2494.

Anderson, E. A., 1973. *National Weather Service River Forecast System-Snow Accumulation and Ablation model.* NOAA Technical Memorandum NWS HYDRO-17. Silver Spring, CO: US Dept of Commerce.

Anderson, E. A., 1976: *A point energy and mass balance model of snow cover*. Office of Hydrology, National Weather Service, NOAA Technical Report NWS 19.

Anderson, R. S., Jiménez-Moreno, G., Carrión, J. S. and C. Pérez-Martínez, 2011: Postgracial history of alpine vegetation, fire and climate from Laguna de Río Seco, Sierra Nevada, southern Spain. *Quaternary Sci. Rev.,* **30,** 1615-1629.

Anderton, S. P., White, S. M. and B., Alvera, 2004: Evaluation of spatial variability in snow water equivalent for a high mountain catchment. *Hydrol. Process.,* **18,** 435-453.

Andreadis, K. M., Storck, P. and D. P., Lettenmainer, 2009:Modeling snow accumulation and ablation processes in forested environments. *Water Resour. Res.,* **45,** 1275-1285.

Andreas, L., 1987: A theory for the scalar roughness and the scalar transfer coefficients over snow and sea ice. *Boundary-Layer Meteorol.,* **38,** 159–184.

Arola, A. and D. P. Lettenmaier, 1996: Effects of subgrid spatial heterogeneity on GMS-Scale land surface energy and moisture fluxes. *J. Climate,* **9,** 1339-1349.

Barnett, T. P., Adam, J. C. and Lettenmainer, D. P., 2005: Potential impacts of a warming climate on water availability in snow-dominated regions. *Nature,* **438,** 304-309.

Bartelt, P. B., and Lehning, M., 2002: A physical SNOWPACK model for avalanche warning services. Part I: numerical model. *Cold. Reg. Sci. Technol.,* **35,** 123-145.

Bavera, D., Bavay, M., Jonas, T., Lehning, M. and C. De Michele, 2014: A comparison between two statistical and a physically-based model in snow water equivalent mapping. *Adv. Water Resour.,* **63,** 167–178.

Beniston, M., 1997: Variations of snow depth and duration in the Swiss Alps over the last 50 years: links to changes in large-scale climatic forcing. *Climatic Change,* **36,** 281-300.

Beniston, M., Keller, F. and S. Goyette, 2003: Snow pack in the Swiss Alps under changing climate conditions: an empirical approach for climate impacts studies. *Theor. Appl. Climatol.,* **74,** 19-31.

Bishop, C. H., Etherton, B., and S. J. Majumdar, 2001: Adaptive sampling with ensemble transform Kalman filer. Part I: Theoretical aspects. *Mon. Wea. Rev.,* **129,** 420-436.

Blanca, G., 2002: *Flora amenazada y endémica de Sierra Nevada.* Consejería de Medio Ambiente, Junta de Andalucía, Granada.

Blöschl, G. and R. Kirnbauer, 1991: Point snowmelt models with different degrees of complexity – internal processes. *J. Hydrol.,* **129,** 127-147.

Blöschl, G., 1991: The influence of uncertainty in air temperature and albedo on snowmelt. *Nord. Hydrol.,* **22,** 95-108.

Blöschl, G., and M., Sivapalan, 1995: Scale issues in hydrological modelling – a review. *J. Hydrol.,* **9,** 251-290.

Blöschl, G., 1999: Scaling issues in snow hydrology. *Hydrol. Process.,* **13,** 2149-2175.

Blöschl, G., Kirnbauer, R. and D. Gutknecht, 1991: Distributed Snowmelt Simulations in an Alpine Catchment 1. Model Evaluation on the Basis of Snow Cover Patterns. *Water Resour. Res.,* **27,** 3171–3179.

Brest, C. and S. Goward, 1987: Deriving surface albedo measurements from narrow band satellite data. *Int. J. Remote Sens.,* **3,** 351-367.

Buttle, J. M. and J. J., McDonnell, 1987: Modeling the areal depletion of snowcover in a forested catchment, *J. Hydrol.,* **90,** 43-60.

Chander G., Markham B.L. and D. L. Helder, 2009: Summary of current radiometric calibration coefficients for Landsat MSS, TM, ETM+, and EO-1 ALI sensors, *Remote Sens. Environ.,* **113,** 893–903.

Chavez, P., 1996: Image-based atmospheric corrections-revisited and improved, *Photo. Eng. Remote Sens.,* **62,** 1025-1036.

Chavez, P., 1988: An improved dark-object subtraction technique for atmospheric scattering correction of multispectral data. *Remote Sens. Environ.,* **24,** 459–79.

Clark, M. P., Hendrikx, J., Slater, G., Kavetski, D., Anderson, B., Cullen, S. C., Kerr, T., Örn Hreinsson, E. and R. A., Woods, 2011: Representing spatial variability of snow water equivalent in land-surface models: A review. *Water Resour. Res.,* **47,** W07539.

Cline, D. W., 1997: Snow surface energy exchanges and snowmelt at a continental midlatitude Alpine site. *Water Resour. Res.,* **33,** 689-701.

Cline, D. W., Bales, R. G., and J. Dozier, 1998: Estimating the spatial distribution of snow in mountain basins using remote sensing and energy balance modeling. *Water Resour. Res.,* **34,** 1275-1285.

Cohn, S. E., 1997: An introduction to estimation theory. *J. Meteor. Soc. Japan,* **75,** 257-288.

Corripio, J. G., 2004: Snow surface albedo estimation using terrestrial photography. Int. *J. Remote Sens.,* **25,** 5705-5729.

Davis, R. E., McKenzie, J. C. and R. Jordan, 1995: Distributed snow process modelling: an image processing approach. *Hydrol. Process.,* **9,** 865-875.

Dadic, R., Mott, R., Lehning, M. and P., Burlando, 2010: Wind influence on snow depth distribution and accumulation over glacier. *J. Geophys. Res.,* **115,** F01012.

DeWalle, D. and A., Rango, 2008: *Principles of snow hydrology.* Cambridge University Press, 428 pp.

Dingman, L., 2002: *Physical Hydrology.* Prentice Hall, 600 pp.

Diodato, N., and G. Bellocchi, 2007: Modeling solar radiation over complex terrain using monthly climatological data. *Agr. Forest Meteorol,* **144,** 111-126.

Dozier, J. and T. H. Painter, 2004: Multispectral and hyperspectral remote sensing of alpine snow properties. *Annu. Rev. Earth Pl. Sc.,* **32,** 465-494.

Dozier, J., Schneider, S .R. and D. F. McGinnis, 1981: Effect of grain size and snowpack water equivalence on visible and near infrared satellite observations of snow. *Wat. Res. Res.,* **17,** 1213-1221.

Dozier, J., 1989: Spectral Signature of Alpine Snow Cover from the Landsat Thematic Mapper, *Remote Sens. Environ,* **22,** 9–22.

Dumur, D., Pilbeam, C. J., and J. Craigon, 1990: Use if the Weibull function to calculate cardinal temperatures in faba bean. *J. Exp. Bot.,* **41,** 1423-1430.

Egüen, M., Aguilar, C., Moreno, I., Herrero, J., Millares, A., Polo, M. J. and M. A., Losada, 2010: WiMMed a distributed physically based watershed model II: Application

examples. *Environmental Hydraulics. Theorical, experimental and computational solutions.*Taylor and Francis, 360 pp.

Elder, K., Dozier, J. and J. Michaelsen, 1991: Snow accumulation and distribution in an Alpine Watershed. *Wat. Res. Res.,* **27**, 1541-1552.

Essery, R., Li, L. and J. Pomeroy, 1999: A distributed model of blowing snow over complex terrain. *Hydrol. Process.,* **13,** 2423-2438.

Evensen, G., 1994: Sequential data assimilation with a nonlinear quasi-geostrophic model using Monte Carlo methods to forecast error statistics. *J. Geophys. Res.*, **99,** 1043-1062.

Farinotti., D., Magnusson, J., Huss, M. and A., Bauder, 2010: Snow accumulation distribution inferred from time-lapse photography and simple modeling. *Hydrol., Process.,* **24,** 2087-2097.

Ferguson, R. J., 1984: Magnitude and modeling of snowmelt runoff in the Cairngorm mountains, Scotland, *Hydrolog. Sci. J.,* **29,** 49-62.

Fiume, L., 1989: *The mathematical structure of raster graphics*, Academic Press Profesional, 221 pp.

Flerchinger, G.N., K.R. Cooley, and Deng, Y, 1994: Impacts of spatially and temporally varying snowmelt on subsurface flow in a mountainous watershed: 1. Snowmelt simulation. *Hydrologic Sci. J.,* **39,** 507-520.

Foley, J. D., van Dam, A., Feimer, S. K., and J. F. Hughes, 1990: *Computer graphics, principles and practice*, Addison-Wesley, 1175 pp.

Franz, K. J. and L. R. Karsten, 2013: Calibration of a distributed snow model using MODIS snow covered area data, *J. Hydrol.*, **494,** 160–175.

Garen, D. C. and D. Marks, 2005: Spatially distributed energy balance snowmelt modelling in a mountainous river basin: estimation of meteorological inputs and verification of model results. *J. Hydrol.*, **315,** 126–153.

Gilabert M.A., Conese C. and F. Maselli, 1994: An atmospheric correction method for the automatic retrieval of surface reflectances from TM images. *Int. J. Remote Sen.,* **15,** 2065–2086.

Goudriaan, J. and H. H., van Laar, 1994. *Modeling potential crop growth processes.* Kluver Academic Publishers, 114 pp.

Green, R. J., Fred, U. P., and W. P. Norbert, 1900: Things that go bump in the night. *Psych. Today,* **46,** 345-678.

Grody, N. C. and A. N., Basist, 1996: Global identification of snow cover using SSM/I instruments. *IEEE Trans. Geosci. Remote Sens.,* **34,** 237-249.

Hall, D. K., Riggs, G. A. and V. V. Salomonson, 1995: Development of methods for mapping global snow cover using moderate resolution imaging spectroradiometer data. *Remote Sens. Environ.,* **54,** 127-140.

Hantson S. and E. Chuvieco, 2011: Evaluation of different topographic correction methods for Landsat imagery, *Int. J. Appl. Earth Obs.*, **13,** 691-700.

Herrero, J., and M. J., Polo, 2012: Parameterization of atmospheric longwave emissivity in a mountainous site for all sky conditions. *Hydrol. Earth Syst. Sc.*, **16,** 3139-3147.

Herrero J., Polo M. J. and M. A. Losada, 2011: Snow evolution in Sierra Nevada (Spain) from an energy balance model validated with Landsat TM data. Proceedings, *Remote Sensing for Agriculture, Ecosystems, and Hydrology XIV*, Pragha, Czech Republic, SPIE 8531.

Herrero, J., Aguilar, C., Millares, A., Moñino, A., Polo, M. J. and Losada M. A., 2011: Mediterranean high mountain meteorology from continuous data obtained by a

permanent meteorological station at Sierra Nevada, Spain. *Geophys. Res. Abstr. EGU 13*, 12893.

Herrero, J., Aguilar, C., Polo, M. J. and M. A., Losada, 2010: Mapping of meteorological variables for runoff generation forecast in distributed hydrological modeling. Proceeding, *Hydraulic Measurements & Experimental Methods Conference*, New York, 606–611.

Herrero, J., Polo, M. J., Moñino, A. and M. A. Losada, 2009: An energy balance snowmelt model in a Mediterranean site, *J. Hydrol.*, **371**, 98–107.

Heywood, V. H., 1995: The Mediterranean flora in the context of world biodiversity. *Ecología Mediterránea,* **21,** 11-18.

James, K., Harris, Jr., G. and W. Wollops, 1976: American independence and magnetism, *Revol. Tracts,* **32,** 34-55.

Jordan, R. E., Andreas, E. L., and A. P. Makshtas, 1999: Heat budget of snow-covered sea ice at North Pole 4. *J. Geophys. Res.*, **104,** 7785-7806.

Jordan, R., 1991. *A one-dimensional temperature model for a snow cover*. US Army Corps of Engineers, Cold Region Research & Engineers Laboratory. Technical documentation for SNTERERM.89, Special Report 91-16.

Kalman, R. E., 1960: A New Approach to Linear Filtering and Prediction Problems. *J. Basic Eng.-T. ASME,* **82,** 35-45.

Karnieli, A., Ben-Dor, E., Bayarjargal, Y. and R. Lugasi, 2004: Radiometric saturation of Landsat-7 ETM+ data over the Negev Desert (Israel): problems and solutions. *Int. J. Appl. Earth Obs. Geoinf.,* **5,** 219–237.

Kaufman, Y. J. and C. Sendra, 1988: Algorithm for automatic atmospheric corrections to visible and near-IR satellite imagery. *Int. J. Remote Sens.,* **9,** 1357-1381.

Kirnnauer, R., Blöschl, G., and D. Gutknecht, D., 1994: Entering the era of distributed snow models. *Nord. Hydrol.,* **25,** 1-24.

Kim, J., and M. Ek, 1995: A simulation of the long-term surface energy budget and soil water content over the HAPEX-MOBILHY forest site, *J. Geophys. Res.,* **20,** 845-854.

Kimes, D. S. and B. N. Holben, 1992: Extracting spectral albedo from NOAA-0 AVHRR multiple view data using an atmospheric correction procedure and an expert system. *Int. J. Remote Sens.,* **13,** 275-289.

Kolberg, S. A., and L. Gottschalk, 2006: Updating of snow depletion curve with remote sensing data. *Hydrol. Process.,* **20,** 2363-2380.

Konz, M., Finger, D., Bürgi, C., Normand, S. and W. W. Immerzeel, 2010: Calibration of a distributed hydrological model for simulations of remote glacierized Himalayan catchments using MODIS snow cover data, *IGBP Report*, 465–473.

Kuchment, L. S., and A. N. Gelfan, 1996: The determination of the snowmelt rate and the meltwater outflow from a snowpack for modeling river runoff generation. *J. Hydrol.*, **179,** 23–36.

Kustas, W. P., Rango, A., and R. Uijlenhoet, 1994: A simple energy budget algorithm for the snowmelt runoff model. *Water Resour. Res.,* **30,** 1515-1527.

Kuusisto, E., 1986: The energy balance of a melting snow cover in different environments. Proceeding, *Modeling Snowmelt-Induced Processes*, Budapest, IAHS, 155.

Lapena, D. R. and L. W., Martz, 1996: An investigation of the spatil association between snow depth and topography in a Prairie agricultural landscape using digital terrain analysis. *J. Hydrol.*, **184,** 277-298.

Lehning, M., Bartelt, P. B., Brown, R. L., Fierz, C., and Satyawali, P., 2002: A physical SNOWPACK model for the Swiss Avalanche Warning Services. Part II: snow microstructure. *Cold. Reg. Sci. Technol.*, **35,** 147-167.

Liang S., Fang H. and M. Chen, 2001: Atmospheric correction of Landsat ETM+ land surface imagery – Part I: Methods, *IEEE Transactions on Geoscience and Remote Sensing*, **39,** 2490-2498.

Liang, S., 2000: Narrowband to broadband conversions of land surface albedo I Algorithms. *Remote Sens. Environ.,* **76,** 213-238.

Liang, S., Stroeve, J., Grant, I., Strahler, A. and J., Duvel, 2000: Angular correction to satellite data for estimating earth's radiation budget. *Remote Sens. Rew.*, **18,** 103-116 (2000).

Lindstrom, G., Johansson, B., Persson, M., Gardelin, M., and Bergstrom S., 1997: Development and test of the distributed HBV-96 hydrological model. *J. Hydrol.*, **201,** 272-288.

Liston, G. E. and Sturm, M., 1998: Asnow transport model for complex terrain. *J. Glaciol.,* **44,** 498-516.

Liston, G. E., Pielke, R. A., and E.M. Greene, 1999: Improving first-order snow-related deficiencies in a regional climate model. *J. Geophys. Res.*, **104,** 19559-19567.

Liston, G. E., 2004: Representing subgrid snow cover heterogeneities in regional and global models. *J. Climate,* **17,** 1381-1397.

Loth. B., Graf, H. F., and Oberhuber, J. M., 1993: Snow cover model for global climate simulation. *J. Geophys. Res.*, **98,** 10451-10464.

Luce, C. H., and D. G. Tarboton, 2004: The application of depletion curves for parameterization of subgrid variability of snow. *Hydrol. Process.*, **18,** 1409-1422.

Luce, C. H., Tarboton, D. G., and K. R. Cooley, 1999: Sub-grid parameteriztion of snow distribution for an energy and mass balance snow cover model. *Hydrol. Process.,* **13,** 1921-1933.

Luce, C. H., Tarboton, D. G. and K. R. Cooley, 1997: Spatially distributed snowmelt inputs to a semi-arid mountain watershed. *Proceeding of the Western Snow Conference,* Banff, Canada.

MacQueen, J. B., 1967: Some methods for classification and analysis of multivariate observations. Proceeding, *Fifth Symposium on Math, Statistics, and Probability,* Berkeley, CA, 281-297.

Malik, M. J., van der Velde, R., Vekerdy, Z. and Z. Su, 2012: Assimilation of Satellite-Observed Snow Albedo in a Land Surface Model. *J. Hydrometeor.,* **13,** 1119–1130.

Malik, M. J., van der Velde, R., Vekerdy, Z. and Z., Su, 2014: Improving modeled snow albedo estimates during the spring melting season, *J. Geophys. Res. Atmos.*, **119,** 1-21.

Malik, M. J., van der Velde, R., Vekerdy, Z., Su, Z. and M. F., Salman, 2011: Semi-empirical approach for estimating broadband albedo of snow. *Remote Sens. Environ.*, **115,** 2086-2095.

Mabuchi, K., Sato, Y., Kida., H., Saigusa, N., and T. Oikawa, 1997: A biosphere-atmosphere interaction model (BAIM) and its primary verifications using grassland data. *Papers Meteorol. Geophys.*, **47,** 115-140.

Marks, D., Winstral, A., Flerchinger, G., Reba, M., Pomeroy, L., Link, T. and K. Elder, 2008: Comparing simulated and measured sensible and latent heat fluxes over snow under a pine canopy to improve an energy balance snowmelt model. *J. Hydrometeor.,* **9,** 1506–1522.

Marks, D. and A., Winstral, 2001: Comparison of Snow Deposition , the Snow Cover Energy Balance, and Snowmelt at Two Sites in a Semiarid Mountain Basin, *J. Hydrometeorol.*, **2,** 213–227.

Marks, D., Domingo, J., Susong, D., Link, T. and D. Garen, 1999: A spatially distributed energy balance snowmelt model for application in mountain basins. *Hydrol. Proc,* **23,** 1935-1959.

Marks, D. and J. Dozier, 1992: Climate and energy exchange at the snow surface in the alpine region of Sierra Nevada. 2 Snow cover energy balance. *Water Resour. Res.,* **28,** 3043-3054.

Meromy, L., Molotch, N. P., Link, T. E., Fassnacht, R. and R. Rice, 2013: Subgrid variability of snow water equivalent at operational snow stations in the western USA. *Hydrol. Process.,* **27,** 2383-2400.

Molotch, N. P. and R. C., Bales, 2005: Scaling snow observation from the point to the grid element: Implications for the observation network design. *Water. Resour. Res.,* **41,** W11421.

Moran, M. S., Jackson, R. D., Slater, P. N. and P. M. Teiuet, 1992: Evaluation of Simplified Procedures for Retrieval of Land Surface Reflectance Factors from Satellite Sensor Output. *Rem. Sens of Env.,* **184,** 169–184.

Niu, G.-Y., and Z.-L. Yang, 2007: An observation-based formulation of snow cover fraction and its evaluation over large North American river basins. *J. Geophys. Res.,* **112,** D21101.

Nolin, A. and J. Dozier, 2000: A hyperspectral method for remotely sensing the grain size of snow. *Remote Sens. Environ.,* **216,** 207–216.

Obled, C. and H. Harder, 1979: A review of snow melt in the mountain environment. *Proceeding, Modelling of Snow Cover Runoff,* Hanover, New Hampshire, US Army Cold Regions Research and Engineering Laboratory, 179-204.

Ott, E., Hunt, B. R., Szunyogh, I., Zimin, A. V., Kostelich, E. J. and co-authors, 2004. A local ensemble Kalman filter for atmospheric data assimilation. *Tellus,* **56A,** 415-428.

Painter, T. H., Rittger, K., Mckenzie, C., Slaughter, P., Davis, R. E., and J., Dozier, 2009: Retrieval of subpixel snow covered area, grain size, and albedo from MODIS. *Remote Sens. Environ.,* **113,** 868-879.

Parajka, J. and G. Blöschl, 2008: The value of MODIS snow cover data in validating and calibrating conceptual hydrologic models. *J. Hydrol.,* **358,** 240–258.

Pham, D., 2001: Stochastic methods for sequential data assimilation in strongly nonlinear systems. *Mon. Wea. Rev.,* **129,** 1194-1207.

Pérez – Palazón, M. J., Pimentel, R., Herrero, J. and M. J. Polo, 2014: Terrestrial photography as an alternative to satellite images to study snow cover evolution at hillslope scale. Proceeding, *Remote Sensing for Agriculture, Ecosystems, and Hydrology XIV,* Edimburgh, SPIE. Remote Sensing, 8531.

Pimentel, R., Herrero, J., Zeng, Y., Su, Z. and M. J., Polo, 2014: Study snow dynamics at subgrid scale in semiarid environment combining terrestrial photography data assimilation techniques. *J. Hydrometeorol. (in press)*

Pimentel, R., Herrero, J. and Polo, M. J., 2014: Snow in a semiarid mountainous area combining snow modelling and Landsat spectral mixture analysis. Proceeding RSHS14 and ICGRHWE14, Guangzhou, China.

Pimentel, R., Herrero, J. and Polo, M. J., 2014: Graphic user interface to preprocess Landsat TM, ETM+ and OLI images for hydrological applications. Proceeding HIC 2014, 11th International Conference on Hydroinformatics, New York City, USA.

Pimentel, R., Pérez-Palazón, M. J., Herrero, J. and Polo, M. J., 2014: Monitoring snow cover area in a semiarid regions using terrestrial photography. Proceeding HIC 2014, 11th International Conference on Hydroinformatics, New York City, USA.

Pimentel R., Herrero J. and M. J. Polo, 2013: Estimating snow albedo patterns in a Mediterranean site from Landsat TM and ETM+ images, Proceedings, *Remote Sensing for Agriculture, Ecosystems, and Hydrology XVI*, Dresde, Germany, SPIE 8887.

Pimentel, R., Herrero, J. and M. J. Polo, 2012: Terrestrial photography as an alternative to satellite images to study snow cover evolution at hillslope scale. Proceeding, *Remote Sensing for Agriculture, Ecosystems, and Hydrology XIV*, Edimburgh, SPIE. Remote Sensing, 8531.

Polo, M. J., Herrero, J., Aguilar, C., Millares, A., Moñino, A., Nieto, S. and M. A. Losada, 2010: WiMMed a distributed physically based watershed model I: Description and validation. *Environmental Hydraulics. Theorical, experimental and computational solutions.*Taylor and Francis, 360 pp.

Rango A. and K. L. Itten, 1976: Satellite potentials in snowcover monitoring and runoff prediction, *Nordic Hydrol.,* **7,** 209-230.

Ranson, K. J., Irons, J. R. and C. S. T. Daughtry, 1991: Surface albedo from bidirectional reflectance. *Remote Sens. Environ.,* **35,** 201-211.

Reichle, R. H., 2008: Data assimilation methods in the Earth sciences, *Adv. Water Resour.,* **31,** 1411-1418.

Riaño, d., Chuvieco, E., Salas, J. and I. Aguado, 2003: Assessment of Different Topographic Corrections in Landsat-TM Data for Mapping Vegetation Types. *IEEE T. Geosci. Remote,* **41,** 1056-1061.

Richards, F. J., 1959: A flexible growth function for empirical use. *J. Exp. Bot.,* **10,** 290-300.

Rivera, A., Corripio, J. G., Brock, B., Clavero, J., and J. Wendt, 2008: Monitoring ice capped active VolcánVillarrica in Southern Chile by mean of terrestrial photography combined with automatic weather stations and GPS. *J. Glaciol.,* **54,** 920-930.

Roeckerner, E., Arpe, K., Bengtsson, L., et al., 1996: *The atmospheric Circulation Model ECHAM-4: Model Description and Simulation of Present-day Climate.* MPI-Rep. 218, MPI Für Meteorologie, Hamburg.

Roesch, A., and E. Roeckner, 2006: Assessment of snow cover andm surface albedo in the ECHAM5 general circulation model. *J. Climate,* **19,** 3828–3843.

Rosenthal, W. and J. Dozier, 1996: Automated mapping of montane snow cover at subpixel resolution from the Landsat Thematic Mapper, *Water Resour. Res.,* **32,** 115-130.

Roy D.P., Borak J.S., Devadiga S., Wolfe R.E., Zheng M. and J. Descloitres, 2002: The MODIS Land product quality assessment approach. *Remote Sens. Environ.,* **83,** 62–76.

Sade, R., Rimmer, A., Litaor, M. I., Shamir, E., and A., Furman, 2014: Snow surface energy and mass balance in a warm temperate climate mountain. *J. Hydrol.,* **519,** 848-862.

Sakov, P., and P. R., Oke, 2008: Implications of the form of the ensemble transformation in the ensemble square root filters. *Mon. Wea. Rev.,* **136,** 1042-1052.

Sakov, P., Evensen, G., and L. Bertino, 2009: Asynchronous data assimilation with the EnKF. *Tellus,* **62A,** 24-29.

Schaepman-Strub, G., Schaepman, M. E., Painter, T. H., Dangel, S. and Martonchik, J. V., "Reflectance quanties in optical remote sensing – definitions and case studies" Remote Sens. Environ. 103, 27-42 (2006).

Schmugge, T. J., Kustas, W. P., Ritchie, J. C., Jackson, T. J. and A. Rango, 2002: Remote sensing in hydrology. *Adv. Water Resour.*, **25,** 1367–1385.

Schulz, O., and C., de Jong, 2004: Snowmelt and sublimation: field experiments and modelling in the high Atlas Mountains of Moroco. *Hydrol. Earth Syst, Sci.*, **8,** 1076-1089.

Shmakin, A. B., 1998: The updated version of SPONSOR land surface scheme: PILPS-influenced improvements. *Gobal Planet. Change*, **19,** 49-62.

Smagorinsky, J., 1974: Global atmospheric modeling and the numerical simulation of climate. *Weather and Climate Modification*, HessWN, John Wiley & Sons, New York, 633-686.

Smirnova, T. G., Brown, J. M., and Benjamin, S. G., 1997: Performance of different soil model configurations in simulating ground surface temperature and surface fluxes. *Mon. Wea. Rev.*, **125,** 216-261.

Sorman, A. A., Sensoy, A., Teleki, A. E., Sorman, A. U. and Z. Akyurek, 2009: Modelling and forecasting snowmelt runoff process using the HBV model in the eastern part of Turkey. Proceeding, *Hydro.*, 1031-1040.

Tarboton, D. G. and C. H. Luce, 1996. *Utah Energy Balance Snow Accumulation Melt Model (UEB), Computer Model Technical Description and User Guide.* Utah Water Research Laboratory and USDA Forest Service Intermountain Research Station.

Tarboton, D. G., Chowdhury, T. G. and T. H. Jackson, 1994: A Spatially Distributed Energy Balance Snowmelt Model. Proceeding, *Symp. Biogeochem. Seas. Snow*, 1523-1535.

Teillet, P.M., Guindon, B. and D. G. Goodenough, 1982: On the slope-aspect correction of multispectral scanner data. *Canadian J. Remote Sens.*, **8,** 84-10.

Tippett, M. K., Anderson, J. L., Bishop, C. H., Hamill, T. M., and J. S., Whitaker, 2003: Ensemble Square Root Filters. *Mon. Weather Rev.*, **131,** 1485-1490.

Verhulst, P. F., 1838: A note on population growth. *Coorespondence Mathematiques et Physiques*, **10,** 290-300.

Wang, Z., Schaaf, C. B., Strahler, A. H., Chopping, M. J., Román, M. O., Shuai, Y., Woodcock, C. E., Hollinger, D. Y. and D. R., Fitzjarrald, 2014: Evaluation of MODIS albedo product (MCD43A) over grassland agriculture and forest surface types during dormant and snow-covered periods, *Remote Sens. Environ.*, **140,** 60-77.

Wen, X. H. and J. J. Gómez-Hernández, 1996: Upscaling hydraulic conductivities in heterogeneous media: an overview. *J. Hydrol.*, **183,** ix-xxxii.

Whitaker, J. S., and T. M. Hamill, 2006: Ensemble data assimilation without perturbed observation. *Mon. Weather Rev.*, **134,** 1913-1924.

Windstral, A., Elder, K. and R. E., Davis, 2002: Spatial snow modeling of wind-redistributed snow using terrain-based parameters. *J. Hydrometeor.*, **3,** 524-538.

Winsor, C. P., 1932: The Gompertz curve as a growth curve. *Proceeding of the National Academy of Science of the United States of America*, **18,** 1-8.

Wulder M. A., White J.C., Goward S.N., Masek J.G., Irons J.R., Herold M., et al., 2008: Landsat continuity: Issues and opportunities for land cover monitoring, *Remote Sens. Environ.*, **112,** 955–69.

Xue, Y., Sellers, P. J., Kinter, J., L., III and Shukla, J., 1991: A simplified biosphere model for global climate studies. *J. Climate*, **4,** 345-364.

Yin, X., Goudriaan, J., Lantinga, E. A., Vos, J., and H. J. Spiertz, 2003: A flexible sigmoid function of determinate growth. *Ann. Bot.*, **91,** 361-371.

Yang, Z. L., Dickinson, R. E., Robock, A., and Vinnikov, K. Y., 1997: On validation of the snow sub-model of the biosphere-atmosphere transfer scheme with Russian snow cover meteorological observational data. *J. Climate*, **10,** 353-373.